**Title**
The Effect of Particle Size and Processing on the Properties of a Barium Titanate Polymer Composite



**Author**
O'Neal, Audrey Pool

**Publication Date**
2014

Peer reviewed|Thesis/dissertation

UNIVERSITY OF CALIFORNIA

Los Angeles

# The Effect of Particle Size and Processing on the Properties of a Barium Titanate Polymer Composite

A dissertation submitted in partial satisfaction of the requirements for the degree Doctor of Philosophy in Mechanical Engineering

by

Audrey Pool O'Neal

2014

ABSTRACT OF THE DISSERTATION

The Effect of Particle Size and Processing

on the Properties of a Barium Titanate Polymer Composite

by

Audrey Pool O'Neal

Doctor of Philosophy in Mechanical Engineering

University of California, Los Angeles, 2014

Professor Adrienne Lavine, Chair

Multifunctional composite materials were developed to enhance the dielectric properties of an epoxy polymer by reinforcing it with ceramic barium titanate ($BaTiO_3$) particles. Potential applications for this material include structural capacitors that can be used to replace discrete capacitors, currently used for power conditioning or electrical discharge in military systems, giving rise to a reduction in system mass, and cost. $BaTiO_3$ particles with an average size of 100 nm (cubic) and 200 nm (tetragonal) were used as the filler and EPON™ Resin 862 (diglycidyl ether of bisphenol F) was used as the matrix. Two parametric studies were performed using Taguchi's Design of Experiments methods. The parameters varied were the volume fraction ($V_f$) of the particles; the particle size (crystal structure); and the use of dielectrophoretic assembly (DPA), by applying an electric field during the composite curing process. For Study 1, DPA was applied in the plane of the composite mold, and for Study 2, DPA was applied through the plane

of the composite mold. The failure stress, *FS*; Young's Modulus, *E*; dielectric constant, $\varepsilon_r$; and dielectric loss, tan$\delta$; were characterized and a signal-to-noise ratio analysis was conducted to determine the optimum combination of manufacturing parameters. For Study 1, to maximize *FS*, the optimum combination was 25% $V_f$, 100 nm (cubic) particles, and no DPA. To maximize *E* and $\varepsilon_r$, the optimum combination was 50% $V_f$, 200 nm (tetragonal) particles, and no DPA. To minimize tan$\delta$, the optimum combination was 50% $V_f$, 100 nm (cubic), and with DPA applied. For study 2, to maximize *FS*, and to minimize tan$\delta$, the optimum combination was 25% $V_f$, 100 nm (cubic) particles, and no DPA. To maximize *E* and $\varepsilon_r$, the optimum combination of parameters was 50% $V_f$, 200 nm (tetragonal) particles, and no DPA. For both studies, the optimum combination of parameters was determined through statistical methods, and supported by the physics which govern the material properties. A numerical simulation calculated the magnitude of the electric field inside the composite, and the charge on the surface of the material. The simulation and experimental results were in good agreement.

The dissertation of Audrey Pool O'Neal is approved.

Christopher Lynch

Ajit Mal

Jenn-Ming Yang

Adrienne Lavine, Committee Chair

University of California, Los Angeles

2014

This dissertation is dedicated to my mother, who has always supported all of my hopes, dreams and aspirations.

# *Table of Contents*

# *List of Figures*

# *List of Tables*

# *Acknowledgements*

I must begin by acknowledging God and His Grace, which sustains me. Without His Blessings, none of this would be possible and as long as I have breath, I will continue to praise His name. I would like to thank my mother, Mrs. Joyce N. Fowler, for being my biggest cheerleader throughout life. Part of the motivation to complete this degree was to make you proud. You are my best friend, my counselor, my advisor and my rock. I would like to thank my sister, Mrs. Kim Pool Ridgell, for being the next biggest cheerleader in my life. You encourage and inspire me as much today, as you did when I was a little girl trying to emulate you. I would like to thank my nephew, Mr. Devin Johnson, for also being an inspiration in my life. If I can achieve anything small and be an example for you, I know that you will continue to achieve big things and fulfill all of your hopes and dreams. To my late husband, Mr. Ron O'Neal, I owe this degree, my life in California and so much more. Thank you for giving me the courage to come here and for continuing to inspire me to stay here, even when times were hard. This is our degree, just like we always planned it. To my cousins, Christel Darden, Troy Hall, Adrienne Fuller, Tiffany Brooks, Gloria and Harold Fuller, Dr. Wendell O'Neal and Patricia Grant, your love and support have been invaluable to me throughout my life and particularly during this process. Thank you from the bottom of my heart. To my sister-in-law Kathleen O'Neal, we've been through so much together and we both have more joyous days ahead. Thank you for staying in my corner. To my brother Mark Greenwood, thanks for all of the support, advice, and for being the first person to call me Dr. Flea. To my best friend and brother Anthony Johnson, I could not have done this without you and I sincerely thank you. To my nephew Leon Williams, thanks for the laughs, and for being the first person to call me Dr. Auntie. To the

Adkisson family; Barbara, Carolyn Jean (CJ), Pamela and Kayla, thank you all for your love and support throughout my career. You must all know that none of this would have been possible without the support of the late Mr. Jack Adkisson, who gave me my start with General Motors, ensured that I attended General Motors Institute, and served as my mentor from the start of my career until his retirement. I will be eternally grateful to Jack and to all of you. To my dear friend and brother Mr. Marcus Sims, on the day we met you told me that I would obtain a Ph.D. and at the time, I was merely a sophomore in undergraduate school. You have continued to encourage and inspire me from that day to this one, and I have finally fulfilled your prophetic expectation. To all of my Walker family members in Los Angeles, and all of my family near and far, thank you for your prayers, words of encouragement and for continuing to believe in me when I had many doubts.

I would like to acknowledge the generous support, encouragement and genuine kindness of my committee chair, Professor Adrienne Lavine. You are a person who does what is right, even when it is not in your own interest. That was certainly the case when you became my advisor, counselor and committee chair. Words fail to express my gratitude, so I will have to just say thank you, although it seems very inadequate. I would like to thank all of the members of my doctoral committee. Professor Ajit Mal, you have supported and encouraged me from the start. Thank you for all of the equipment, time and resources that you so generously dedicated to my work. I would also like to thank Dr. Harsh Baid and Himadri Samajder, two members of your research team, for all of their assistance. Professor Christopher Lynch, just by coming to UCLA you advanced my work exponentially. You have always shown an interest in my work, and because you provided an incredible amount of equipment, time, human resources, and incredible advice, I was able to complete this work. This would not have been possible without

you and Sam Goljahi, who personally dedicated himself to numerous high-voltage experiments required to complete this research. I will remain eternally grateful to you both. Professor Jenn-Ming Yang, thank you for also allowing me to use equipment in your lab that was critical to this research, and for sticking with me throughout this long process. I would also like to thank my former committee chair, Professor Emeritis H. Thomas Hahn, for the opportunity to begin this project and for your support. To another former committee member, Professor Gregory P. Carman, I sincerely thank you for all of your support throughout the years. You have welcomed me into your lab and allowed me to use equipment and brain power, as needed. To your graduate student Paul Nordeen I give special acknowledgement for all of the numerical simulation work. Thank you for everything. To Miguel Lozano, who has provided assistance with everything on this project that ever needed to be cut, sanded, or welded, I sincerely thank you. I also thank you for your friendship. To Dr. Ignacio Martini, Associate Director of the UCLA Molecular Instrumentation Center, I thank you for your support and assistance throughout the years. I would not have been able to complete this work without your assistance, kindness and understanding. To Dean Vijay K. Dhir, thank you for your encouragement throughout this process.

To my colleagues in the UCLA Center for Excellence in Engineering and Diversity (CEED), who are much more like family than colleagues, I thank you all for your support, kindness, friendship and encouragement. Each and every time I wanted to give up, Rick Ainsworth always found a way to make sure that I didn't. I thank you for doing so, and now look at what you've helped me accomplish. To my sister and best friend Catherine Douglas, your enthusiasm and encouragement are infectious and only rivaled by your genius and generosity. You inspire me with all that you do and I am so grateful that you consider me a

friend. To Carol Cadle, Scheherezade (Sherry) Hormozi, Blanca Madrigal, and Linda Robertson, thank you for welcoming into the CEED family. When I first arrived in CEED I felt like a duck out of water, yet the four of you made every effort to welcome me into this amazing organization, and you have provided nothing but kindness and friendship since I've been here. Thank you so much. And because he was an honorary member of CEED while working at UCLA, I would like to thank my friend and brother Mr. KiMi Wilson, who will soon be Dr. KiMi Wilson. Thank you for your friendship and for providing me with such amazing students through your outreach program. Without your dedicated support to the students and to my efforts, this dream would not have become reality.

To all of the students with whom I have worked, this is our degree. None of this would have been possible without you. I would like to thank Mr. Gbenga Elehinafe, Mr. Alex Franceschi, Mr. Abubakarr Bah, Mr. Cesar Quinde, Mr. Adam Provinchain, Ms. Folasade (Sade) Adeseun, Mr. Gregory Caguimbal, Mr. Anthony Anderson, Mr. Edgar Mendoza, and Ms. Morolake (Duchess) Omoya. You inspired me to continue and now we all have this Ph.D., as I share it with all of you. Thank you for everything.

# *Vita*

## Audrey Pool O'Neal

## Education

**MS** **University of California, Los Angeles**
Mechanical Engineering

**MS** **Rensselaer Polytechnic Institute**
Engineering Science — Management of Technology

**BS** **GMI Engineering & Management Institute**
Mechanical Engineering

***Thesis: High Carbon to Low Carbon Steel Welding***

B. Lee Tuttle, Advisor

## Teaching Experience

**University of California, Los Angeles, Center for Excellence in Engineering and Diversity, 2005 – Present**

**Co-Instructor for the Introduction to Engineering Disciplines Course**

*Responsible for the computer literacy and team research projects*

**University of California, Los Angeles, Mechanical & Aerospace Engineering Department, 2003-2004**

**Teaching Associate**

***Teaching Apprentice Practicum***

*Presented best teaching practices, to new graduate teaching assistants in the Mechanical & Aerospace Engineering Department, using traditional and multi-media presentation methods (lectures, video-tapes, computer presentation, etc.)*

**Teaching Assistant**

***Probability & Its Applications to Risk, Reliability and Quality Control***
***Mechanical Product Design***

**University of California, Los Angeles, Center for Excellence in Engineering and Diversity, Summer 2004**

**Instructor**

***Elementary Fluid Mechanics***

## Awards/Honors/Fellowships

**Graduate Assistance in Areas of National Need (GAANN) Fellowship, University of California, Los Angeles**

*2005*

**Center for Excellence in Engineering and Diversity (CEED) Leadership Award, University of California, Los Angeles**

*2004-2005*

## Publications

### Co-Authored Article

A. D. Pool (maiden name) and H. T. Hahn, A Nanocomposite for Improved Stereolithography, 48th International Society for the Advancement of Material and Process Engineering (SAMPE) Symposium, **48**(2), 1617-1626 (2003)

## Other Professional Experience

### University of California, Los Angeles, Center for Excellence in Engineering and Diversity, 2007 – Present

#### Associate Director for Undergraduate Programs

*Responsible for directing the undergraduate research program, and coordinating supplemental education programs to improve students' academic performance*

### University of California, Los Angeles, Multifunctional Composites Research Laboratory, 2000 – 2005

#### Graduate Student Researcher

*Conducted research and development in the area of multifunctional, polymer nanocomposite materials*

# *Chapter 1: Introduction and Background*

Multifunctional composite materials were developed to enhance the dielectric properties of an epoxy polymer by reinforcing it with ceramic barium titanate ($BaTiO_3$) particles. The goal of combining the two materials is to take advantage of the dielectric properties of a monolithic ceramic without the limitations of the brittle material. Potential applications for this material include structural capacitors that can be used to replace discrete capacitors currently used for power conditioning or electrical discharge in military systems, giving rise to a reduction in system mass, and cost. The material can also be used to integrate capacitors into existing electronic packaging to reduce size and weight, while simultaneously increasing speed and durability. Barium titanate ($BaTiO_3$) particles with an average size of 100 nm and 200 nm were used as the filler and EPON™ Resin 862 (diglycidyl ether of bisphenol F) was used as the matrix. The crystal structure of the 100 nm particles is cubic and it is tetragonal for the 200 nm particles. A silane coupling agent and a viscosity modifier were also used in this research to improve particle bonding to the matrix, to decrease particle agglomeration and to reduce the viscosity of the particle/resin mixture. Two parametric studies were performed using Taguchi's Design of Experiments methods. The parameters varied were the volume fraction ($V_f$) of the particles; the particle size (crystal structure); and the use of dielectrophoretic assembly (DPA) by applying an electric field during the composite curing process. In Study 1, DPA was applied in the plane of the mold used to manufacture composite specimens, and will hereafter be referred to as In-Plane DPA. In Study 2, DPA was applied through the plane of the mold used to manufacture the composite specimens, and will hereafter be referred to as Through-Plane DPA. Although maximizing all of the parameters is not part of Taguchi's Design of Experiments

methods, a composite material with all of the parameters maximized was also created, for this research, and a sample of unaltered resin was prepared and tested as a control. The mechanical and dielectric properties of the composite materials were characterized and a signal-to-noise ratio analysis was conducted to determine the optimum combination of manufacturing parameters. Rank analysis was also conducted to determine which parameter had the greatest impact on the material properties. The experimental results were then compared to existing models for relative permittivity. A numerical simulation was also performed to model the behavior of the material, in the presence of an electric field. The electric field throughout the material was obtained, along with the charge on the material surface. From the surface charge data, dielectric constant was found and compared to the experimental results.

## *1.1 Capacitance with Direct Current Electrical Potential*

Capacitance is the ability of a material to hold an electric charge and has the units of Farads [F]. A very simple capacitor consists of parallel plates that are separated by a small distance. If a direct current (DC) electrical potential, also known as a voltage ($V$) is applied across two parallel plates, with surface area ($A$), being separated a small distance ($d$), with only air between them, we can assume that the electric field ($E$) is uniform, and the amount of charge acquired by each plate is ($Q$) as shown in Figure 1. Note that any fringing effects of the electric field are ignored.

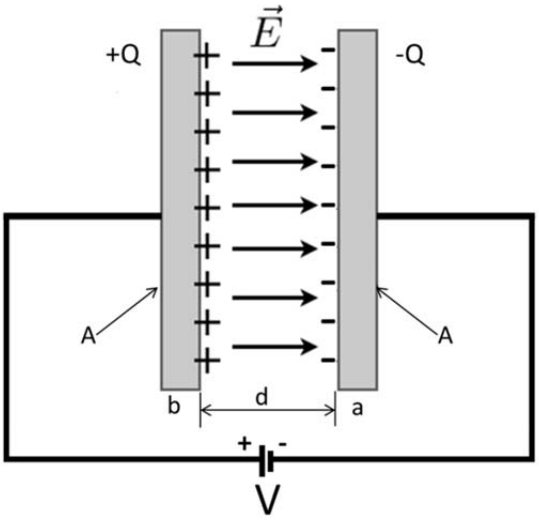


**Figure 1: Parallel-plate capacitor connected to a DC electrical potential[1]**

The charge ($Q$) acquired by each plate is proportional to the potential difference $V_{ba} = V_b - V_a$, and the constant of proportionality is the Capacitance ($C$) given by Equation 1.1.1[1].

$$Q = CV_{ba} \qquad \textbf{Equation 1.1.1}$$

In the case when there is air between the parallel plates, the capacitance will be referred to as the initial capacitance or $C_0$. The electric field is given by Equation 1.1.2[1].

$$E = \frac{\sigma}{\varepsilon_0} \qquad \textbf{Equation 1.1.2}$$

The electric field is perpendicular to the plates, $\varepsilon_0$ is a constant known as the permittivity of free space, and equals 8.854 x $10^{-12}$ F/m. The charge per unit area ($\sigma$) is given by Equation 1.1.3[1].

$$\sigma = \frac{Q}{A} \qquad \textbf{Equation 1.1.3}$$

Using Equations 1.1.2 and 1.1.3, the field is given by Equation 1.1.4.

$$E = \frac{Q}{\varepsilon_0 A} \qquad \textbf{Equation 1.1.4}$$

Electric field and electrical potential are related by Equation 1.1.5[1].

$$V_{ba} = -\int_a^b E \cdot dl \qquad \textbf{Equation 1.1.5}$$

The infinitesimal increment of displacement is ($dl$). If the integral is taken along a path not parallel to the field lines, from plate b to plate a, then $\theta = 180^\circ$, and cos 180º = -1. The potential is related to electric field by Equation 1.1.6.

$$V_{ba} = -\int_a^b E \cdot dl \cos 180^\circ = +\int_a^b E \cdot dl = \frac{Q}{\varepsilon_0 A}\int_a^b dl = \frac{Qd}{\varepsilon_0 A} \qquad \textbf{Equation 1.1.6}$$

From Equations 1.1.1 and 1.1.6, capacitance can be found with Equation 1.1.7.

$$C_0 = \frac{Q}{V_{ba}} = \varepsilon_0 \frac{A}{d} \qquad \textbf{Equation 1.1.7}$$

These plates are typically rolled into a cylinder with an insulator or a dielectric between them, to produce capacitors.

## *1.2 Capacitance with Alternating Current Electrical Potential*

For the derivations in section 1.1, the capacitor was connected to a direct current (DC) source of electrical potential, but when a parallel plate capacitor is connected to an alternating current (AC) source of electrical potential, as shown in Figure 2, the voltage given is by Equation 1.2.1[2].

$$V = V_0 e^{i\omega t} \qquad \textbf{Equation 1.2.1}$$

$V_0$ is the maximum voltage, and ω is the angular frequency given by $\omega = 2\pi f$, where $f$ is the frequency of the alternating current.

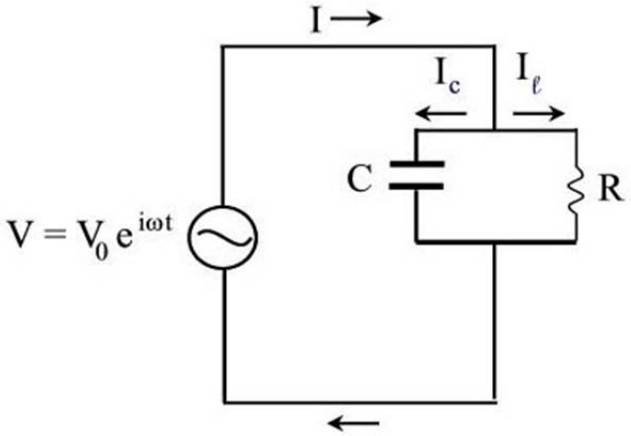


**Figure 2: Circuit with Capacitor, Resistor and AC Voltage[2]**

The charge of the capacitor is given by Equation 1.2.2.

$$Q = C_0 V = C_0 V_0 e^{i\omega t} \qquad \textbf{Equation 1.2.2}$$

The charging current ($I_c$) leads the applied voltage by a phase angle of 90º, and is given by the Equation 1.2.3[2].

$$I_c = \frac{dQ}{dt} = i\omega C_0 V \qquad \textbf{Equation 1.2.3}$$

Now if the space between the capacitor is filled with a dielectric material, there is an increase in capacitance ($C$) given by Equation 1.2.4[2].

$$C = \frac{\varepsilon}{\varepsilon_0} C_0 = \varepsilon' C_0 \qquad \textbf{Equation 1.2.4}$$

Combining Equations 1.1.7 and 1.2.4, the increased capacitance due to the presence of a dielectric material is also given by Equation 1.2.5.

$$C = \frac{\varepsilon A}{d} \qquad \textbf{Equation 1.2.5}$$

The permittivity of the dielectric material is $\varepsilon$ and the relative permittivity of the material, also known as the dielectric constant, is $\varepsilon_r$ and equals $\varepsilon'$. From equation (1.2.4), $\varepsilon'$, which

represents the ratio of the dielectric constant of the material to the dielectric constant of vacuum, is given by Equation 1.2.6.

$$\varepsilon' = \frac{\varepsilon}{\varepsilon_0} \qquad \textbf{Equation 1.2.6}$$

For the parallel connection of a capacitor and resistor shown in Figure 2, a complex permittivity ($\varepsilon^*$) can be defined and is given by Equation 1.2.7[2].

$$\varepsilon^* = \varepsilon' - i\frac{1}{\omega R} \qquad \textbf{Equation 1.2.7}$$

The resistance($R$) and the complex permittivity can also be defined by Equation 1.2.8[2].

$$\varepsilon^* = \varepsilon' - i\varepsilon'' \qquad \textbf{Equation 1.2.8}$$

The real part of the permittivity, which is related to the stored energy within the medium, is $\varepsilon'$, and the imaginary part of the permittivity, which is related to the dissipation (or loss) of energy within the medium, is $\varepsilon''$. Setting Equation 1.2.7 equal to Equation 1.2.8 shows that $\varepsilon'' = 1/\omega R$.

In addition to increased capacitance, the presence of the dielectric also increases the charge on the capacitor, and the charging current. The increased charge on the capacitor and the increased charging current are given by Equations 1.2.9 and 1.2.10, respectively.

$$Q = CV = \varepsilon' C_0 V_0 e^{i\omega t} \qquad \textbf{Equation 1.2.9}$$

$$I_c = \frac{dQ}{dt} = i\omega\varepsilon' C_0 V \qquad \textbf{Equation 1.2.10}$$

Since no dielectric material is a perfect insulator, in addition to $I_C$, which leads the voltage by 90º, there is an additional AC conduction current $I_\ell$ shown in Figure 3 that is in phase with the voltage and represents the energy loss or power dissipated in the dielectric[2]. As a result of the energy loss, the total current flow on discharge of the capacitive cell (**I**) consists of two vector components ($I_C$) and ($I_\ell$).

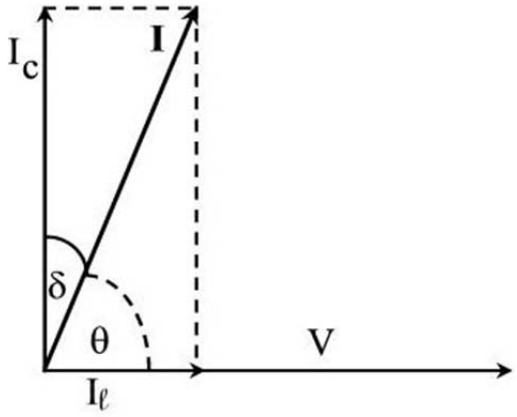


**Figure 3: Loss Tangent for Typical Dielectric[2]**

The charging and loss current can be represented by the complex permittivity given in Equation 1.2.8 and the total current (**I**) is then given Equation 1.2.10[2].

$$\mathbf{I} = i\omega C_0 \left(\varepsilon' - \varepsilon''\right)V = i\omega C_0 \varepsilon' V + \omega C_0 \varepsilon'' V = I_c + I_\ell \qquad \textbf{Equation 1.2.11}$$

Alternatively the loss angle ($\delta = 90^\circ - \theta$) can be used to define the loss tangent given by Equation 1.2.12.

$$\tan\delta = \frac{I_\ell}{I_c} = \frac{\omega C_0 \varepsilon'' V}{\omega C_0 \varepsilon' V} = \frac{\varepsilon''}{\varepsilon'} \qquad \textbf{Equation 1.2.12}$$

The loss tangent (tan $\delta$) is also called the dissipation factor and represents the energy dissipated (usually in the form of heat) per cycle[3].

## *1.3 Dielectrics*

Practically all of the electronic charges in a dielectric material are bound to their parent atoms or molecules. Since they are not free to migrate under the application of an electric field, they are not conductive like metals. Instead of conducting charge when an electric field is applied, the bound charges displace slightly, relative to one another, with the positive charges being displaced in the direction of the field and the negative charges in the opposite direction. Figure 4 illustrates a parallel plate capacitor with a dielectric material between the plates or

electrodes that are a distance *d* apart[4]. Each atom or molecule in the dielectric acquires an electric dipole moment and this effect is referred to as dielectric polarization.

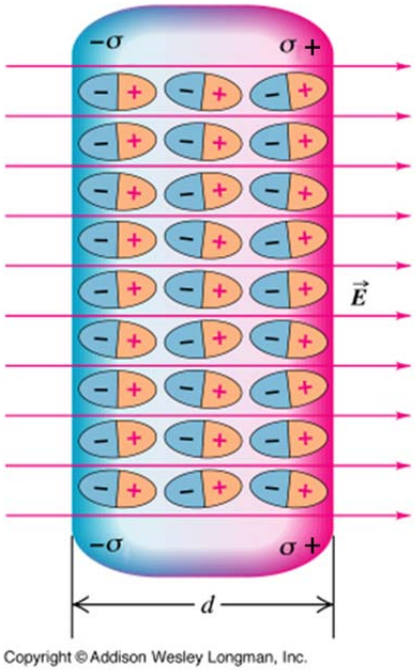


**Figure 4: Electric Dipole Moment of Dielectric Material in a Parallel Plate Capacitor[4]**

The polarization (*P*) is parallel to and in the same direction as the applied electric field (*E*). The field is a function of voltage (*V*) and the distance between the electrodes (*d*) and is given by Equation 1.3.1[2].

$$E = \frac{V}{d} \qquad \textbf{Equation 1.3.1}$$

The polarization (*P*) is given by Equation 1.3.2[5].

$$P = \chi' \varepsilon_0 E \qquad \textbf{Equation 1.3.2}$$

The dimensionless constant $\chi'$ is known as the real electric susceptibility.

The combined effects of the electric field and the electric polarization can be described by defining an additional vector term *D*, which is the electric displacement, also known as the dielectric displacement, and is given by Equation 1.3.3[5].

$$D = \varepsilon_0 E + P$$ **Equation 1.3.3**

The dielectric displacement describes the extent to which the electric field has been altered by the presence of the dielectric[3]. Assuming the polarization and the field are collinear, $\chi'$ reduces from a second rank tensor to a scalar and Equations 1.3.2 and 1.3.3 yield Equation 1.3.4.

$$D = \varepsilon_0 E + \chi' \varepsilon_0 E = (1 + \chi') \varepsilon_0 E$$ **Equation 1.3.4**

The increased capacitance resulting from filling the space between the electrodes with a dielectric material can also be written in terms of the electric susceptibility ( $\chi'$ ) and is given by Equation 1.3.5.

$$C = (1 + \chi') \mathrm{C}_0$$ **Equation 1.3.5**

From Equation 1.2.4 it can be seen that the relative dielectric constant and the electric susceptibility are related by Equation 1.3.6.

$$\varepsilon' = \left(1 + \chi'\right)$$ **Equation 1.3.6**

Using Equation 1.3.4, the dielectric polarization (*P*) and the electric displacement (*D*) can be written in terms of the dielectric constant ( $\varepsilon'$ ) and the electric field (*E*) as shown in Equations 1.3.7 and 1.3.8, respectively.

$$P = \varepsilon_0 \left(\varepsilon' - 1\right) E$$ **Equation 1.3.7**

$$D = \varepsilon' \varepsilon_0 E$$ **Equation 1.3.8**

In capacitors, the parallel plates are rolled into cylinders with insulators or dielectric materials separating the plates, as shown in Figure 5[6,7]. Dielectric materials allow the electrodes of a capacitor (the parallel plates) to be placed closer together, without touching, leading to an increased capacitance due to a smaller distance (*d*). As shown in Equation 1.2.5, Capacitance (*C*) is inversely proportional to the distance between the electrodes (*d*).

## 1.4 *Capacitors*

Capacitors can store electric charge, are used in nearly all electronic circuits and have various end user applications including but not limited to consumer electronics, automotive and health care equipment, information & communication technology, infrastructure, and military equipment.

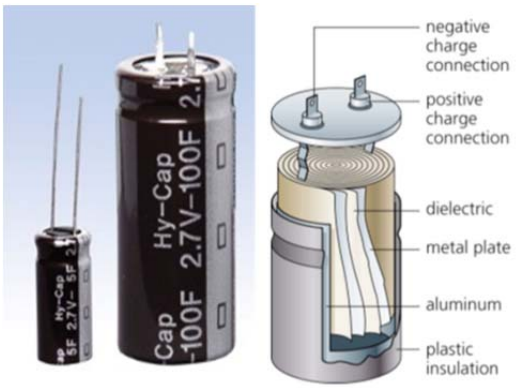


**Figure 5: Discrete Capacitors (left)—Capacitor Showing Rolled Electrodes and Dielectric Material (right)[6,7]**

In 2010, an estimated 1.3 trillion capacitors were sold with a total market value of $15.1 billion[8]. Figure 6 shows the quarterly sales trends from 2008 – 2010, of the top four ceramic capacitor manufacturers[9].

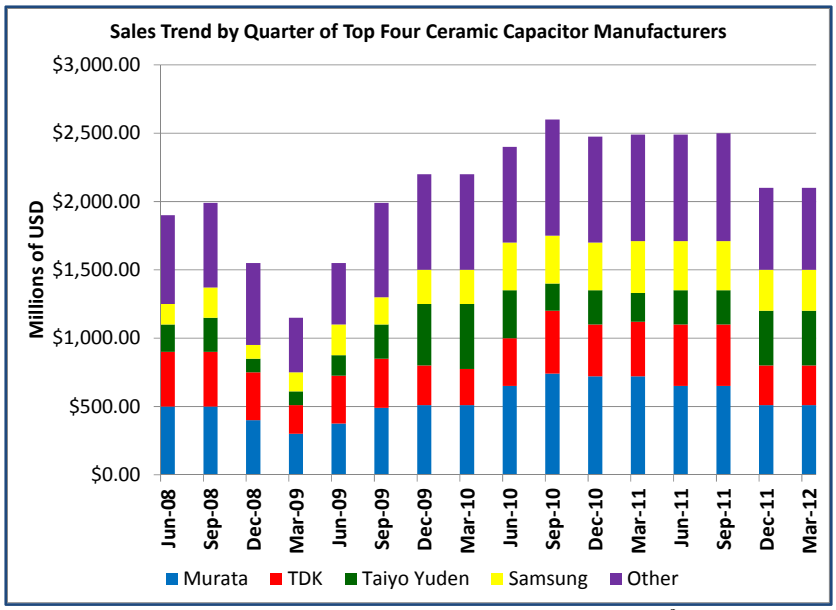


**Figure 6: Sales trends of capacitors in Millions of USD[9]**

The current drive toward miniaturization of electronic devices is also fueling the drive for integrated and structural capacitors. Cellular phones, digital cameras, tablet computers, other portable devices, and wearable electronics, each contain hundreds of capacitors. These products will continue to require smaller electronic components with increased capabilities.

## *1.5 Literature Review*

Applications for polymer matrix composites with dielectric properties are far ranging. Roberts[10] investigated using a silicone rubber/lead zirconia titanate (PZT) composite as a dielectric element that could be embedded into the aircraft skin of an antenna panel. Carrodeguas et al.[11] developed a barium titanate ($BaTiO_3$)/polymethyl methacrylate (PMMA) composite material as bone cement for percutaneous injection into a cervical, thoracic or lumbar vertebral body lesion to relieve pain and strengthen bone. Chiang et al.[12] produced ferroelectric ceramic/polymer composites by adding $BaTiO_3$ particles into a UV curable, trimethylolpropane triacrylate polymer matrix. The potential application for this work was integration into high frequency electronics. Liang et al.[13] and Cho et al.[14] investigated $BaTiO_3$/epoxy composite materials for use as embedded capacitors for electronics. Korleski et al.[15] also investigated dielectric/polymer composites for electronic packaging applications. Balasubramanian[16] investigated $BaTiO_3$ filler in a polystyrene matrix, for pulse power applications. While Kim[17] investigated $BaTiO_3$ and related metal oxide nanoparticles in a poly(vinylidene fluoride-co-hexafluoropropylene) (P(VDF-HFP)) polymer matrix for such potential applications as high-energy-density capacitors and gate insulators in organic field-effect transistors.

In addition to wide ranging applications, the methods used to produce the composites also differ among researchers. Two important and interrelated categories emerged when

reviewing the literature and those categories include the composite connectivity and the composite processing.

### *1.5.1 Composite Connectivity*

Two numbers are used to designate the connectivity of diphasic composites. This system was developed by Newnham et al.[18] The first number describes the continuity of one phase of the composite and the second number describes the continuity of the other phase of the composite, both in Cartesian space. For example, let the first number represent the matrix material of the composite and let the second number represent the filler material. If the composite has particulate filler material that is homogeneously dispersed in a polymer matrix, it would be described as having 3-0 connectivity or be referred to as a 3-0 composite. The 3 indicates the matrix material is continuous in all three directions and the zero indicates the filler material is not continuous in the x, y, or z directions. A polymer matrix reinforced with unidirectional fibers would be designated as having 3-1 connectivity, as the matrix material is still continuous in all three directions, but the filler material is only continuous in one direction. Figure 7 shows the ten connectivity patterns for diphasic composites[18].

Composites with 3-0 connectivity are attractive due to their relative ease of manufacturing, their ability to be shaped into various forms and their ability to be fabricated using mass production methods[19]. It is widely believed that manipulation of dielectric particles in ceramic/polymer composites to induce connectivity between them will result in the creation of composites with greater dielectric properties. Connectivity of the individual phases controls the electric flux pattern and mechanical properties of the material[18].

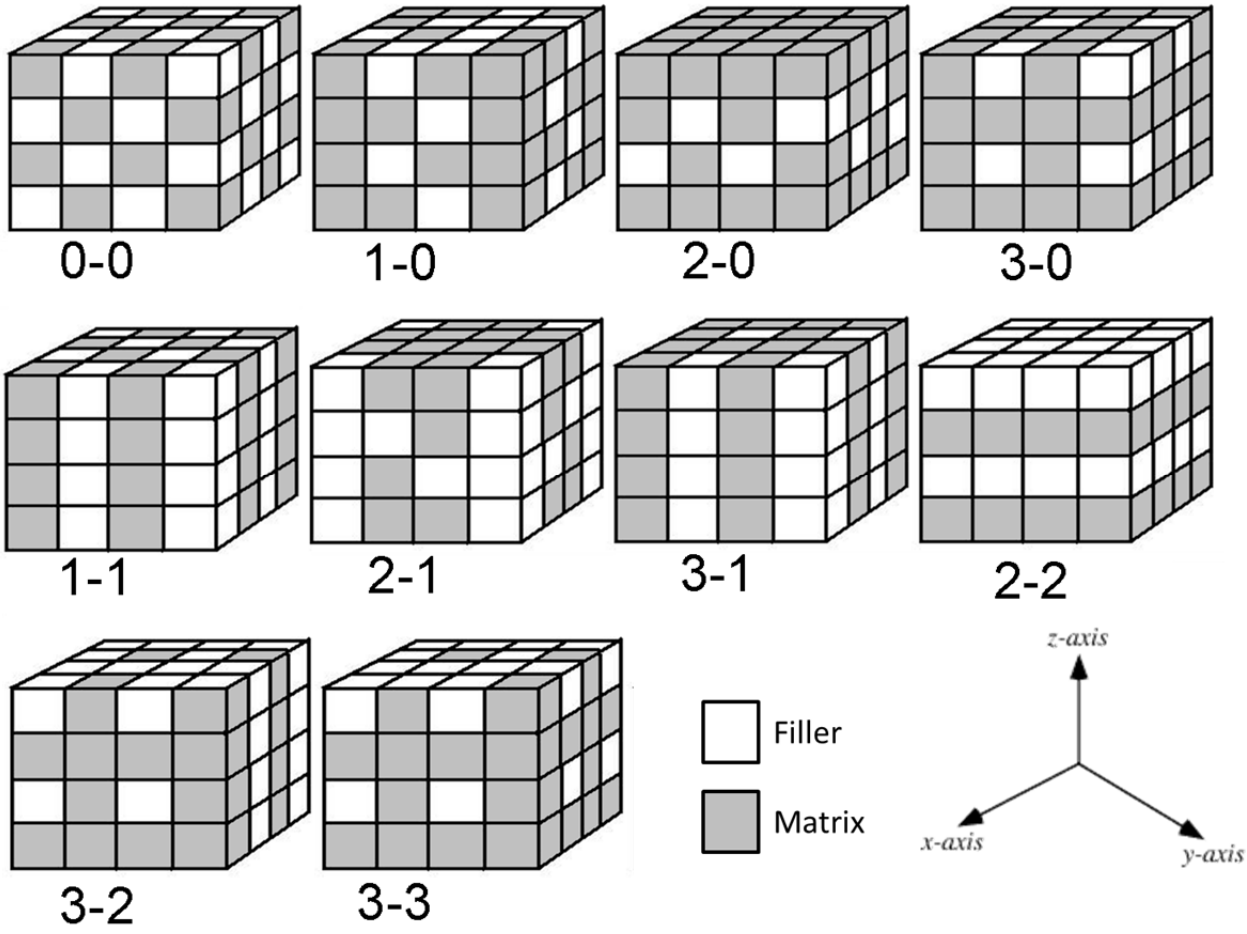


**Figure 7: Diphasic Composite Connectivity Patterns[18]**

### *1.5.2 Composite Processing: Dielectrophoretic Assembly (DPA)*

Application of an electric field induces a dipole-dipole interaction between neutral, suspended particles, as shown in Figure 8[20]. If the field is divergent the particles will become polarized and move in the direction of higher field concentration. Polarization of the neutral particles is known as dielectrophoresis and it can be used to force suspended dielectric particles to redistribute themselves and form chains parallel to the electric field. When used to manufacture dielectric/polymer composites, the technique is known as dielectrophoretic assembly (DPA)[21]. The application of DPA changes the connectivity of the composite from 3-0 to 3-1.

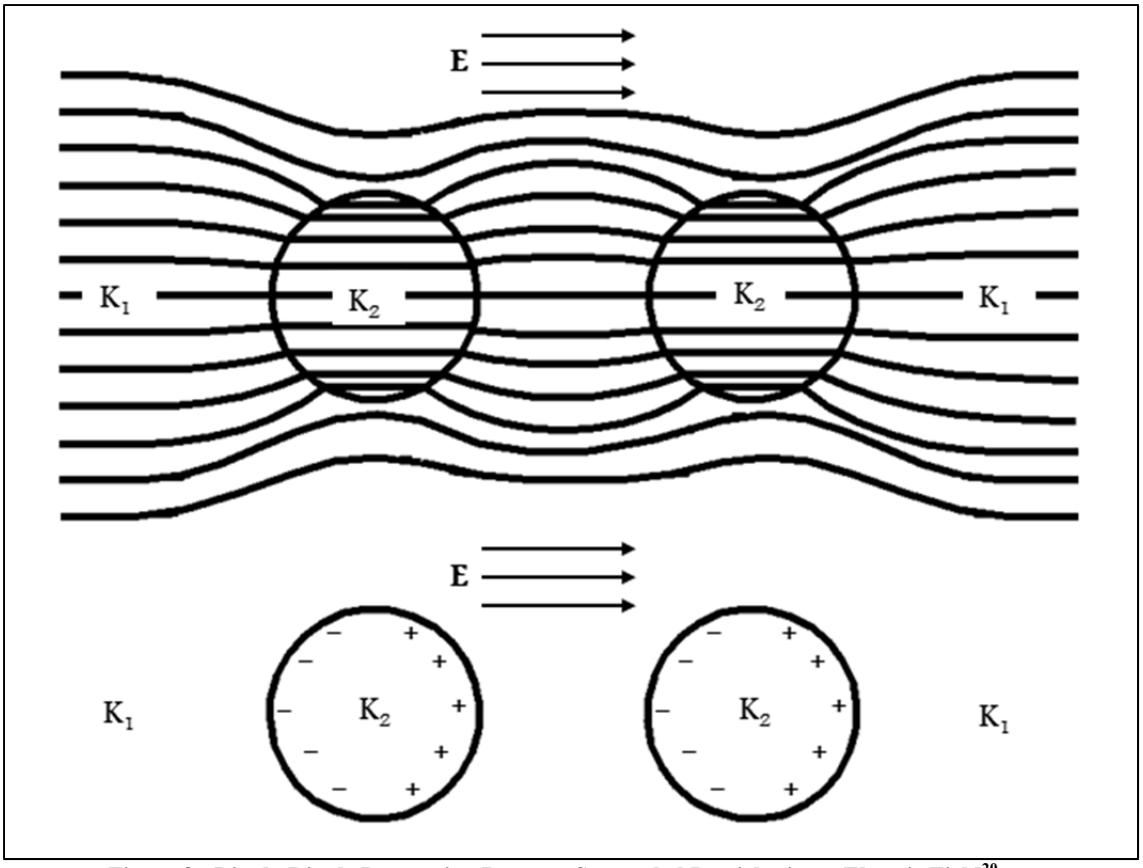


**Figure 8: Dipole-Dipole Interaction Between Suspended Particles in an Electric Field[20]**

Randall et al.[21] were able to create particle/polymer composites with quasi 3-1 connectivity by applying DPA to align $BaTiO_3$ particles in a silicone elastomer matrix. The composites were referred to as quasi 3-1, as all of the elastomer could not be removed from between the particles, thus the connectivity of the particles was not completely continuous. An SEM image of their results can be found in Figure 9. Khastgir and Adachi[22] also used DPA to align $BaTiO_3$ particles in silicone rubber. The dielectric constant experimental results were compared to a mixing theory proposed by Wagner, as well as a mixing law proposed by Bottcher and Bruggeman, with good agreement between the models and their results. However, the dielectric constants measured were higher than the predictions and the discrepancies were attributed to the concentration of $BaTiO_3$ particles in the specimens and aggregation of the

particles in the polymer matrix. These researchers did not employ any surface treatment techniques to aid dispersion of the particles into the polymer.

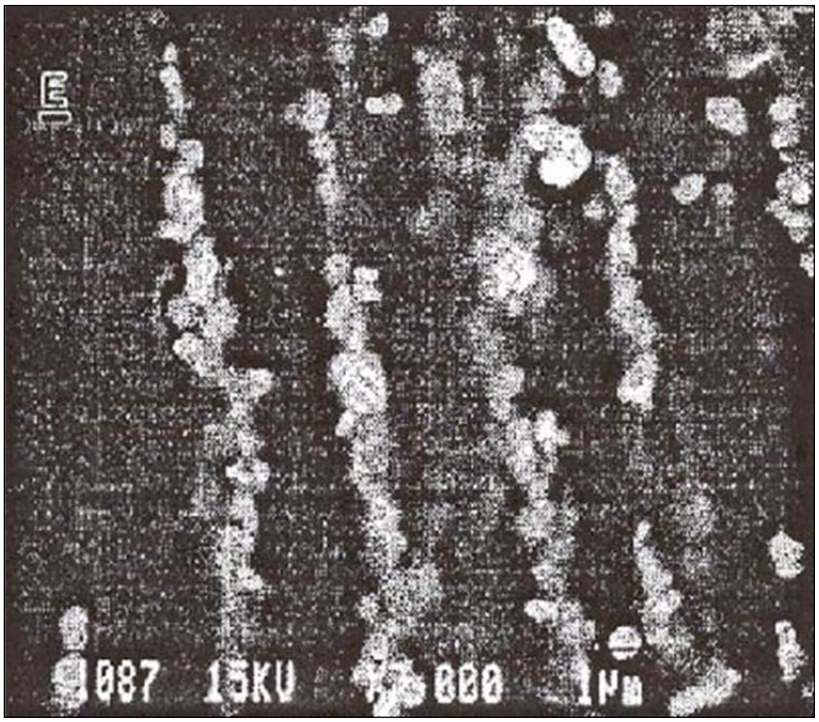


**Figure 9: SEM Image of Aligned $BaTiO_3$ Particles in a Silicone Elastomer Matrix[21]**

Bowen et al.[23] also used DPA to align PZT particles in a silicone elastomer matrix and compared them to composites with randomly dispersed particles. The dielectric constant of the composites with 3-1 connectivity was 2 to 3 times greater than the dielectric constant of the composites with 3-0 connectivity. Dielectrophoretic assembly was used in this dissertation research, to align $BaTiO_3$ particles in an epoxy matrix.

### *1.5.3 Composite Processing: Compounding Techniques*

Some researchers have used chemical solution methods to create $BaTiO_3$ particles in-situ and evenly disperse them in polymer matrices. Collins and Slamovich[24] used chemical solution methods to create $BaTiO_3$ particles in-situ and evenly disperse them in a polymer solution, for the creation of dielectric thin films. Titanium diisopropoxide bis (ethylacetoacetate) (TIBE) was

dissolved in toluene with either polystyrene-block-polybutadiene-block polystyrene (SBS) or styrene-co-maleic anhydride (S-MAH) block copolymer, to create the thin films. Lee et al.[25] were able to produce $BaTiO_3$/polystyrene-block-polybutadiene-block polystyrene (SBS) nanocomposite thin films by creating cubic $BaTiO_3$ particles in-situ, with an approximate size of 10 nm, using hydrothermal techniques. Hirano et al.[26] developed an in-situ processing technique to produce $BaTiO_3$ particle/polymer composites based on the reaction control of chemically designed metal-organics. Somani et al.[27] and Patil et al.[28]created conducting polyaniline/$BaTiO_3$ composites by in-situ deposition of fine grade $BaTiO_3$ in the polymerization reaction mixture of aniline. In most cases, the researchers created the particles in-situ in order to control the size, shape and phase of the $BaTiO_3$ particles produced[25] or to avoid the powder agglomeration and coagulation problems associated with the use of compounding techniques[24,26,29]. But with some exceptions, such as gold and other metal phases, in-situ development of particles yields only precursors to ceramic crystalline material that provide properties far less than those anticipated from fully developed, crystalline particles[29]. As a result, the use of compounding techniques to incorporate fully developed crystalline particles into polymers is now a growing field and this approach serves as the basis for this dissertation.

Many researchers have used compounding techniques to create ceramic/polymer composites. Cho et al.[14] used a combination of ultrasonic treatment and ball milling to combine $BaTiO_3$ particles and epoxy resin to create embedded capacitor films (ECFs). Ultrasonic treatment along with a dispersant were used for particle de-agglomeration and the particle/epoxy suspension was ball milled for two days to achieve thorough mixing and dispersion of the particles. Wang et al.[30] mixed $BaTiO_3$ nanoparticles, ethanol and ground polystyrene sulfonic sodium (PSS) polymer powder into a dilute paste to create humidity sensing composite films.

Chiang et al.[12] used compounding techniques to produce their $BaTiO_3$/polymer composite films and found particle cluster formation at particle volume fractions below 25% and uniform particle distribution above 25% volume fraction.

### *1.5.4 Composite Processing: Silane Coupling Agents*

Rong et al.[31] acknowledged the difficulty of dispersing nanoparticles into polymer resins due to the strong attraction between the particles and the limited shearing force applied during compounding. To this end, they used various silane-coupling agents to functionalize (i.e. introduce double bonds onto the particles) in order to mix $Al_2O_3$, SiC and $Si_3N_4$ nanoparticles into epoxy resins. The suspensions were stirred for 3 hours and ultrasonically treated for 1 hour, in order to obtain homogeneous dispersion. Liang et al.[13] obtained homogeneous dispersions of $BaTiO_3$ particles into an epoxy matrix, through mixing, after functionalizing the surface of the ceramic powders with a silane-coupling agent. The volume fraction of particles in their work was as high as 60%. Blum et al.[29] also used a similar surface treatment approach to incorporate fully developed, crystalline $TiO_2$ nanoparticles into both low and high molecular weight polyacrylic acid (PAA), by modifying the surface of the particles with an organo-alkoxysilane. Silane coupling agents were used in the current research in order to covalently bond the inorganic $BaTiO_3$ particles with the polymer matrix and facilitate dispersion[13,29]. Ultrasonic treatment and centrifugal mixing were used to disperse the particles throughout the polymer matrix in this dissertation research.

Table 1 was prepared as an aid to synthesize the vast amount of research done to develop $BaTiO_3$/polymer composites[11-14,19,22,24-25,27,30,32-38].

**Table 1: Literature Review Summary**

| Filler | Mean Dia. | Volume Fraction (%) | Matrix | Processing | Connec -tivity | $\varepsilon_r$ | tan $\delta$ | Elastic Properties | Ref. No. |
|---|---|---|---|---|---|---|---|---|---|
| $BaTiO_3$ | 0.3 μm | 30 | PVDF | Dispersant & Poling | 3-0 | 23.9 | 0.2606 | N/R | 32 |
| $BaTiO_3$ Whiskers | 0.3 μm | 30 | PVDF | Dispersant & Poling | 3-0 | 90.7 | 0.0746 | N/R | 32 |
| $BaTiO_3$ | 0.975 μm | 75 | Epoxy | Dispersant | 3-0 | 90 | N/R | N/R | 14 |
| $BaTiO_3$ | N/R | 10 - 40 | Epoxy | N/R | 3-0 | 27 | ~0.03 | N/R | 33 |
| $mBaTiO_3$ | N/R | 10 - 40 | Epoxy | Doped $BaTiO_3$ | 3-0 | 44 | ~0.03 | N/R | 33 |
| $BaTiO_3$/ PMN-PT | 0.1μm/ 1.8 μm | 85 | Epoxy | Surfactant | 3-0 | 150 | N/R | N/R | 34 |
| $BaTiO_3$ | 2 μm – 300μm | 0 - 60 | PP & Epoxy | N/R | 3-0 | 120 | ~0.05 | N/R | 35 |
| $BaTiO_3$ | 1.14 μm | N/R | PMMA | Silane Coupling Agent | 3-0 | N/R | N/R | N/R | 11 |
| $BaTiO_3$ | 10 nm | N/R | MTPT | In-Situ Particles | 3-0 | 5.2 | N/R | N/R | 36 |
| $BaTiO_3$ | 25 nm | N/R | PSS | N/R | 3-0 | N/R | N/R | N/R | 30 |
| $BaTiO_3$ | 7 μm – 9 μm | 10 - 25 | Epoxy | N/R | 3-0 | ~12. 5 | ~0.2 | N/R | 37 |
| $BaTiO_3$ | 0.5 μm – 1 μm | 5 - 35 | TMPTA | N/R | 3-0 | ~40 | N/R | N/R | 12 |
| $BaTiO_3$ | 20 nm – 3 μm | 40 | PVDF | Poling | 3-0 | ~500 | ~0.6 | N/R | 19 |
| $BaTiO_3$ | ~10 nm | N/R | SBS | In-Situ Particles | 3-0 | N/R | N/R | N/R | 25 |
| $BaTiO_3$ | ~5 nm | N/R | SBS & S-MAH | In-Situ Particles | 3-0 | N/R | N/R | N/R | 24 |
| $BaTiO_3$ | ~0.1 μm – 0.5 μm | 3 - 14 | t-PDMS | DPA & Poling | 3-1 | ~7 | ~0.4 | N/R | 22 |
| $BaTiO_3$ | N/R | 5 & 10 | PANI | Poling | 3-0 | N/R | N/R | N/R | 27 |
| $BaTiO_3$ | N/R | 60 | Epoxy | Silane Coupling Agent | 3-0 | 40 | 0.035 | N/R | 13 |
| $BaTiO_3$ | N/R | ~15 - 20 | PI | Poling | 3-0 | ~9.5 | 0.011 | N/R | 38 |

**Table 1 Abbreviations**

| | | | |
|---|---|---|---|
| $BaTiO_3$ | Barium Titanate | PMN-PT | Lead Magnesium Niobate-Lead Titanate |
| Dia. | Diameter | PP | Polypropylene |
| DPA | Dielectrophoretic Assembly | PSS | Polystrene Sulfonic Sodium |
| $mBaTiO_3$ | Modified Barium Titanate | PVDF | Polyvinylidene fluoride |
| MTPT | Methacryltriisopropoxytitanium | Ref. No. | Reference Number |
| N/R | Not Reported | S-MAH | Poly-(styrene-co-maleic anhydride) |
| PANI | Polyaniline | SBS | Polystyrene-polybutadiene-polystyrene |
| PI | Polyimide | t-PDMS | Telechelic polydimethylsiloxane |
| PMMA | Poly(methyl methacrylate) | TMPTA | Trimethylolpropane triacrylate |

## *1.6 Dissertation Objectives*

Upon completion of the literature review there were several interesting questions that remained to be answered. It can be seen from Table 1 that mechanical property data on dielectric composite materials is under-reported or nonexistent. One objective of this dissertation research is to determine the optimum combination of parameters required to create a $BaTiO_3$/polymer composite, with a high dielectric constant, low dielectric loss, and sound structural properties. Another objective is to determine which parameters have the greatest impact on the dielectric and mechanical properties of the material. In order to develop $BaTiO_3$/polymer composite materials suitable for use as structural capacitors, allowing the removal of discrete capacitors, these parameters must be investigated and optimized.

# *Chapter 2: Composite Materials*

Composite specimens were made using barium titanate ($BaTiO_3$) particles with an average size of 100 nm and 200 nm as the filler and EPON™ Resin 862 (diglycidyl ether of bisphenol F) was used as the matrix. The crystal structure of the 100 nm particles is cubic and it is tetragonal for the 200 nm particles. A silane coupling agent and a viscosity modifier were also used in this research to improve particle bonding to the matrix, to decrease particle agglomeration and to reduce the viscosity of the particle/resin mixture.

## *2.1 Particles*

Barium titanate has a high dielectric constant, well-documented material properties, is relatively inexpensive, and is readily available at high purities[39-56]. For these reasons, it was chosen as the particle material in this research. $BaTiO_3$ was the first ceramic material in which the ferroelectric phenomenon was observed. It is referred to as a perovskite because it is isostructural with the mineral perovskite ($CaTiO_3$)[5]. $BaTiO_3$ assumes two basic structures, one is a ferroelectric form at certain temperatures and the other is a non-ferroelectric form. A ferroelectric material exhibits spontaneous polarization, which is polarization in the absence of an electric field[57]. The temperature at which the ferroelectric switching occurs is called the Curie Temperature ($T_C$) or the Curie point. Above 1460ºC $BaTiO_3$ has a stable hexagonal form that can remain metastably at room temperature; however, a reconstructive transformation to cubic form usually takes place below 1460ºC. The Curie point ($T_C$) is approximately 130ºC. Above $T_C$ = 130ºC but below 1460ºC, the unit cell of $BaTiO_3$ is cubic. In its cubic form, $BaTiO_3$ is non-ferroelectric. Below $T_C$ the structure distorts slightly, assuming a tetragonal form, and has a dipole moment along the c direction. This spontaneous polarization along the c direction makes the tetragonal form of $BaTiO_3$ ferroelectric. Additional transformations occur at and below

freezing temperatures from tetragonal to orthorhombic at approximately 0ºC and from orthorhombic to rhombohedral at about -80ºC. Figure 10 illustrates the structural transformations of $BaTiO_3$. The arrows indicate the polarization direction.

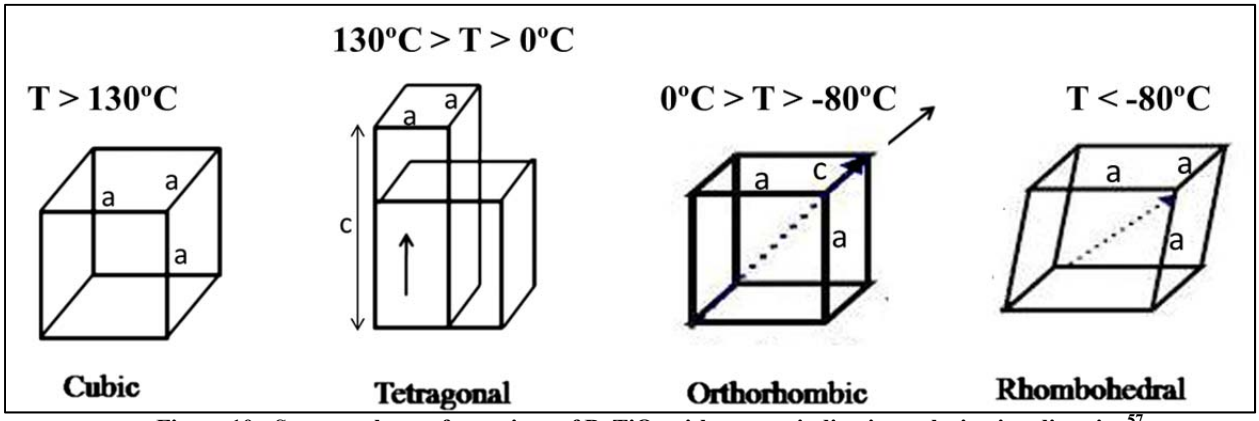


**Figure 10: Structural transformations of $BaTiO_3$ with arrows indicating polarization direction[57]**

Many researchers have studied the effect of particle size on the dielectric properties of $BaTiO_3$. There is believed to be a critical size at which $BaTiO_3$ particles exhibit strong ferroelectric and dielectric properties but the critical size listed in the literature seems to range from 15 nm to 200 nm[58]. Hsiang et al.[19] investigated the effect of $BaTiO_3$ particle size on the dielectric properties of $BaTiO_3$/PVDF composites and found that dielectric constants at frequencies below 1 kHz increased greatly with frequency for particles smaller than 58 nm and the variation of dielectric constant with frequency became flat for composites with particles larger than 58 nm. This result was attributed to space charge effects at the interface between the particles and the matrix, and these effects were believed to dominate for smaller particles due to increased defects in the particles.

Lee et al.[25] pointed out that $BaTiO_3$ shows a ferroelectric to non-ferroelectric phase transition when its size is reduced below 100 nm but that while not ferroelectric in its cubic form, $BaTiO_3$ still has a high dielectric constant. This was evident in the work performed by Wada et

al.[59] who produced $BaTiO_3$ particles using hydrothermal techniques and found the maximum dielectric constant of 15,000 resulted from particles with a size around 70 nm. Xu and Gao[60] produced $BaTiO_3$ particles with hydrothermal techniques and concluded that it was the tetragonal content of the particles, and not the size, that significantly affected the dielectric constant of the particles. They obtained the highest dielectric constant of 6200 and the lowest dielectric loss results with particles 80 nm in size with 40% tetragonal content.

Both 100 nm and 200 nm particles were used in this research. The 100 nm particles have a cubic crystal structure and the 200 nm particles have a tetragonal crystal structure. Figure 11 shows the unit cells of cubic and tetragonal $BaTiO_3$. The particles were provided by Nanostructured and Amorphous Materials, Inc., Houston, TX, and the properties of the particles are shown in Table 2.

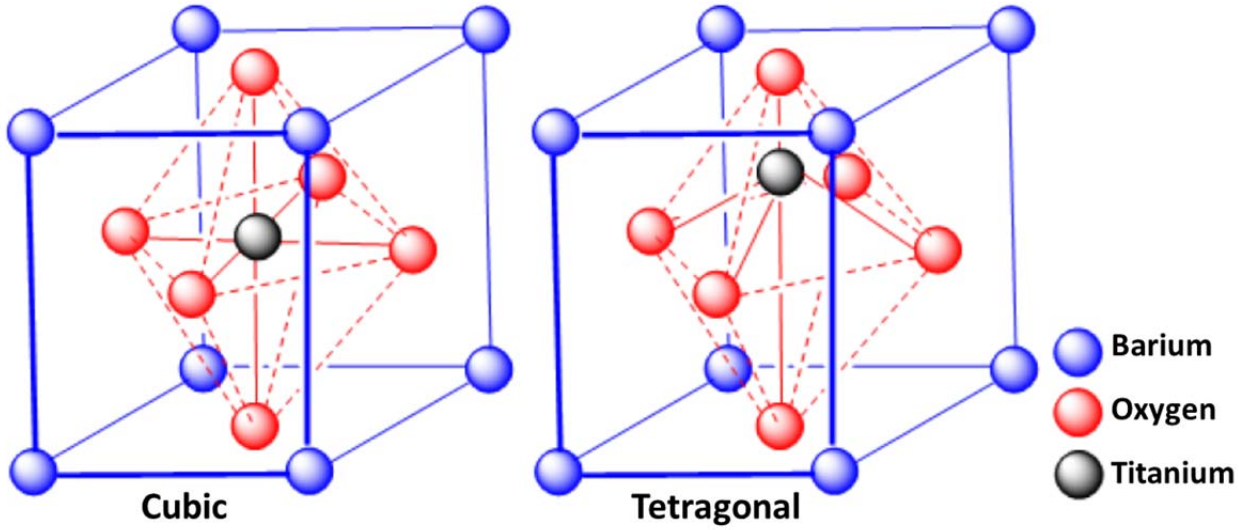


**Figure 11: Unit Cells of Cubic (left) and Tetragonal (right) $BaTiO_3$[8]**

Note that in the cubic phase, $BaTiO_3$ does not have an innate dipole, and is non-ferroelectric. Instead, it is paraelectric. Paraelectric materials are those that polarize in the presence of an electric field; however, they are not left with a residual polarization once the field is removed because they do not have a mobile charged atom with more than one stable lattice

position[61]. In the tetragonal phase, $BaTiO_3$ has a permanent dipole that aligns with the external electrical field, and still maintains its polarization even when the electric field is removed, thus it is ferroelectric. Polarization of tetragonal $BaTiO_3$ is often depicted by a shift in the central titanium; however, there is also concerted movement of the ions, including the oxygen ions, which shift slightly around the titanium[8].

**Table 2: Barium Titanate Particle Properties[62,63]**

| ***Barium Titanate Particles ($BaTiO_3$)*** | | | | |
|---|---|---|---|---|
| **Average Particle Size 100 nm** | | | **Average Particle Size 200 nm** | |
| Measurement | Value | | Measurement | Value |
| Purity | 99.9% | | Purity | 99.9% |
| Specific Surface Area | 10 - 11 $m^2/g$ | | Specific Surface | 5.0-5.6 $m^2/g$ |
| Morphology | Spherical | | Morphology | Spherical |
| Crystal Structure | Cubic | | Crystal Structure | Tetragonal |
| Color | White | | Color | White |
| True Density | 5.85 g/cc | | True Density | 5.85 g/cc |

## *2.2 Polymer Matrix*

The polymer matrix chosen for this research was EPON™ Resin 862 with EPIKURE ™ Curing Agent 3230, provided by Hexion Specialty Chemicals, Columbus, OH. EPON™ 862 is a bisphenol F-based epoxy resin that is formulated for high resistance to fatigue and microcracking[64]. This resin is widely used in applications varying from the marine industry to aerospace. The chemical structure of EPON™ Resin 862 is shown in Figure 12.

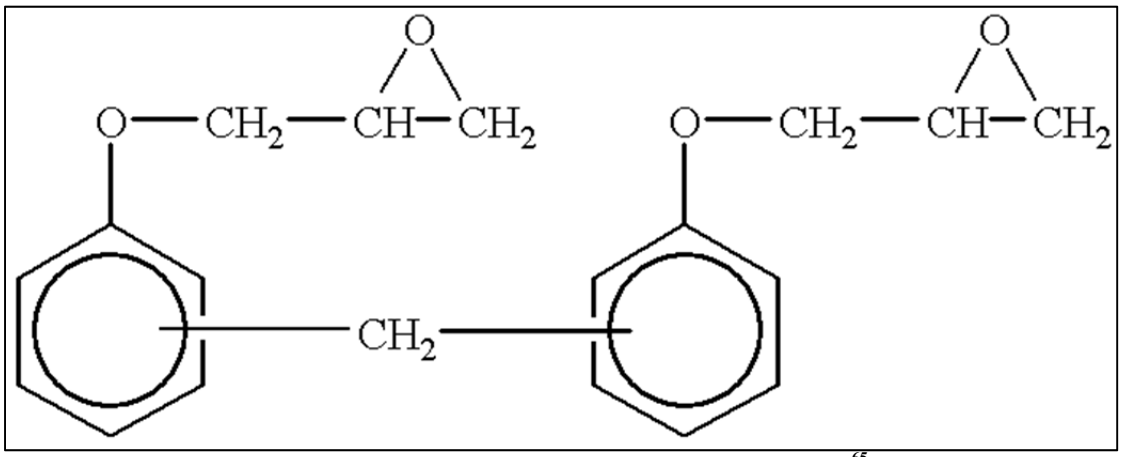

**Figure 12: Chemical Structure of EPON™ Resin 862[65]**

For dielectrophoretic assembly (DPA), the matrix material should be insulating, have a low dielectric constant and loss (compared to the filler material), resist electrical breakdown, and allow a sufficient time before curing to allow movement and alignment of the particles[10]. Its low viscosity at room temperature, low dielectric constant and loss (compared to the $BaTiO_3$ particles) and long gel time made EPON™ Resin 862 suitable for this research. The properties of the resin and curing agent can be found in Tables 3 and 4, respectively.

**Table 3: EPON™ Resin 862 Properties[66]**

| ***EPON™ Resin 862*** | | | |
|---|---|---|---|
| **Property** | **Units** | **Value** | **Test Method** |
| Weight per Epoxide | g/eq | 165 – 173 | ASTM D1652 |
| Density @ 25$^{O}$C | lb/gal | 9.8 | ASTM D1475 |
| Viscosity 25°C | P | 25 – 45 | ASTM D445 |
| Color | Pt-Co | 200 max | ASTM D1209 |

**Table 4: EPIKURE Curing Agent 3230 Properties[67]**

| ***EPIKURE™ Curing Agent 3230*** | | | |
|---|---|---|---|
| **Property** | **Units** | **Value** | **Test Method** |
| Amine value | mg/g | 454-488 | ASTM D2896 |
| Density | lb/gal | 7.9 | ASTM D1475 |
| Viscosity 25°C | cP | ~9 | ASTM D2196 |
| Color | Pt-Co | 30 | ASTM D1209 |

## 2.3 Coupling Agent

Researchers have found that the surfaces of $BaTiO_3$ particles contain hydroxyl groups that are hydrophilic in nature and most organic polymer resins are hydrophobic. As a result of this incompatibility, when the particles are mixed with the resin they tend to agglomerate and separate from the resin. Silane coupling agents have been used to make the particles more compatible with organic solvents and resins. In this research, the EPON™ Resin 862 is hydrophobic and rejects hydrogen bonding therefore 3-(trimethoxysilyl)propyl methacrylate, hereafter referred to as TMSPM, was used to functionalize the $BaTiO_3$ particles. In addition to stabilizing the particles during processing, this silane coupling agent has also been shown to be compatible with polymer matrices[68]. TMSPM has a hydrolysable group ($-Si(OCH_3)_3$) that can be hydrolyzed and bonded to the surface of the nanoparticles and an unsaturated carbon-carbon double bond that can be copolymerized with the resin[13,29,69]. The TMSPM was provided by Sigma-Aldrich, Saint Louis, MO. The chemical structure is shown in Figure 13 and the material properties are shown in Table 5.

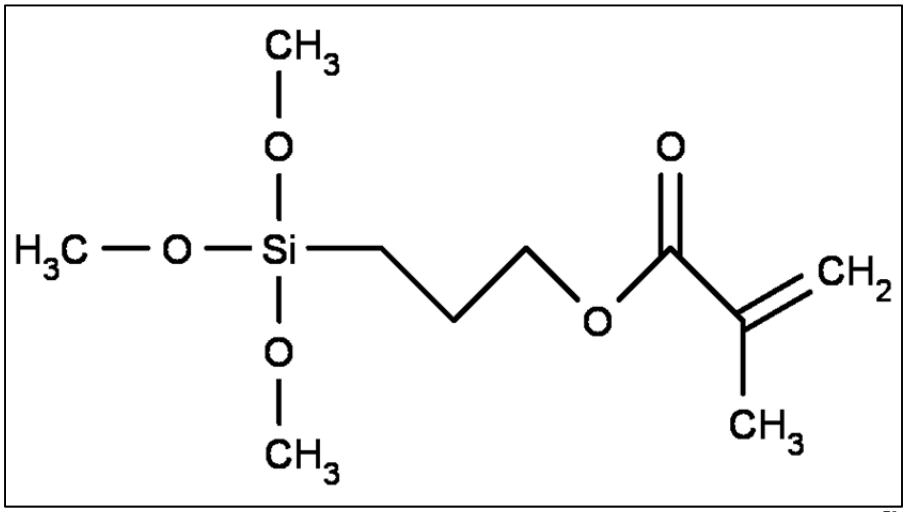


**Figure 13: Chemical Structure of 3-(Trimethoxysilyl)propyl Methacrylate (TMSPM)[70]**

Table 5: 3-(Trimethoxysilyl)propyl Methacrylate (TMSPM) Properties[70]

| *3-(Trimethoxysilyl)propyl Methacrylate* | |
|---|---|
| **Measurement** | **Value** |
| Formula | $C_{10}H_{20}O_5Si$ |
| Molecular Weight | 248.35 g/mol |
| Density @ 25$^{O}$C | 1.045 g/cc |
| Boiling point | 190 °C |
| Water solubility | Soluble |

## *2.4 Viscosity Modifier*

Since this research involves relatively high volume fractions of particle filler (25% and 50%), a viscosity modifier was used to improve processing of the resin/particle mixture. HELOXY™ 61 Epoxy Functional Modifier, provided by Hexion Specialty Chemicals, Columbus, OH, was the modifier used. While the chemical formula for this material is proprietary and was not provided by the manufacturer, generally reactive diluents include mono- and di-functional glycidyl ethers which can be used to reduce the viscosity of typical epoxy resins without causing significant changes in final physical properties. The reduced viscosity provides improved pigment/filler wetting and improved application properties[71]. The properties of this material are shown in Table 6.

Table 6: HELOXY™ 61 Epoxy Functional Modifier Properties[72]

| *HELOXY™ 61 Epoxy Functional Modifier* | | | |
|---|---|---|---|
| **Property** | **Units** | **Value** | **Test Method** |
| Weight per Epoxide | g/eq | 145-155 | ASTM D1652 |
| Density | lb/gal | 7.5 | ASTM D1475 |
| Viscosity 25°C | cP | 1-2 | ASTM D2196 |
| Color (max) | Pt-Co | < 1 | ASTM D1209 |

# *Chapter 3: Composite Manufacturing*

A composite is a combination of two or more materials, in which each material remains uniquely identifiable in the mixture[73]. Composites are designed to display a combination of the best characteristics of each of the component materials. This is known as the principle of combined action and it is the idea that a better combination of properties can be achieved through the thoughtful combination of two or more distinct materials[58]. In this research, multifunctional composite materials were developed by combining barium titanate ($BaTiO_3$) particles and an epoxy polymer. The goal of combining the two materials is to develop a composite that has greater dielectric properties than an epoxy polymer, with better toughness than a brittle, monolithic, $BaTiO_3$ ceramic.

## *3.1 Designed Experiments*

Designed experiments are used extensively in manufacturing engineering, as a method to improve the quality of products. They help identify the key variables, or factors, that influence the desired quality characteristics[74]. Designed experiments provide a systematic approach to varying the controllable factors of a process and observing the effect these factors have on the product. Each factor may also have levels, such as high and low, or low, medium, and high. Designed experiments also identify the levels of these controllable factors that reduce variation and optimize process performance. Manufacturing processes usually have several factors, so factorial experimental designs are used[75]. The term factorial design means that in each complete trial or experiment, all combinations of the levels and factors are investigated[75]. The $2^k$ factorial design is used very often, where the [2] refers to the number of levels and the[k] refers to the

number of factors[75]. For example, if an experiment has 2 levels and 3 factors, it would be a $2^3$ factorial design and it has eight ($2^3 = 8$) factor-level combinations to be investigated.

In the early 1980's, Professor Genichi Taguchi introduced his approach to using experimental designs[75]. This approach is often referred to as the Taguchi Design of Experiments Methods, or the Taguchi Methods. Instead of conducting full factorial experiments, a reduced factorial or an orthogonal matrix method serves as the basis for the Taguchi Methods[75, 76]. An orthogonal matrix is a generalized Latin square and a Latin square is used as the basis of experimental procedures in which it is desired to control or allow for two sources of variability while investigating a third[77],[78]. The full nomenclature for an orthogonal array is $L_a(b^c)$, in which [L] stands for Latin square, [a] is the number of test trials, [b] is the number of levels, and [c] is the number of factors[79]. Using the same example of an experiment with 2 levels and 3 factors, an $L_4(2^3)$ orthogonal array would be used. In this case, there are only four factor-level combinations to be investigated, as opposed to eight in a full factorial design.

For this research, composite specimens were manufactured using the Taguchi Methods. Two parametric studies were performed and the factors, hereafter referred to as the parameters, investigated include the volume fraction of $BaTiO_3$ particles, the size/crystal structure of the particles, and the application of an electric field during the composite curing process (dielectrophoretic assembly). The 100 nm particles have a cubic crystal structure, and will hereafter be referred to as 100 nm (cubic). The 200 nm particles have a tetragonal structure, and will hereafter be referred to as 200 nm (tetragonal). Two levels of each parameter were tested; therefore, a Taguchi $L_4(2^3)$ orthogonal array was used. Table 7 shows the basic Taguchi matrix used for this research. The choice of these manufacturing parameters was informed by the literature referenced in Section 1.5 of this dissertation.

**Table 7: Taguchi Orthogonal Array $L_4(2^3)$[75]**

| *Experiment Number* | *Particle Volume Fraction ($V_f$)* | *Dielectrophoretic Assembly (DPA)* | *Particle Size/Crystallography* |
|---|---|---|---|
| **1** | 1 | 1 | 1 |
| **2** | 1 | 2 | 2 |
| **3** | 2 | 1 | 2 |
| **4** | 2 | 2 | 1 |

The two levels used in the parametric studies were high and low, or on and off. In Table 7, when the level of a parameter in the matrix is 1, the lowest level of that parameter was used. In this research that corresponds to 25% volume fraction of $BaTiO_3$ particles, 100 nm (cubic) $BaTiO_3$ particles, and DPA was not applied. When the level of a parameter in the matrix is 2, the highest level of that parameter was used. That corresponds to 50% volume fraction of $BaTiO_3$ particles, 200 nm (tetragonal) $BaTiO_3$ particles, and DPA was applied.

In parametric Study 1, DPA was applied in the plane of the mold used to manufacture composite specimens, and will hereafter be referred to as In-Plane DPA. In parametric Study 2, DPA was applied through the plane of the mold used to manufacture the composite specimens, and will hereafter be referred to as Through-Plane DPA. Although maximizing all of the parameters is not part of Taguchi's Design of Experiments Methods, a composite material with all of the parameters maximized was also created, and will hereafter be referred to as MAX. The parameters and levels used in the two parametric studies, as well as the MAX study, are shown in Table 8. Although MAX is shown in Table 8, it is not part of the parametric studies or the $L_4(2^3)$ orthogonal array. It is included in Table 8 for comparison only.

**Table 8: Parameters and Levels used for In-Plane DPA, Through-Plane DPA, and MAX Studies**

| *Experiment Number* | *Particle Volume Fraction ($V_f$)* | *Dielectrophoretic Assembly (DPA)* | *Particle Size/Crystallography* |
|---|---|---|---|
| **1** | 25% | Not Applied | 100 nm (cubic) |
| **2** | 25% | Applied | 200 nm (tetragonal) |
| **3** | 50% | Not Applied | 200 nm (tetragonal) |
| **4** | 50% | Applied | 100 nm (cubic) |
| **MAX** | 50% | Applied | 200 nm (tetragonal) |

## 3.2 *Particle Surface Functionalization*

The surfaces of metal oxides, such as $BaTiO_3$, have many defective sites which are typically terminated with hydroxyl groups (OH)[17]. These hydroxyl groups are hydrophilic in nature and most organic polymer resins, including the EPON™ Resin 862 used in this research, are hydrophobic. The hydrophobic polymer resin rejects hydrogen bonding, so a silane coupling agent, 3-(trimethoxysilyl)propyl methacrylate, hereafter referred to as TMSPM, was used to functionalize the $BaTiO_3$ particles. For successful particle functionalization, an electrophilic substitution must occur to replace the proton in the surface hydroxyl group with the binding hydrolysable group ($-Si(OCH_3)_3$) of the TMSPM, as shown in Figure 14.

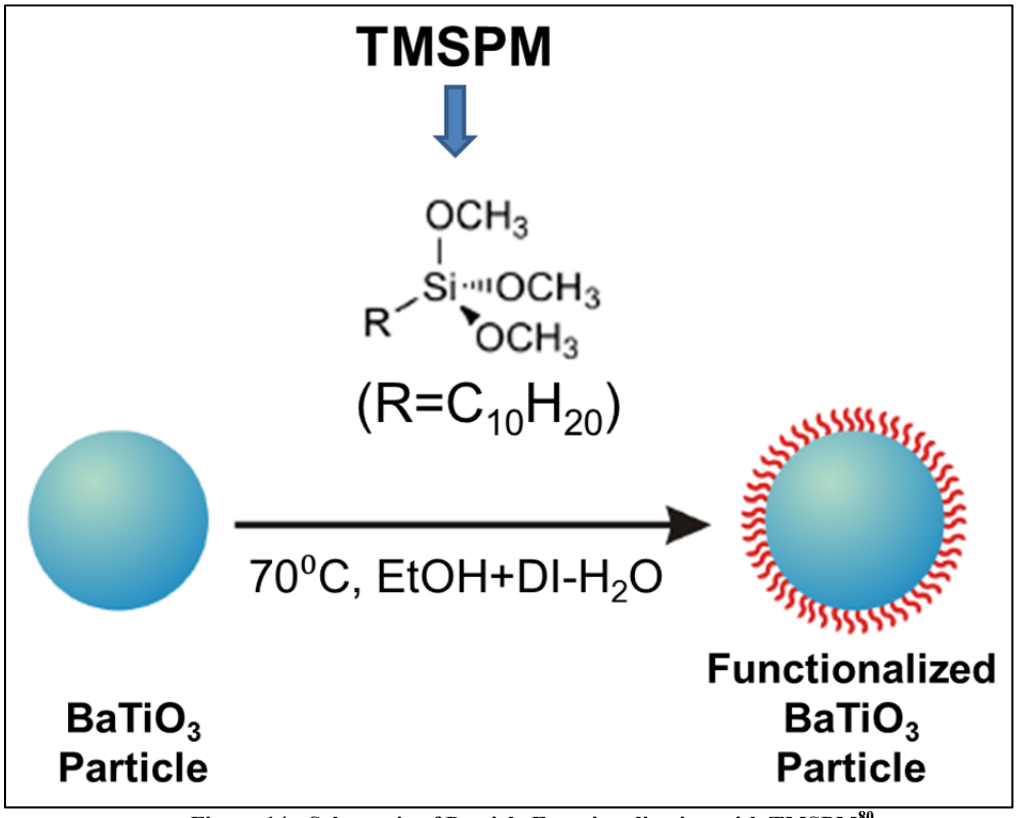


**Figure 14: Schematic of Particle Functionalization with TMSPM[80]**

The as-received $BaTiO_3$ particles were placed in a vacuum oven, heated to 200 ºC and held under vacuum for 12 hours. A mixture containing 40 g of the BaTiO3 particles, 5 ml of

de-ionized water (DI-$H_2O$), 95 ml of Ethyl Alcohol (EtOH) and 2.0 g of TMSPM was placed in a round-bottom flask and ultrasonically treated for 5 minutes. The flask containing the mixture was then placed inside a large beaker of silicon oil, and refluxed at 70ºC for 2 hours. After refluxing, the mixture was centrifuged using an Eppendorf International Model 5804R, and the liquid was de-canted. The particles were then rinsed 3 times with EtOH, and dried at room temperature, under vacuum, for 24 hours. The process is depicted in Figure 15.

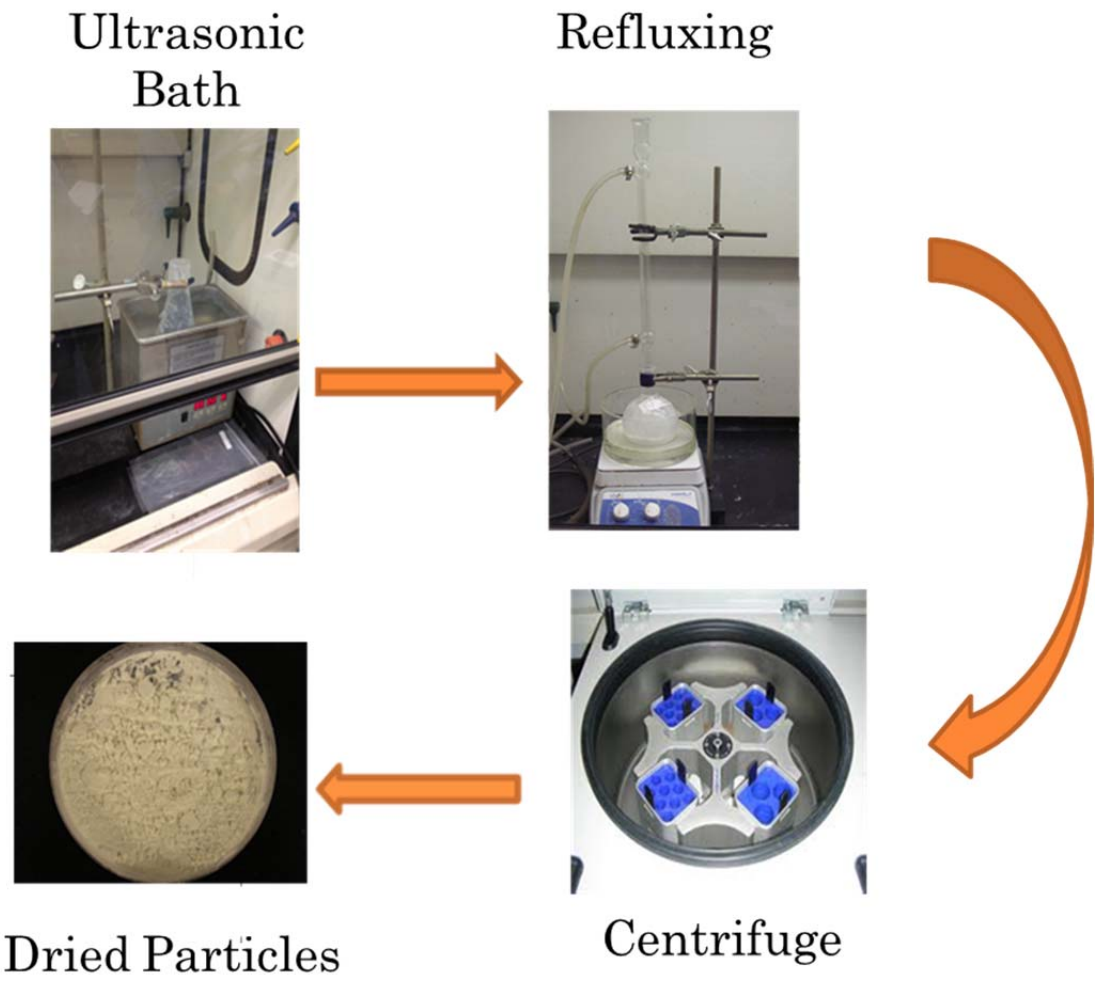


**Figure 15: Refluxing of $BaTiO_3$ and TMSPM**

Through hydrolysis and condensation, as shown in Figure 16, the silane group of the TMSPM was then grafted to the surface of the $BaTiO_3$ particles.

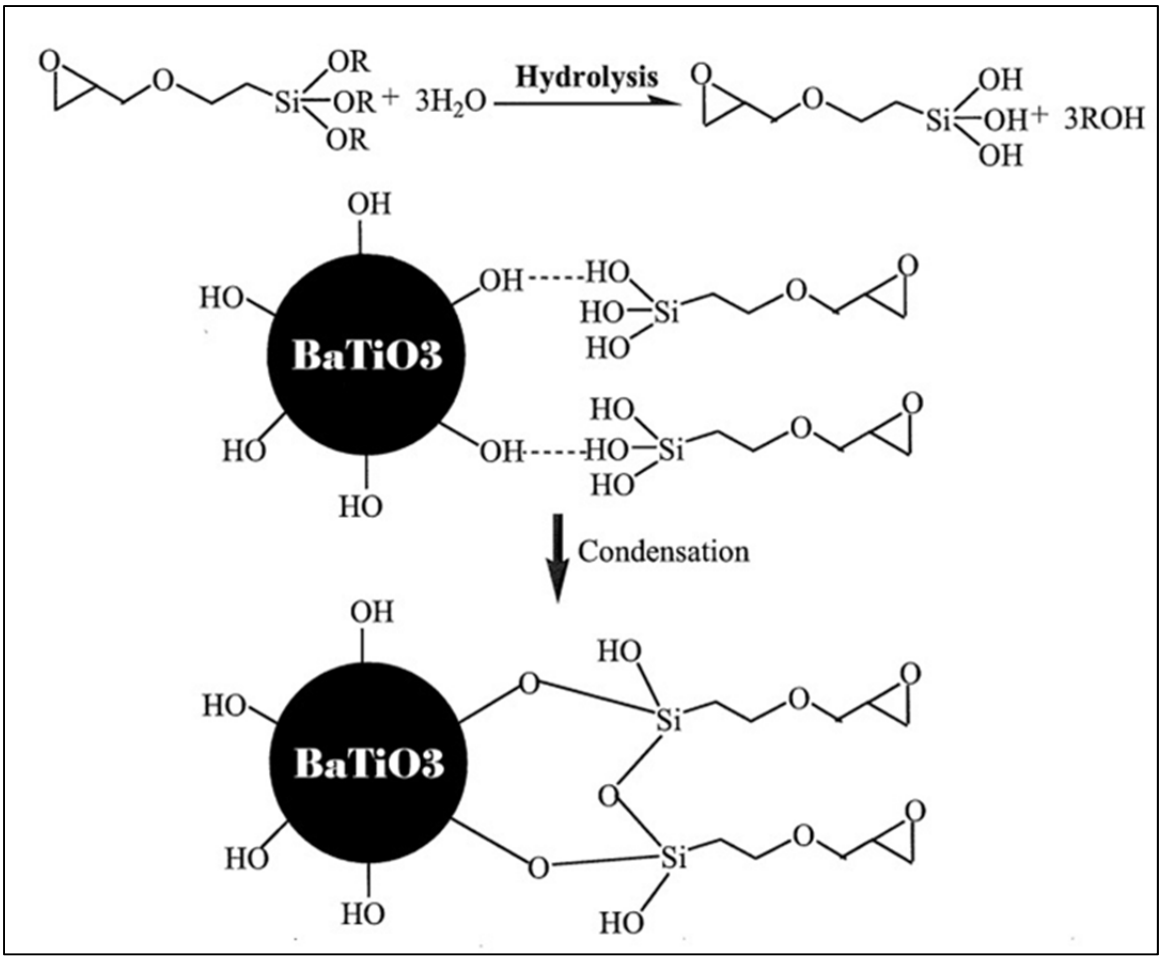


**Figure 16: Hydrolysis and Grafting of Silane onto $BaTiO_3$ Particle[79]**

### *3.2.1 Fourier Transform Infrared (FT-IR) Spectroscopy*

Fourier Transform Infrared (FT-IR) Spectroscopy was performed with a Jasco FT-IR 420 spectrometer to verify bonding of the TMSPM functional group to the particles. Spectra were recorded in absorbance mode under dried nitrogen flow at 10 cc per minute. To test the particles, KBr pellets were prepared with 300 mg of KBr to 3 mg of the sample. Both as-received $BaTiO_3$ and TMSPM treated $BaTiO_3$ particles were tested. Both the functionalized 100 nm and 200 nm particles showed peaks at 1085$cm^{-1}$ and 1720 $cm^{-1}$. These peaks correspond to

the Si-O and the C=O vibrations of the TMSPM, respectively[80]. Thus the silane groups were successfully grafted onto the $BaTiO_3$ particles. The 200 nm sample used for FT-IR analysis had been rinsed but was not completely dry at the time of testing, thus a peak at 1045 $cm^{-1}$ is shown which corresponds to the C—O stretch of the residual EtOH used for rinsing the particles[81]. The FT-IR spectra for the 100 nm and 200 nm particles are shown in Figures 17 and 18, respectively.

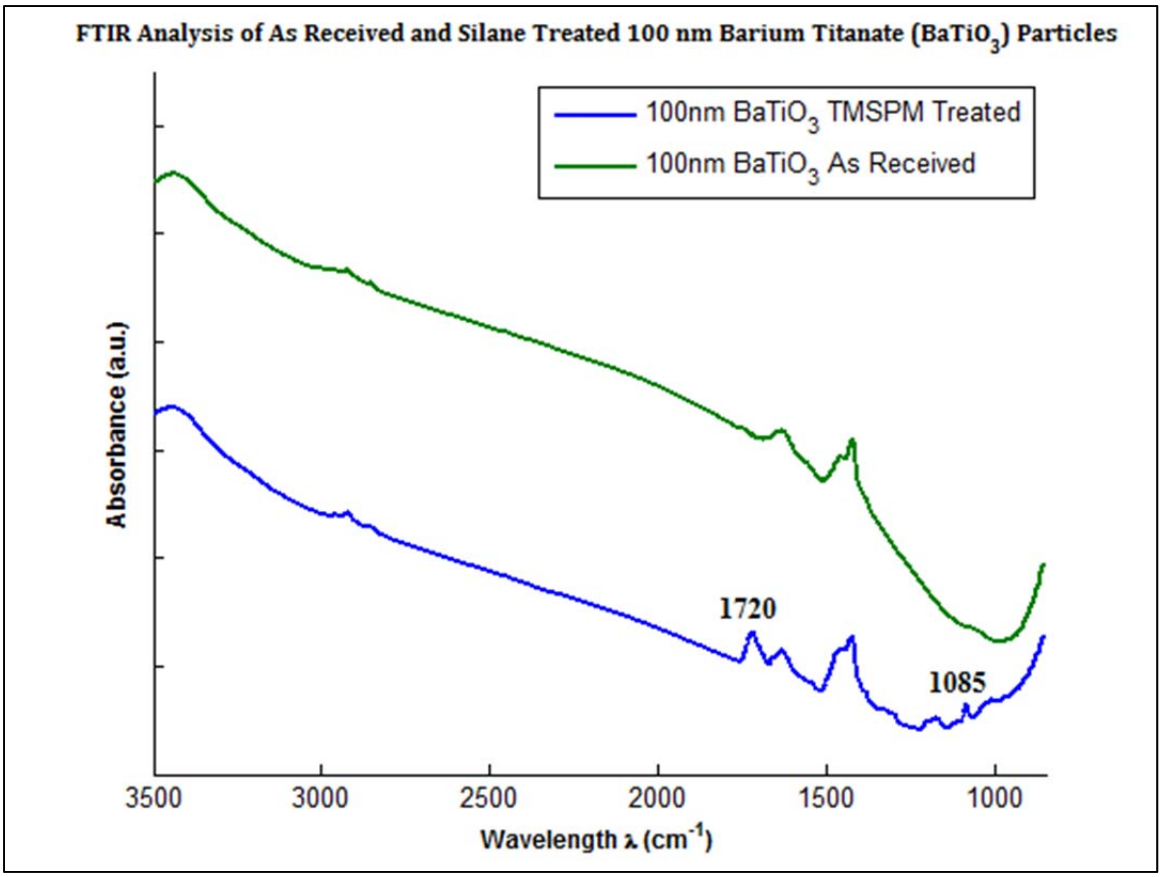


**Figure 17: FT-IR Spectra of 100 nm $BaTiO_3$ Particles**

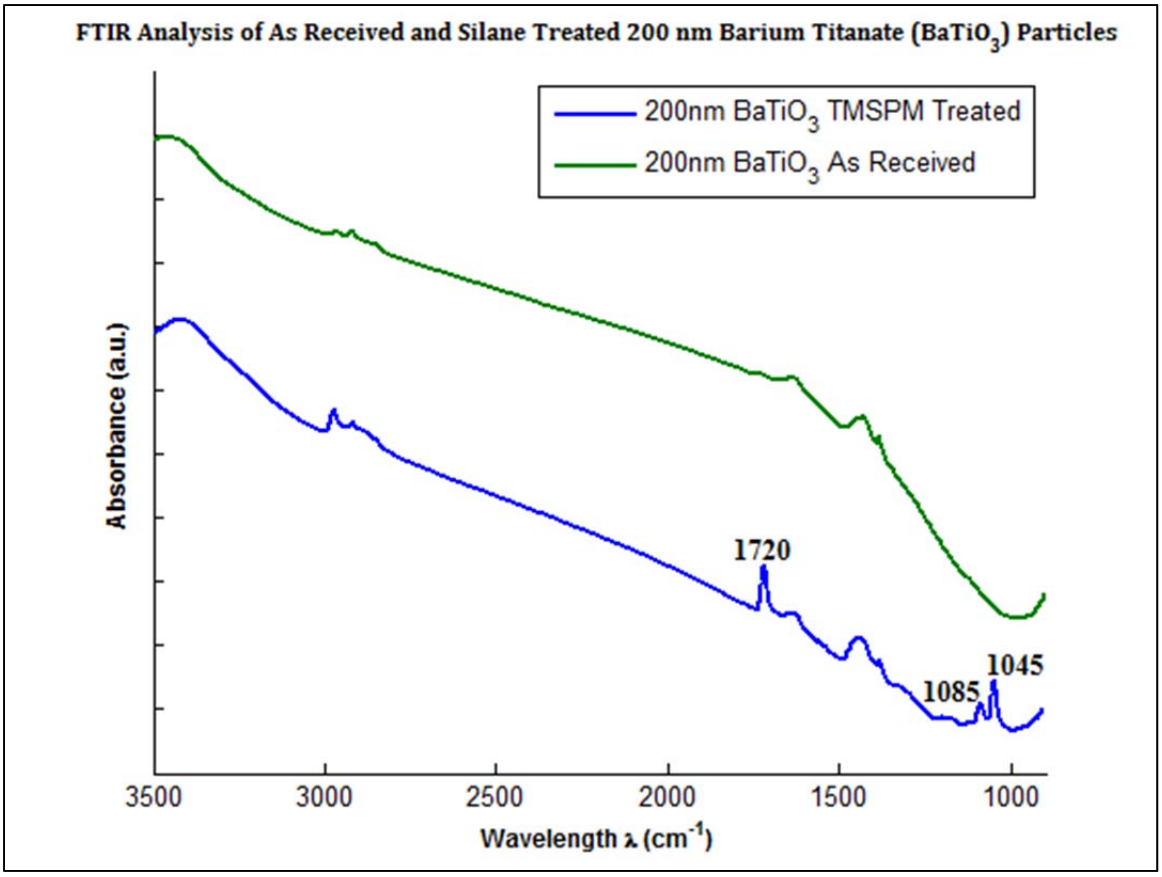


**Figure 18: FT-IR Spectra of 200 nm $BaTiO_3$ Particles**

## *3.3 Test Specimen Manufacturing*

Following the Taguchi test matrix shown in Table 8, test specimens for the In-Plane DPA and the Through-Plane DPA parametric studies were made, along with test specimens for the MAX study. A total of 30 ml of resin and particles were prepared for each experiment. The Taguchi test matrix dictated the volume fraction of particles and resin used in each experiment. HELOXY™ 61 Epoxy Functional Modifier was added to each experiment, at 5% by weight of the resin. Samples of unaltered EPON™ Resin 862 and EPON™ Resin 862 with 5% by weight of HELOXY™ 61 modifier, were also prepared.

### 3.3.1 Resin/Particle Processing

In this research, centrifugal mixing and ultrasonic treatment were used to combine the resin and particles. The functionalized $BaTiO_3$ particles were added to the EPON™ 862 resin. The HELOXY™ 61 modifier was also added at 5% by weight of the resin. The particles, resin and modifier were then placed inside a THINKY AR-250 conditioning mixer, supplied by Adaptive Energy in Tacoma, WA, for mixing and bubble removal. The THINKY AR-250 mixer rotates the material inside a container while revolving it on a set radius to produce a huge and continuous centrifugal force that mixes and forces out resultant bubbles.

Following processing in the THINKY AR-250 mixer, the material was placed inside an ultrasonic bath and treated for 1 hour. After ultrasonic treatment, the EPIKURE ™ Curing Agent 3230 was added at 32% by weight of resin, and the mixture was returned to the THINKY AR-250 mixer, for final conditioning.

### 3.3.2 Curing Composites with 3-0 Connectivity

As detailed in Section 1.5.1 of this dissertation, two numbers are used to designate the connectivity of diphasic composites. If the composite has particulate filler material that is homogeneously dispersed in a polymer matrix, it would be described as having 3-0 connectivity, where the 3 indicates the matrix material is continuous in all three directions and the zero indicates the filler material is not continuous in the x, y, or z directions. For experiments 1 and 3, from the Taguchi test matrix shown in Table 8, composite specimens with 3-0 connectivity were produced.

After adding the curing agent, the resin/particle mixture was poured into a mold made from room-temperature vulcanizing (RTV) silicone rubber, which was affixed to an aluminum caul plate. The mold had 22 mm diameter disc impressions to prepare specimens for dielectric

property characterization and microtensile test impressions made to the American Society for Testing and Materials (ASTM) D 1708—06a specification, to prepare specimens for mechanical property characterization. A drawing of the microtensile test specimen is shown in Figure 19.

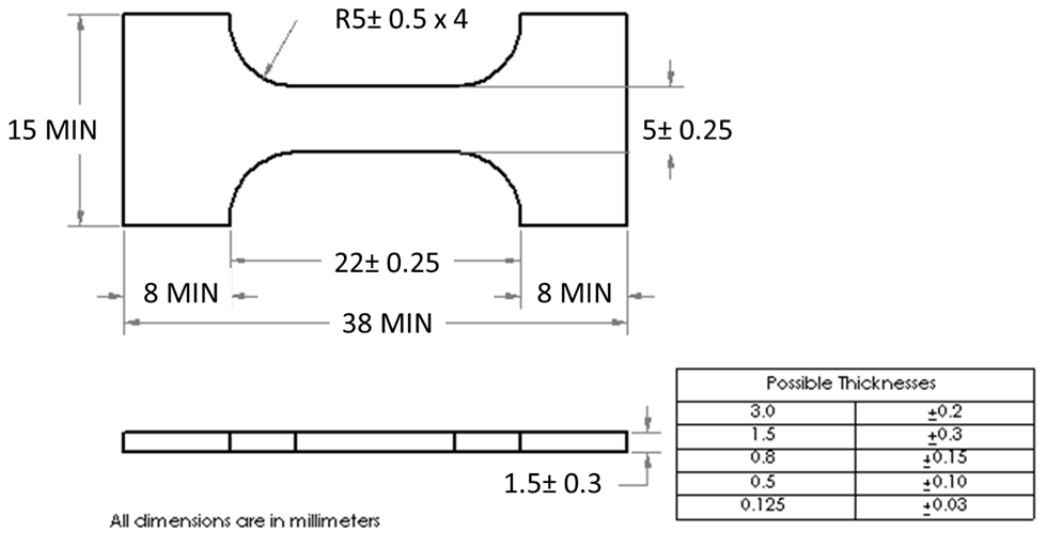


| Possible Thicknesses | |
|---|---|
| 3.0 | ±0.2 |
| 1.5 | ±0.3 |
| 0.8 | ±0.15 |
| 0.5 | ±0.10 |
| 0.125 | ±0.03 |

**Figure 19: ASTM Standard D 1708-06a Microtensile Specimen**[82]

The mold was then placed inside a vacuum oven and held at 28 inHg for 15 minutes to de-gas the viscous mixture, as shown in Figure 20.

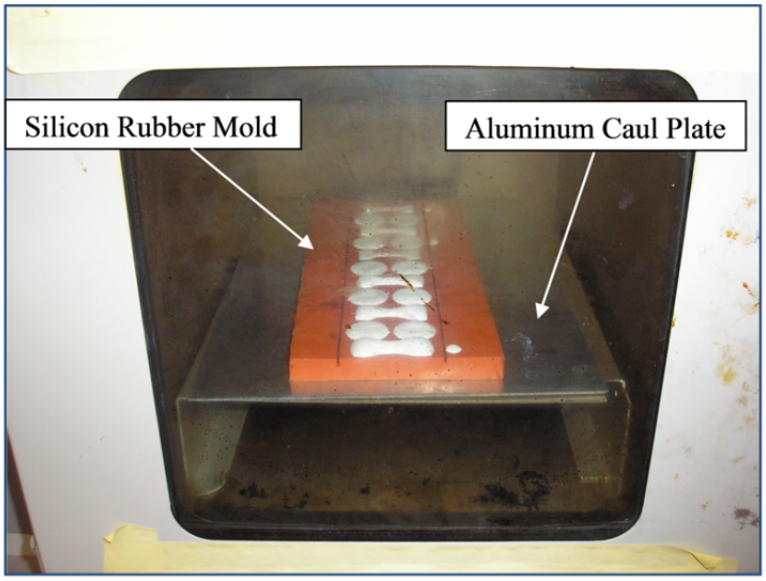


**Figure 20: De-gassing Resin/Particle Mixture in Mold for 3-0 Composite Test Specimens**

Following de-gassing, the composite specimens were allowed to cure, at room temperature, for 24 hours and post-cured at 121°C for 1 hour. Once the test specimens cooled to room temperature, they were de-molded and the surfaces were smoothed with 1000 grit sand paper. Sanding strokes were made in the direction parallel to the long axis of the tensile test specimens.

### *3.3.3 Curing Composites with Quasi 3-1 Connectivity*

As detailed in Section 1.5.2 of this dissertation, the application of DPA changes the connectivity of the composite from 3-0 to 3-1. The composites are referred to as quasi 3-1, because even though the particles align and chain together, all of the polymer is not removed from between the particles, thus the connectivity of the particles is not completely continuous. In experiments 2 and 4 for this research, DPA was used to align the $BaTiO_3$ particles in the epoxy resin matrix. Compounding of the resin-particle mixture was the same as detailed in Section 3.3.1; however, once the material was poured into the silicone rubber mold, an electric field was applied.

#### *3.3.3.1 In-Plane DPA*

For In-Plane DPA, electrodes were place inside the silicone mold and spaced 48 mm apart. The electrodes were arranged such that particle alignment would occur in the plane of the composite specimens, and in the direction parallel to the long axis of the tensile test specimens. The electrodes were attached to lead wires with one lead wire connected to the input signal source, and the other lead wire connected to ground. A drawing of the In-Plane configuration is shown in Figure 21 and pictures of the set-up are shown in Figure 22.

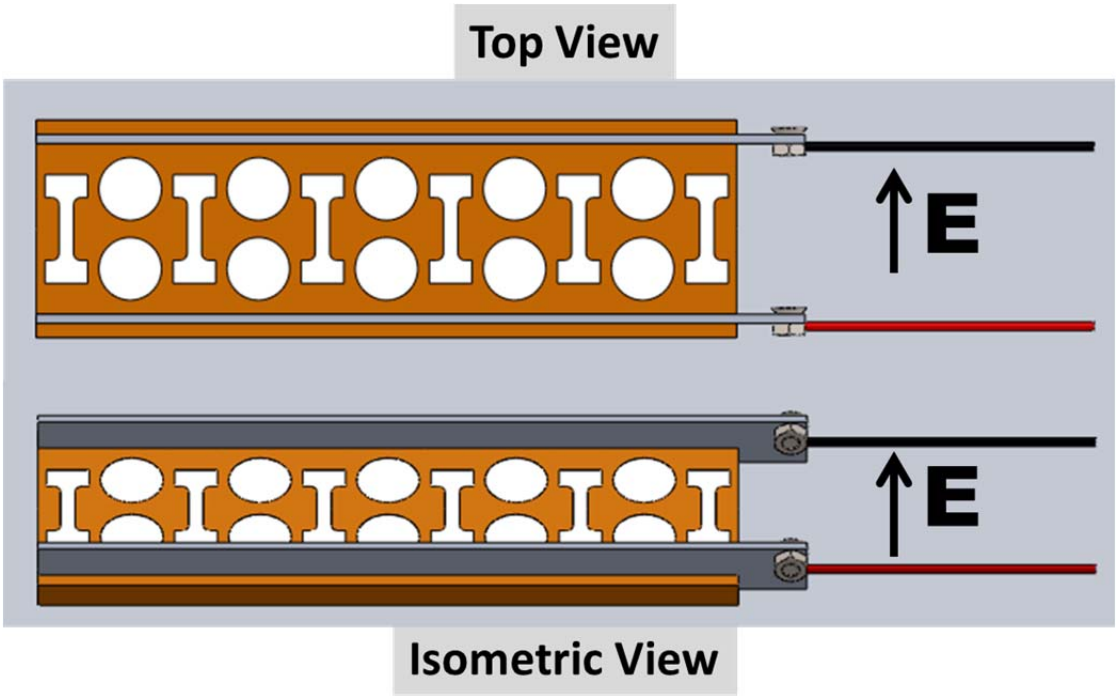


**Figure 21: Top and Isometric Views of In-Plane DPA**

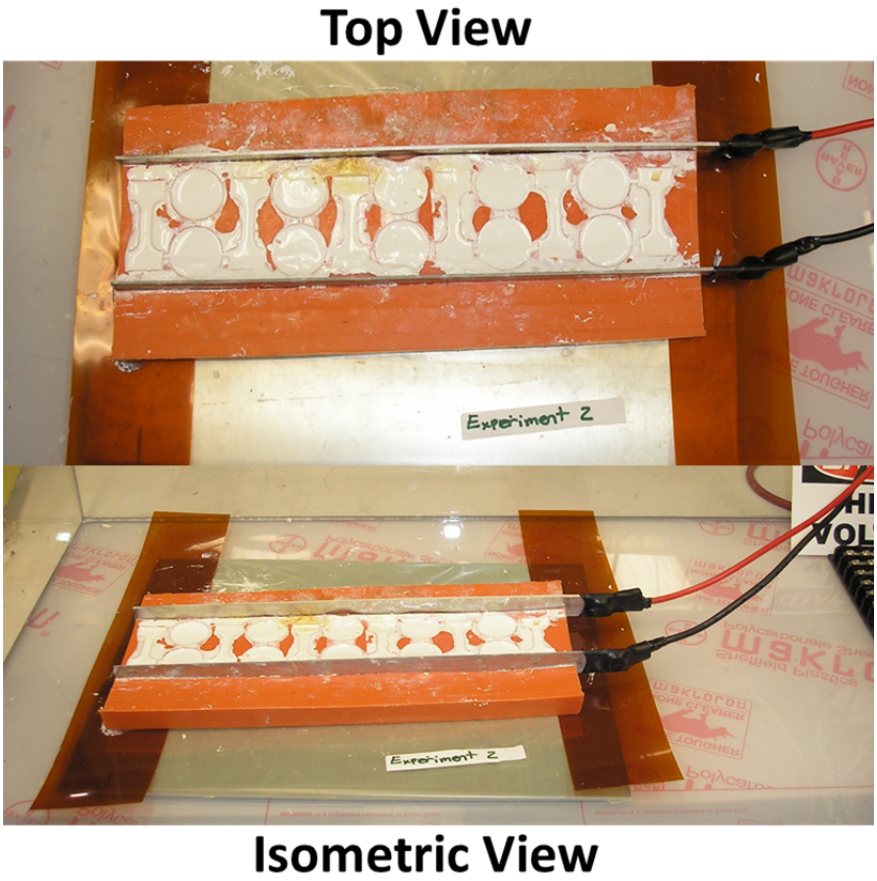


**Figure 22: Top and Isometric View Photographs of the In-Plane DPA Set-Up**

Using a WaveTek (Model 10 MHz DDS) function generator, a square wave with an amplitude of ± 7.5 V and a frequency of 650 Hz was sent to a TREK Model 20/20A amplifier. The amplifier increased the input signal to a maximum peak voltage of 15 kV. The distance between the electrodes was 48 mm, thus the maximum electric field applied during In-Plane DPA was 0.63 MV/m. The In-Plane DPA experiments were placed inside an electrical isolation box and the field was applied for 24 hours, as the composites cured at room temperature.

#### *3.3.3.2 Through-Plane DPA*

For the Through-Plane DPA experiments, the bottom caul plates for experiments 2 and 4 served as electrodes. Another aluminum plate was placed above experiments 2 and 4, and served as the top electrode. A lead wire from the top electrode was connected to ground. The top electrode was 12.7 mm above the bottom caul plates and this distance was set by fiberglass spacers that were affixed to the top electrode. The bottom, aluminum caul plates of the molds for experiments 2 and 4 were wired together and a lead wire from the experiment 4 caul plate was connected to the input signal. The direction of the electric field was through the plane of the composite specimens. An exploded view drawing of the DPA set-up is shown in Figure 23.

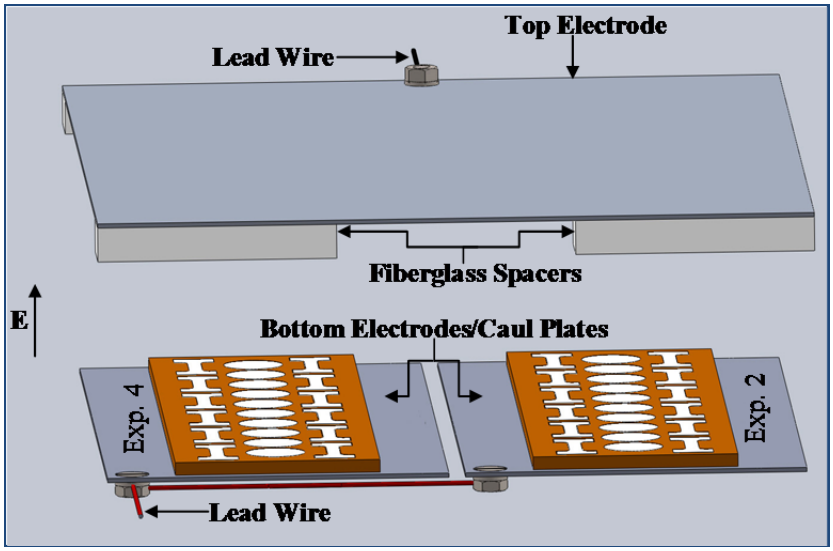


**Figure 23: Exploded View of the Through-Plane DPA Set-up for Experiments 2 and 4**

Using a WaveTek (Model 10 MHz DDS) function generator, a square wave with anamplitude of ± 5 V and a frequency of 650 Hz was sent to a TREK Model 20/20A amplifier. The amplifier increased the input signal to a maximum peak voltage of 10 kV. The distance between the electrodes was 48 mm, thus the maximum electric field applied during Through-Plane DPA was 0.79 MV/m. These experiments were also placed inside an electrical isolation box and the field was applied for 24 hours, as the composites cured at room temperature.

#### *3.3.3.2.1 MAX DPA Experiments*

For the MAX experiments, DPA was also applied Through-Plane. The bottom caul plate served as one electrode and another aluminum plate was placed above it, at a distance of 12.7 mm, and served as the top electrode. Once again, the distance between the electrodes was set by fiberglass spacers that were affixed to the top electrode. Just as in the Through-Plane DPA case detailed in Section 3.3.3.2, a lead wire from the top electrode was connected to ground, and a lead wire from the bottom caul plate was connected to the input signal. An exploded view drawing of the Through-Plane DPA set-up used to manufacture the MAX specimens is shown in Figure 24.

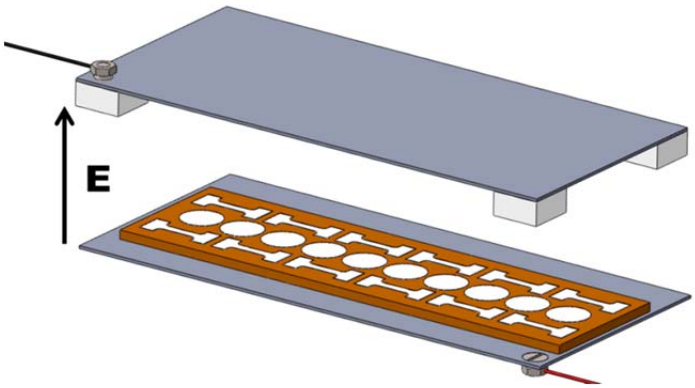


**Figure 24: Exploded View of Through-Plane DPA Set-up for MAX Experiment**

Using a function generator by WaveTek (Model 10 MHz DDS), a sinusoidal wave was used as the input signal voltage, at a frequency of 350 Hz. This signal was sent to a TREK Model 610E Cor-A-Trol H.V. Supply Amplfier/Controller. This amplifier had a maximum frequency limit of 350 Hz, before the voltage signal was cut off at the peaks. The voltage signal was recorded during the MAX experiment and it was used to plot the electric field with respect to time. This plot can be found in Figure 25 and it shows that the maximum field applied was ~ 0.5 MV/m.

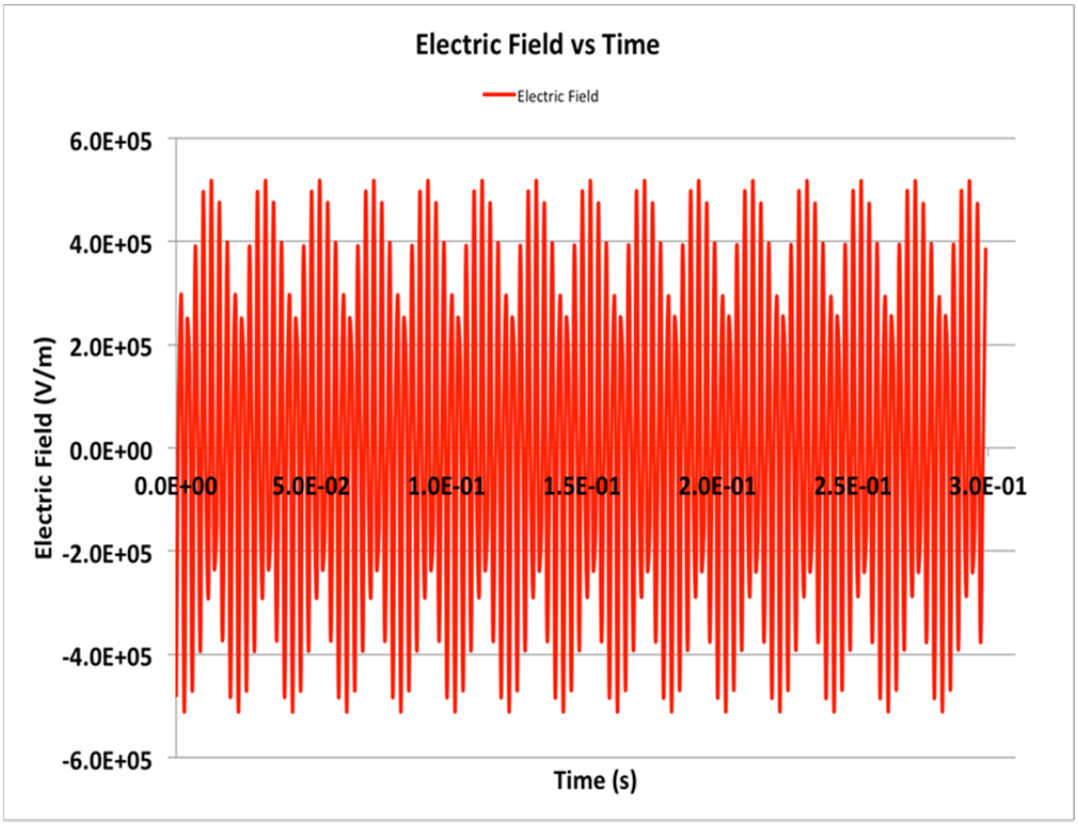


**Figure 25: Plot of Electric Field vs Time for MAX Through-Plane DPA Experiment**

# *Chapter 4: Material Characterization*

Both the mechanical and electrical properties of the composite specimens, as well as the pure and modified resin samples, were investigated. Nondestructive Evaluation (NDE) methods were used to characterize the elastic modulus, and tensile testing was done to characterize the strength of the material. Dielectric property testing was also conducted to characterize the dielectric constant and dielectric loss of the material.

## *4.1 Elastic Properties of Materials in Tension*

When a force pulls on an object, the object is said to be in tension. If a uniform, static force, *F*, pulls on an object and the force is applied over the surface, or cross-sectional area of an object, the length of the object changes from its original length $L_0$, to a new length *L, as* shown in Figure 26. This change in length or elongation, is known as $\Delta L$, and $\Delta L = L_0 - L$, *and* $\Delta L << L_0$.

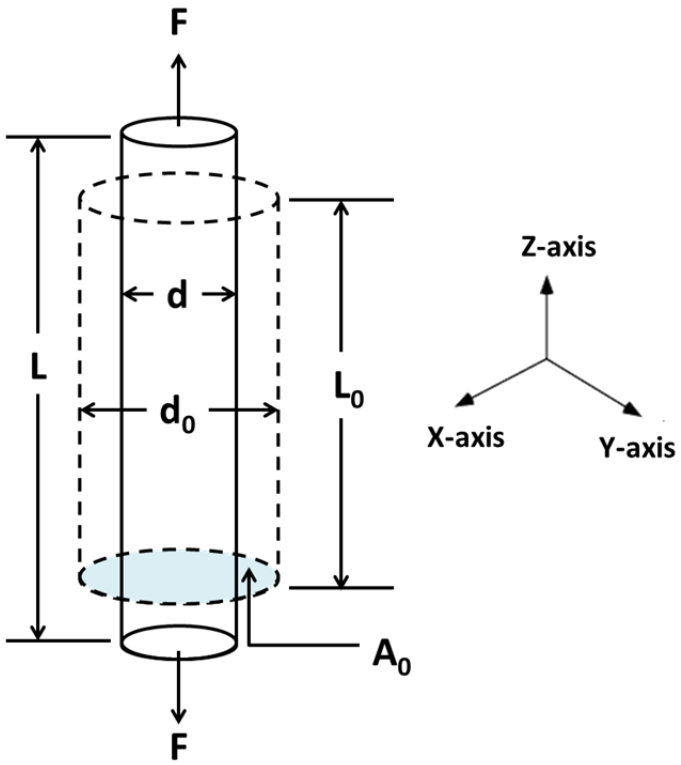


**Figure 26: Elongation of an Object Under a Linear Uniaxial Tensile Load[58]**

The ratio of the force to the original cross-sectional area is defined as the stress $\sigma$, and is given by Equation 4.1.1[1].

$$\sigma = \frac{F}{A_0} \qquad \textbf{Equation 4.1.1}$$

The original cross-sectional area of the object is $A_0$. The ratio of the object's elongation $\Delta L$, to its original length $L_0$, is defined as the strain $\varepsilon$, and is given by Equation 4.1.2[1].

$$\varepsilon = \frac{\Delta L}{L_0} \qquad \textbf{Equation 4.1.2}$$

Isotropic solids are characterized by two independent elastic constants, e.g., the Young's Modulus, $E$, and Poisson's ratio, $\nu$. These are one of the possible pairs, but the others are related to $E$ and $\nu$. Isotropic materials are those in which the material properties are independent of the direction of measurement[58]. In an isotropic solid, a uniaxial stress load produces one component of stress, $\sigma_z$, which results in strain along the z-axis, $\varepsilon_z$. The stress is given by Equation 4.1.3, also known as Hooke's law[83].

$$\sigma_z = E\varepsilon_z \qquad \textbf{Equation 4.1.3}$$

Note that when the object in Figure 26 elongates under uniaxial stress, it also contracts in the transverse direction, and its original diameter $d_0$ reduces to $d$. For an isotropic material, the lateral contractions in the $x$ and $y$-directions are perpendicular to the applied stress, which is in the $z$-direction. These contractions are compressive and have strains $\varepsilon_x$ and $\varepsilon_y$. Since the material is isotropic, $\varepsilon_x = \varepsilon_y$, and there is a parameter, known as Poisson's ratio, which defines the ratio of the lateral strain, $\varepsilon_x$, to the axial strain, $\varepsilon_z$. Poisson's ratio, $\nu$, is given by Equation 4.1.4[58].

$$\nu = -\frac{\varepsilon_x}{\varepsilon_z} \qquad \textbf{Equation 4.1.4}$$

## 4.2 Elastic Wave Propagation in Materials

For isotropic materials, there are two different elastic waves, dilatational and shear, which propagate through unbounded isotropic media[84]. The dilatational waves are longitudinal, with speed $c_1$, and are known as P waves, and the shear waves are transverse, with speed $c_2$, and are known as S waves. These wave speeds, $c_1$ and $c_2$, are given by Equations 4.2.1 and 4.2.2, respectively[85].

$$c_1 = \sqrt{\frac{E(1-\nu)}{\rho(1+\nu)(1-2\nu)}} \qquad \textbf{Equation 4.2.1}$$

$$c_2 = \sqrt{\frac{E}{2\rho(1+\nu)}} \qquad \textbf{Equation 4.2.2}$$

Dilatational waves arrive before shear waves, so $c_1 > c_2$.

From Equations 4.2.1 and 4.2.2, $\nu$ and $E$ can be found with Equations 4.2.3 and 4.2.4, respectively.

$$\nu = \frac{c_1^2 - c_2^2}{2(c_1^2 - 2c_2^2)} \qquad \textbf{Equation 4.2.3}$$

$$E = 2\rho c_2^2(1+\nu) \qquad \textbf{Equation 4.2.4}$$

Nondestructive evaluation (NDE) techniques for determining the elastic properties of composites, and for the detection of damage in composites, are based upon elastic wave propagation in materials.

## 4.3 Nondestructive Evaluation (NDE)

Several researchers have used NDE methods to characterize the mechanical constants of materials[86-99]. Mourik et al.[94] used NDE techniques to characterize the elastic anisotropy in Aluminum-SiC and -$Al_2O_3$ metal matrix composites. Wooh and Daniel[90] used NDE testing to characterize the elastic properties of a graphite/epoxy unidirectional composite, and compared the NDE results to those obtained by mechanical testing. Balasubramaniam and Whitney[92], as well as Adamowski et al.[93], used NDE techniques to characterize the elastic properties of fiber-reinforced composites, while Solodov et al.[99] conducted a case study on the elastic anisotropy in carbon fiber-reinforced composites, using NDE methods. Rokhlin and Wang[97] used NDE testing to characterize the elastic properties in multidirectional composites, and Hsu et al.[91] used NDE methods to determine the anisotropic elastic constants in thick composite laminates.

The ASTM D1708-06a standard, used in this research to characterize the strength of the material, does not allow the determination of the modulus of elasticity, *E*, as listed in Section 1.3 of the specification[83]. Since *E* could not be determined through tensile testing, NDE techniques were used. Ultrasonic waves were transmitted and received through the material using Digital Wave B1025 broadband lead zirconate titanate (PZT) transducers. The transducers were placed in the grip area of the microtensile test specimens. A single sine wave, with a frequency of 850 kHz, was generated by a Stanford Research Systems function generator. The signal was filtered and amplified with a Digital Wave Corp Model FM-1 signal conditioner. An Agilent Technologies 54624A four-channel digital oscilloscope, with a 100 MHz sampling rate, was used to digitize and record the ultrasonic signal.

Two sets of transducers produced elastic waves for the NDE characterization. One set produced and received P waves and the other set produced and received S waves. The P wave

oscillates in the direction of propagation of the wave, and the S wave motion is perpendicular to the direction of wave propagation. A schematic of the characterization set-up is shown in Figure 27 and a picture of the equipment is shown in Figure 28.

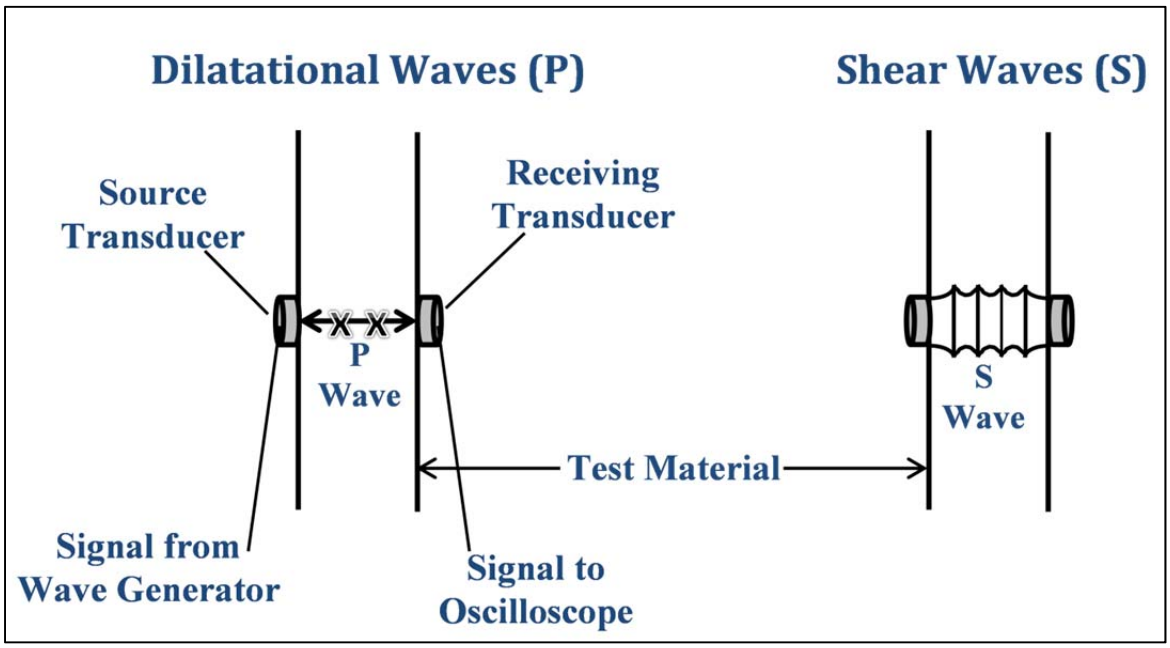


**Figure 27: Schematic of NDE Material Characterization Set-up**

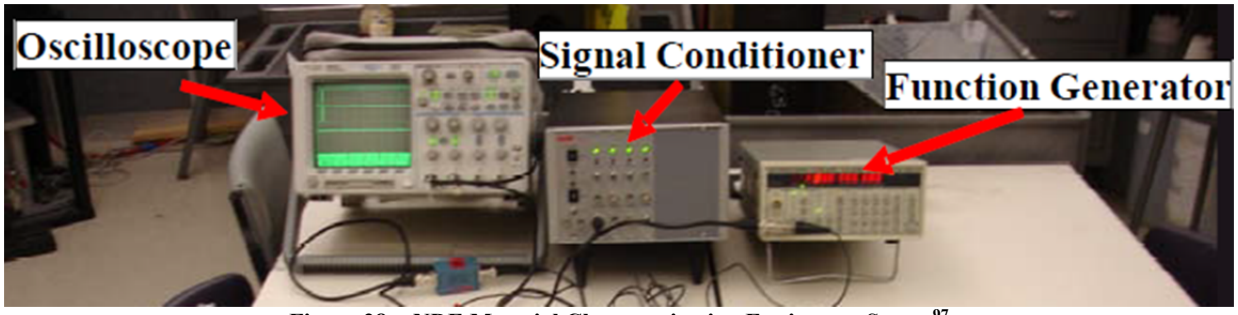


**Figure 28: NDE Material Characterization Equipment Set-up[97]**

Both P and S wave speeds were measured for each specimen, using the oscilloscope. Two readings were taken for each specimen, with one reading taken in each of the two grip areas of the microtensile test specimens, as shown in Figure 29. Prior to testing, the thickness of the specimens, in the test areas shown in Figure 29, was measured.

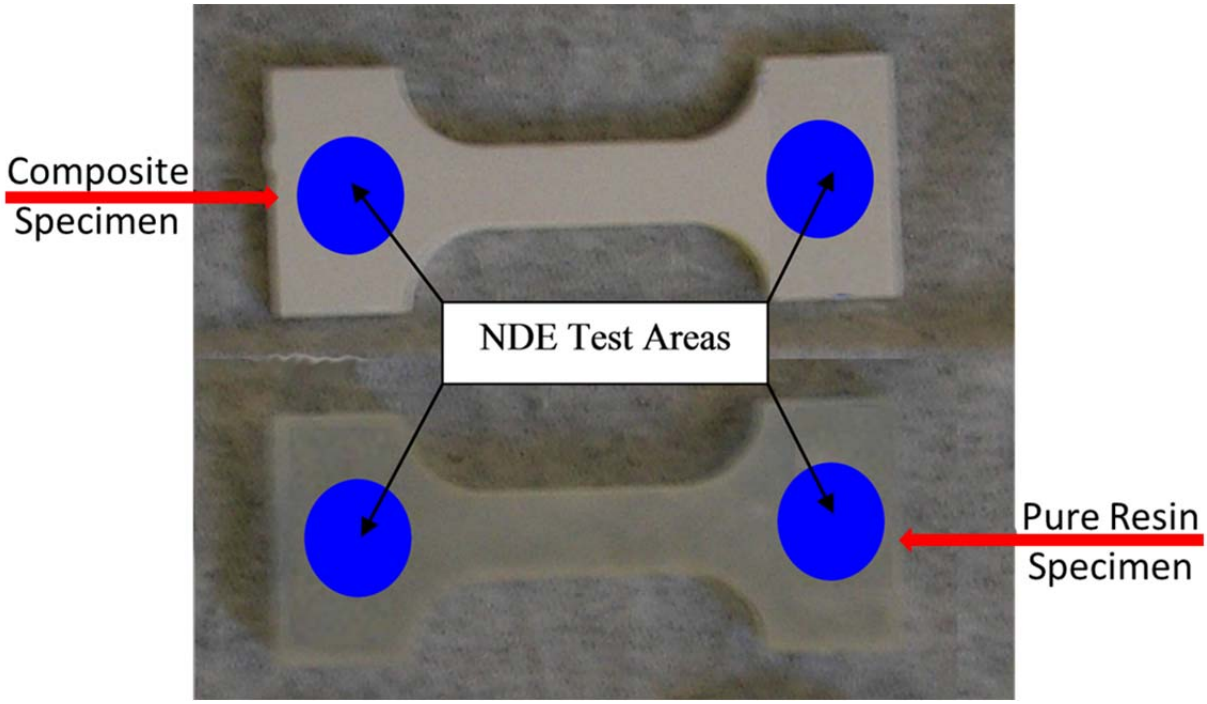


**Figure 29: Microtensile Specimens with NDE Test Areas Indicated in Blue**

The time delay between the transducers with no material between them, called the face-to-face speed, was measured for both sets of transducers. This value was later subtracted from the total time delay obtained when a sample was between the transducers.

After measuring both wave speeds $c_1$ and $c_2$, Equations 4.2.3 and 4.2.4 were used to determine $\nu$ and $E$, respectively. Plots of the waves generated and received when the transducers were face-to-face, as well as when they were in contact with the test specimens, are shown in Figures 30 and 31, for P and S wave signals, respectively.

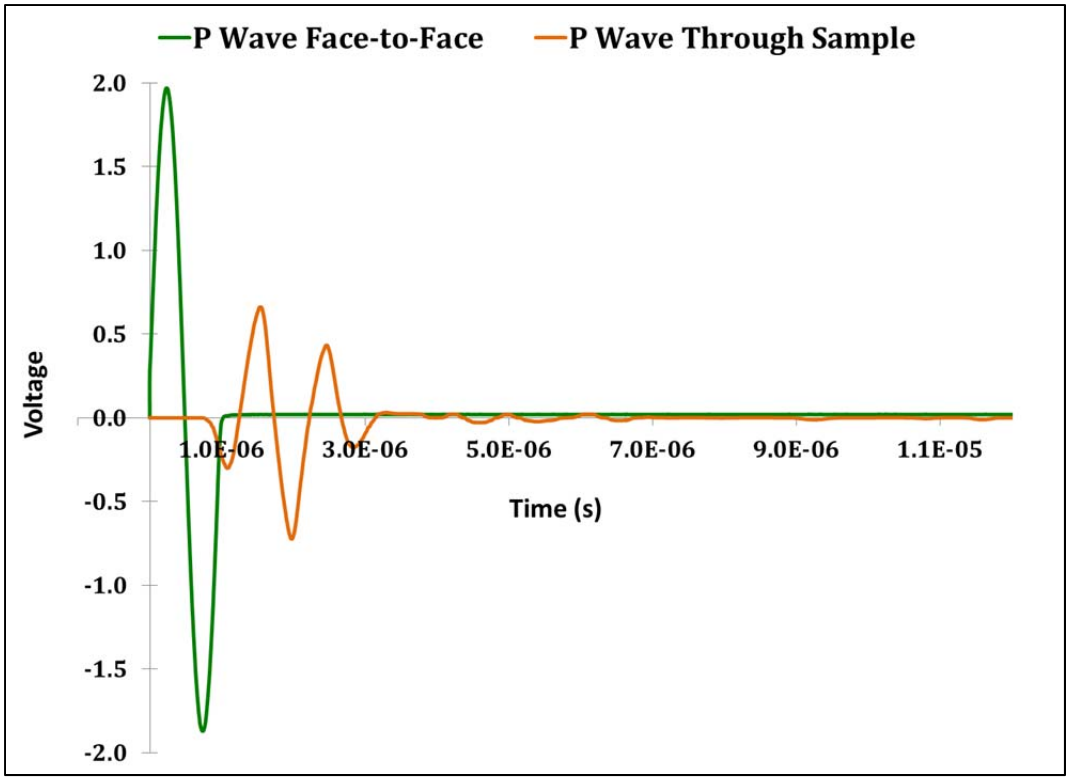


**Figure 30: P wave Plot with Face-to-Face Time Delay**

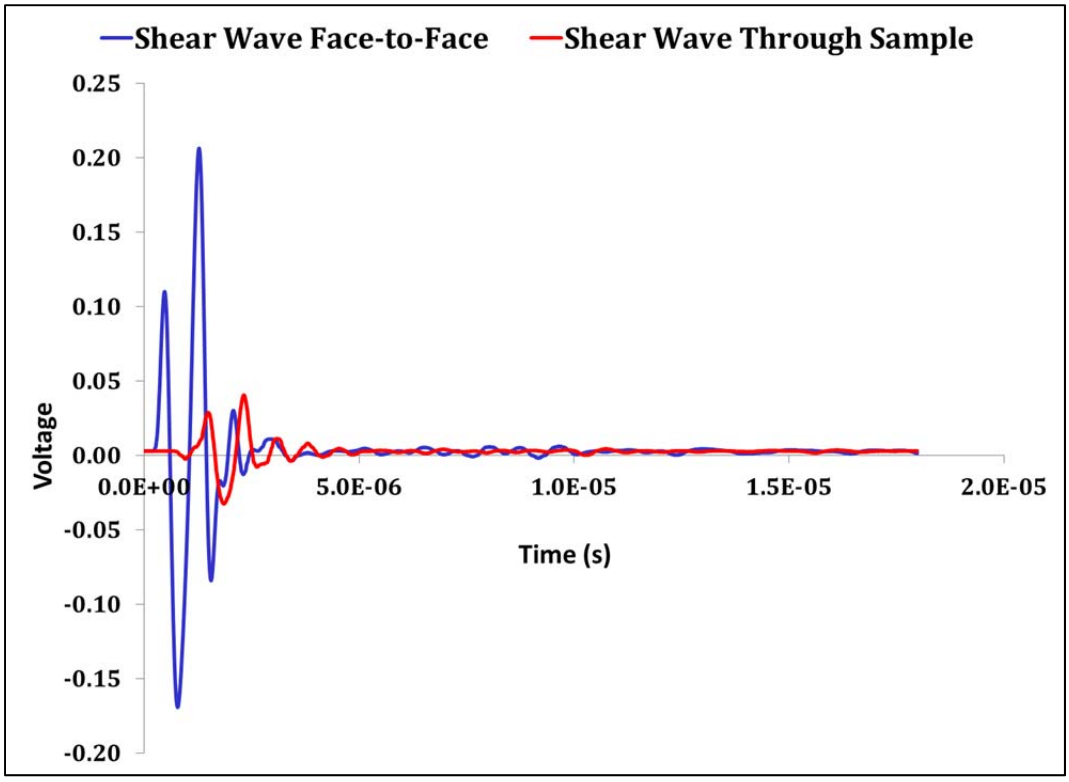


**Figure 31: P wave Plot with Face-to-Face Time Delay**

## 4.4 *Microtensile Testing*

The strength of the material was characterized in accordance with the ASTM D1708-06a Standard Test Method for Tensile Properties of Plastics by Use of Microtensile Specimens[84]. An Instron model 5544 System, with a 50 kN load cell, was used to test samples to failure. All of the samples failed in the neck region. Figure 32 illustrates the grip areas and neck region of the microtensile test specimens, and Figure 33 shows a picture of a composite specimen tested to failure.

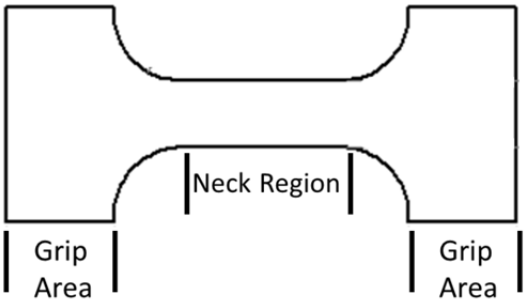


**Figure 32: Illustration of Microtensile Test Specimen Showing Grip Areas and Neck Region**

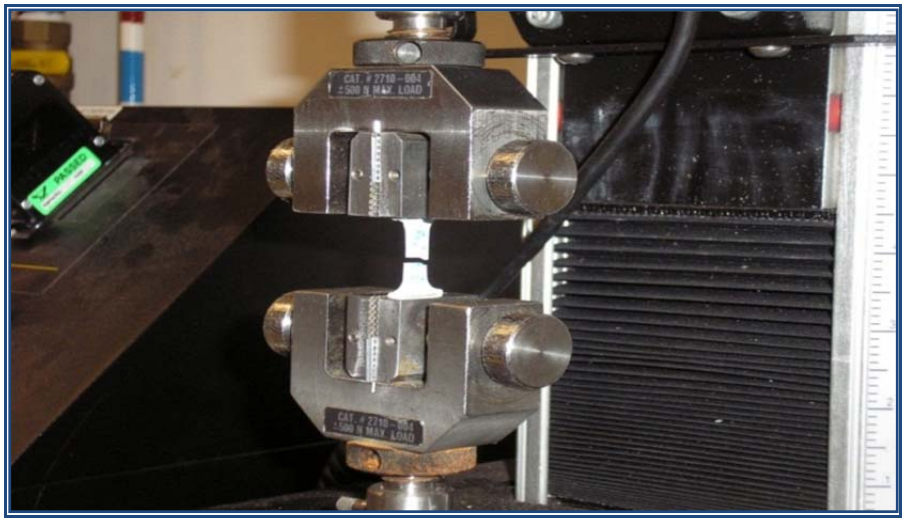

**Figure 33: Composite Microtensile Specimen Tested to Failure**

Prior to testing, the width and thickness (in the neck region) of each specimen was measured. These dimensions were used to calculate the original cross-sectional area, $A_0$, of each specimen.

The load at failure was obtained through testing, and the Failure Stress was calculated using Equation 4.1.1.

## 4.5 *Dielectric Property Testing*

Using an Agilent Technologies 4284A Impedence Analyzer and 16451B Solid Dielectric Test Fixture, shown in Figure 34, the dielectric constant, $\varepsilon_r$, and dielectric loss, *tan* $\delta$, of the material were characterized.


**Figure 34: Agilent Technologies 4284A Impedence Analyzer (a) and 16451B Solid Dielectric Test Fixture (b)**

The electrode used in the test fixture was Electrode D, for materials with applied thin film electrodes. The dimensions of Electrode D, the applied thin film electrodes and test material specifications are shown in Figure 35.

After measuring the thickness, *d*, of each test specimen, a thin layer of gold was sputtered onto them, using a Hummer Sputter Model 6.2. Masks made from aluminum were placed on top of the specimens prior to sputtering, to produce the pattern required for characterization with Electrode D. Figure 36 shows test specimens prior to sputtering, with the masks in place, as well as a test specimen with the electrode sputtered onto the surface.

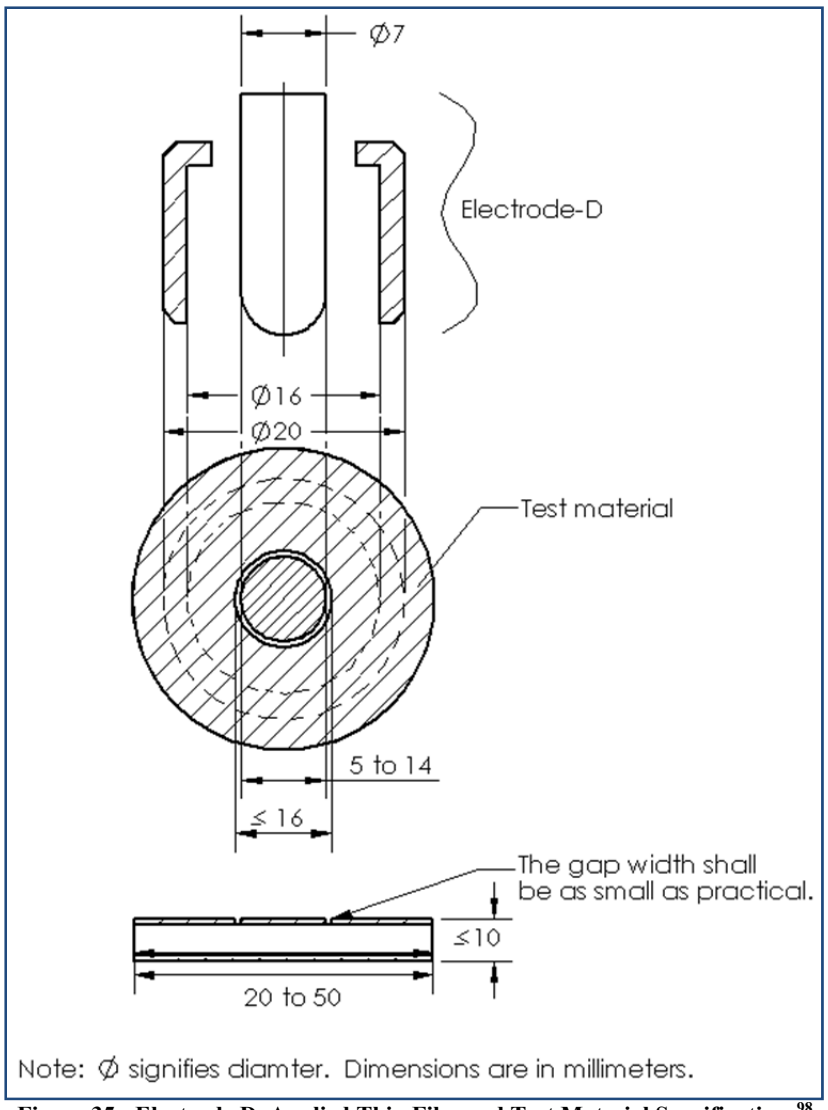


**Figure 35: Electrode D, Applied Thin Film and Test Material Specifications[98]**

After sputtering a thin layer of gold onto both sides of the test specimens, they were placed inside the Agilent Solid Dielectric Test Fixture and cycled through a frequency range from 100 Hz to 1 MHz, using LabVIEW. Capacitance, *C*, and $tan\ \delta$ were obtained at 100 points throughout the frequency range. Using the permittivity of free space $\varepsilon_0 = 8.854$ F/m, the thickness, *d*, of the specimens, along with Equations 1.25 and 1.26, $\varepsilon_r$ was determined.

**Figure 36: Specimens with Masks on Sputter Stage (left), Specimen with Sputtered Electrode (right)**

# *Chapter 5: Results and Analysis*

The material characterization results for the mechanical and dielectric properties were determined as detailed in Chapter 4, and the mean and standard deviation of the data were calculated. A signal-to-noise ratio analysis was performed on the In-Plane and Through-Plane parametric studies, to determine the optimum combination of parameters required to achieve the desired material characteristic. A rank analysis was also performed, to determine which parameter had the greatest influence, on the desired material property.

## *5.1 Signal-to-Noise Ratio Analysis*

When using the Taguchi Methods, the parameters chosen for testing represent the controllable factors in an experiment or manufacturing process. In this research, the parameters chosen were the volume fraction of particles, the use of DPA, and the crystal structure/size of the particles. In addition to the controllable factors, there are also uncontrollable factors involved in experiments, such as environmental factors, human error, etc. Both the controllable and the uncontrollable factors have an effect on the outcome. Professor Taguchi defines the controllable factors as the signal, and the uncontrollable factors as the noise. The Taguchi Methods focus on maximizing the effects of the controllable factors or the signal, while minimizing the effects of the uncontrollable factors, or the noise. When a series of samples are measured and the standard deviation of those measurements is large, it is difficult to trust the mean value obtained. The signal-to-noise ratio is a means to sort this out, as the variation is used to analyze these effects through the calculation of signal-to-noise ratios (*SN*).

The *SN* equations are derived from the quadratic loss function, and there are three cases for which these values are calculated. One case is when the maximum value of a characteristic is desired, another case is when the minimum value of a characteristic is desired, and the final case

is when a specific target value of a characteristic is desired. The two cases used in this research were the larger-is-best, for Young's modulus, failure stress, and dielectric constant; and the smaller-is-best, for dielectric loss.

In cases where the larger outcome is best, the signal-to-noise ratio, denoted as $SN_L$, is given by Equation 5.1.1, and in the case where the smaller outcome is best, the signal-to-noise ratio, denoted as $SN_S$, is given by Equation 5.1.2[99].

$$SN_L = -10\log\left(\frac{1}{n}\right)\sum_{i=1}^{n}\frac{1}{y_i^2} \qquad \textbf{Equation 5.1.1}$$

$$SN_S = -10\log\left(\frac{1}{n}\right)\sum_{i=1}^{n} y_i^2 \qquad \textbf{Equation 5.1.2}$$

In both Equations 5.1.1 and 5.1.2, $n$ is the number of observations and $y$ is the particular characteristic being measured. In all cases, whether larger-is-best or smaller-is-best, the goal is to maximize the $SN$[101]. For each of the parametric studies conducted, the $SN$ analysis was completed, and the results were compared. Note that a $SN$ analysis for Experiment MAX was not performed, as MAX is not part of the Taguchi test matrix.

### *5.1.1 Rank Analysis (Δ)*

After calculating the $SN$ ratio for each experiment, the mean $SN$ ratio ($\overline{SN}$) can be found for each parameter and level, and the effect of each parameter can be separated because the experimental design is orthogonal[100]. The effect of a parameter (Δ) is then defined as the absolute value of the difference between the mean $SN$ ratios of the levels. In the case of an $L_4$ ($2^3$) orthogonal array used in this research, where there are two levels for each parameter, the effect of a parameter is defined as the absolute difference between the average $SN$ ratio of levels 1 and 2, as shown in Equation 5.1.1.1.

$$\Delta = \left| \overline{SN}_1 - \overline{SN}_2 \right| \qquad \text{Equation 5.1.1.1}$$

The parameter with the largest Δ has the most significant influence on the characteristic being measured. The parameters are then ranked in order of their significance on the characteristic, from 1 to p, where p is the number of parameters in the experiments. In this research there were three parameters being investigated, so Δ is ranked from 1 to 3 with 1 being the most significant controllable factor and 3 being the least significant controllable factor. Note that as in the case of the *SN* analysis, rank analysis was not conducted for Experiment MAX.

## *5.2 Elastic Modulus Results*

The mean Young's modulus, *E*, and standard deviation for the composite specimens, pure resin and pure resin specimens containing 5% by weight HELOXY™ 61 Epoxy Functional Modifier (hereafter referred to as 5% Modified Resin) can be found in Table 9 and a plot of the results is shown in Figure 37.

**Table 9: Mean and Standard Deviation of Young's Modulus Resulting from NDE**

| *Test Specimens* | *Mean E (GPa)* | *Standard Deviation (GPa)* |
|---|---|---|
| Pure Resin | 4.24 | 0.21 |
| 5% Modified Resin | 4.38 | 0.10 |
| Experiment 1 | 5.82 | 0.70 |
| Experiment 2 In-Plane DPA | 9.20 | 0.94 |
| Experiment 2 Through-Plane DPA | 7.79 | 0.58 |
| Experiment 3 | 14.48 | 1.04 |
| Experiment 4 In-Plane DPA | 13.51 | 0.37 |
| Experiment 4 Through-Plane DPA | 12.19 | 0.54 |
| MAX | 12.24 | 0.86 |

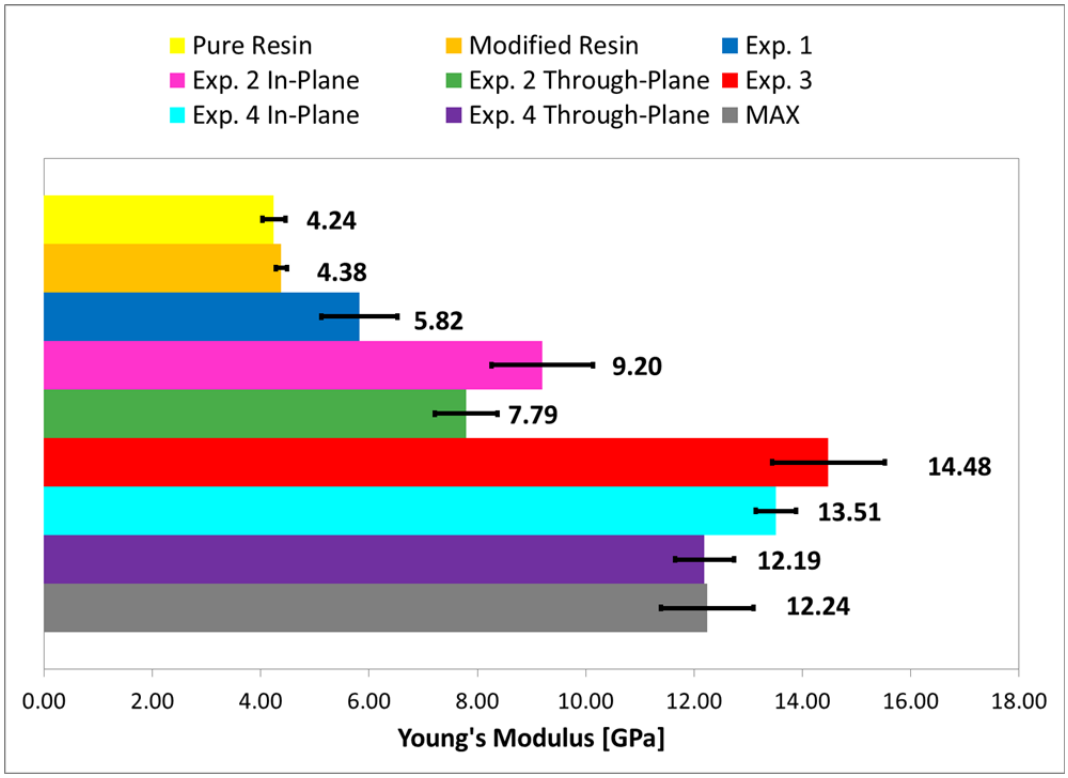


**Figure 37: Plot of Young's Modulus , *E*, Results**

### *5.2.1 Signal-to-Noise ($SN_L$) Ratio and Rank ($\Delta$) Analysis for E*

For *E*, $SN_L$ was used, as an objective of this research was to increase the stiffness of the polymer, by adding ceramic particles. The results for the In-Plane and Through-Plane DPA studies can be found in Table 10 and Table 11, respectively. In each table, the maximum value for $SN_L$ is highlighted in yellow, with its corresponding controllable factors and experiment number. This represents the experiment with the optimum combination of parameters to maximize *E*.

**Table 10: $SN_L$ Analysis for $E$ from the In-Plane DPA Study**

| *In-Plane (IP) DPA Study* | | | | |
|---|---|---|---|---|
| **Young's Modulus, *E*** | | | | |
| **Experiment Number** | **Particle Volume Fraction ($V_f$)** | **Dielectrophoretic Assembly (DPA)** | **Particle Size (Crystal Structure)** | **$SN_L$ values for *E*** |
| **1** | 25% | No | 100 (cubic) | 15.14 |
| **2-IP** | 25% | Yes | 200 (tetragonal) | 19.10 |
| **3** | 50% | No | 200 (tetragonal) | 23.14 |
| **4-IP** | 50% | Yes | 100 (cubic) | 22.60 |

**Table 11: $SN_L$ Analysis for $E$ from the Through-Plane DPA Study**

| *Through-Plane (TP) DPA Study* | | | | |
|---|---|---|---|---|
| **Young's Modulus, *E*** | | | | |
| **Experiment Number** | **Particle Volume Fraction ($V_f$)** | **Dielectrophoretic Assembly (DPA)** | **Particle Size (Crystal Structure)** | **$SN_L$ values for *E*** |
| **1** | 25% | No | 100 (cubic) | 15.14 |
| **2-TP** | 25% | Yes | 200 (tetragonal) | 17.76 |
| **3** | 50% | No | 200 (tetragonal) | 23.14 |
| **4-TP** | 50% | Yes | 100 (cubic) | 21.70 |

The rank analysis was completed for both the In-Plane DPA and Through-Plane studies, and the results are listed in Table 12 and Table 13, respectively. In each table, the parameter with the rank of 1 is highlighted in blue, along with its controllable factor. This represents the parameter with the largest impact on *E*.

**Table 12: Rank Analysis for $E$ from the In-Plane DPA Study**

| *In-Plane (IP) DPA Study* | | | |
|---|---|---|---|
| **Young's Modulus, *E*** | | | |
| **Mean $SN_L$ at Levels 1 and 2** | **Particle Volume Fraction ($V_f$)** | **Dielectrophoretic Assembly (DPA)** | **Particle Size (Crystal Structure)** |
| $\overline{SN}_1$ | 17.12 | 19.14 | 18.87 |
| $\overline{SN}_2$ | 22.87 | 20.85 | 21.12 |
| $\Delta$ | 5.75 | 1.71 | 2.25 |
| Rank | 1 | 3 | 2 |

**Table 13: Rank Analysis for *E* from the Through-Plane Study**

| ***Through-Plane (TP) DPA Study*** | | | |
|---|---|---|---|
| **Young's Modulus, *E*** | | | |
| **Mean $SN_L$ at Levels 1 and 2** | **Particle Volume Fraction ($V_f$)** | **Dielectrophoretic Assembly (DPA)** | **Particle Size(Crystal Structure)** |
| $\overline{SN}_1$ | 14.14 | 19.14 | 18.42 |
| $\overline{SN}_2$ | 22.42 | 19.73 | 20.45 |
| Δ | 8.28 | 0.58 | 2.03 |
| Rank | 1 | 3 | 2 |

The $SN_L$ analyses from both the In-Plane and Through-Plane DPA studies showed that the optimum combination of parameters to maximize *E* were found with Experiment 3, made with 200 nm (tetragonal) particles, at a volume fraction of 50%, and without the application of DPA. At 14.48 GPa, *E* for this composite was 3.4 times greater than pure resin. The rank analyses for both studies also found particle volume fraction to be the controllable factor with the greatest impact on *E*.

As detailed in Chapter 3, composites are designed to display a combination of the best characteristics of each of the component materials, through the principle of combined action. The increased stiffness achieved with the composites in this research is due to addition of the higher stiffness $BaTiO_3$ filler. As the volume of filler increased, there was also an increase in *E*. Research has shown that *E* can be improved by adding inorganic nanoparticles or microparticles to a polymer matrix, because the particles have a much greater stiffness than the polymer[101-107]. This is supported by the rank analysis for both studies in this research, which identified particle volume fraction as the most important parameter for increasing *E,* as shown in Tables 12 and 13.

## 5.3 *Failure Stress (FS) Results*

The mean Failure Stress, *FS*, and standard deviation for the composite specimens, pure resin, and 5% Modified Resin specimens, can be found in Table 14 and a plot of the results is shown in Figure 38.

**Table 14: Mean and Standard Deviation of Failure Stress Resulting from NDE**

| *Test Specimens* | *Mean FS (MPa)* | *Standard Deviation (MPa)* |
|---|---|---|
| Pure Resin | 69.00 | 1.05 |
| 5% Modified Resin | 59.34 | 8.94 |
| Experiment 1 | 61.23 | 6.48 |
| Experiment 2 In-Plane DPA | 49.80 | 8.16 |
| Experiment 2 Through-Plane DPA | 30.07 | 10.52 |
| Experiment 3 | 32.92 | 8.66 |
| Experiment 4 In-Plane DPA | 51.87 | 6.62 |
| Experiment 4 Through-Plane DPA | 16.22 | 6.12 |
| MAX | 21.60 | 4.59 |

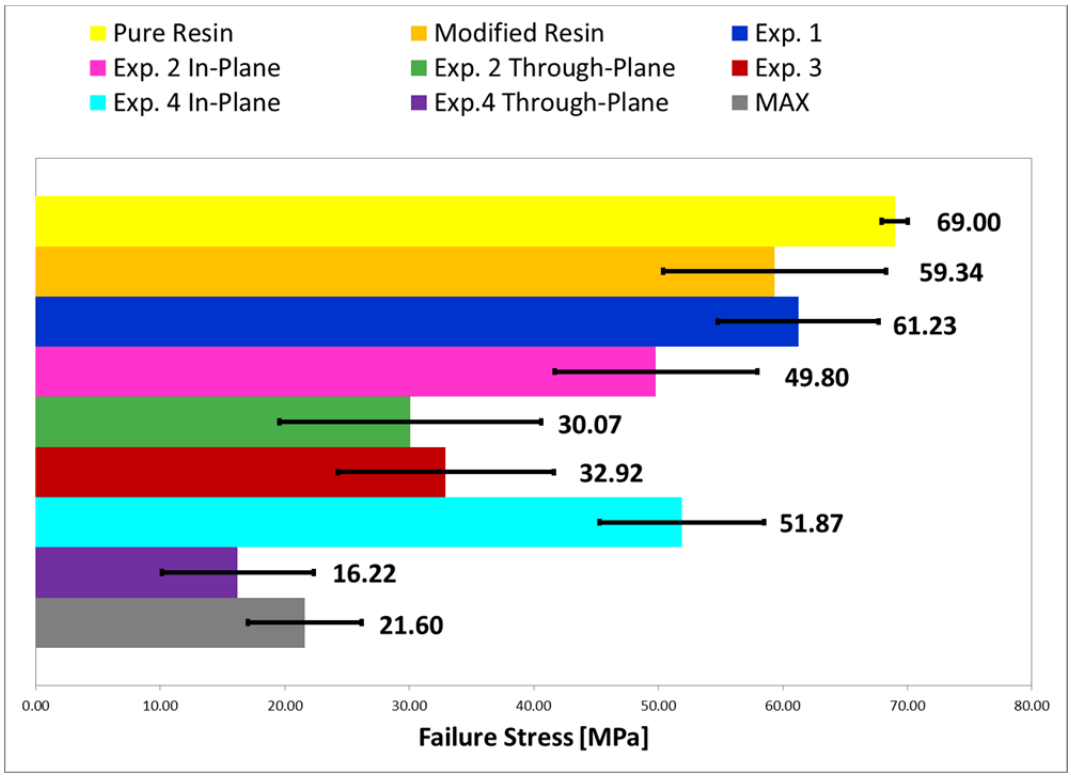


**Figure 38: Plot of Failure Stress, *FS*, Results**

### *5.3.1 Signal-to-Noise ($SN_L$) Ratio and Rank (Δ) Analysis for FS*

For *FS*, $SN_L$ was used, as an objective of this research was to increase the strength of the polymer by reinforcing it with ceramic particles. The results for the In-Plane and Through-Plane DPA studies can be found in Table 15 and Table 16, respectively. In each table, the maximum value for $SN_L$ is highlighted in yellow, with its corresponding controllable factors and experiment number. This represents the experiment with the optimum combination of parameters to maximize *FS*.

**Table 15: $SN_L$ Analysis for *FS* from the In-Plane DPA Study**

| ***In-Plane (IP) DPA Study*** | | | | |
|---|---|---|---|---|
| **Failure Stress, *FS*** | | | | |
| **Experiment Number** | **Particle Volume Fraction ($V_f$)** | **Dielectrophoretic Assembly (DPA)** | **Particle Size(Crystal Structure)** | **$SN_L$ values for *FS*** |
| **1** | 25% | No | 100 (cubic) | 35.59 |
| **2-IP** | 25% | Yes | 200 (tetragonal) | 33.54 |
| **3** | 50% | No | 200 (tetragonal) | 28.72 |
| **4-IP** | 50% | Yes | 100 (cubic) | 34.09 |

**Table 16: $SN_L$ Analysis for *FS* from the Through-Plane DPA Study**

| ***Through-Plane (TP) DPA Study*** | | | | |
|---|---|---|---|---|
| **Failure Stress, *FS*** | | | | |
| **Experiment Number** | **Particle Volume Fraction ($V_f$)** | **Dielectrophoretic Assembly (DPA)** | **Particle Size(Crystal Structure)** | **$SN_L$ values for *FS*** |
| **1** | 25% | No | 100 (cubic) | 35.59 |
| **2-TP** | 25% | Yes | 200 (tetragonal) | 28.31 |
| **3** | 50% | No | 200 (tetragonal) | 28.72 |
| **4-TP** | 50% | Yes | 100 (cubic) | 22.24 |

The $SN_L$ analyses from both the In-Plane and Through-Plane DPA studies, showed the optimum combination of parameters to maximize *FS*, were found with Experiment 1. These composites were made with 100 nm (cubic) particles, at a volume fraction of 25%, and

without the application of DPA. While there was no increase in strength of the Experiment 1 specimens, the *FS* of 61.23 MPa represents a less than 2% decrease in strength, as compared to pure resin. It is unclear if this decrease in strength can be attributed to the addition of particles. As listed in Table 14 and shown in Figure 38, a 16% decrease in strength resulted from the addition the HELOXY™ 61 Epoxy Functional Modifier. This modifier was added at 5%, by weight, of the resin. The mean *FS* and standard deviation for the Experiment 1specimens, also fall within the error range of the 5% Modified Resin specimens, so it is unclear if the particles are responsible for the slight decrease in strength.

The viscosity modifier used in this research is a reactive diluent, and although they reduce the viscosity of epoxy composites with high filler loadings, they are also associated with a reduction in mechanical strength and glass transition temperature[108] . The manufacturer recommends its use be limited to 20%, by weight, of the resin[73]. Although 5% by weight was used in this research, a reduction in strength was observed.

The composites made with 100 nm (cubic) particles, demonstrated higher mechanical strength, at equivalent particle loadings, than the composites made with 200 nm (tetragonal) particles. Smaller particles have a higher surface area than larger particles, and as shown in Table 2, the specific surface area of the 100 nm (cubic) particles is twice that of the 200 nm (tetragonal) particles. This increased surface area is believed to result in higher strength, as it provides more efficient stress transfer in the composite. Similar results have been found by others researchers, who investigated the size effect on the strength of particulate-filled composites[109-113]. While the effect of particle size on the *FS* of the composite materials has been observed, that was not the intent of this study. The purpose of this research was to find the

optimum combination of controllable factors, resulting in the desired material properties. In the case of *FS*, that was found to be the parameters used in Experiment 1.

The rank analysis was completed for both the In-Plane and Through-Plane DPA studies, and the results are listed in Table 17 and Table 18, respectively. In each table, the parameter with the rank of 1 is highlighted in blue, along with its controllable factor. This represents the parameter with the largest impact on *FS*.

**Table 17: Rank Analysis for *FS* from the In-Plane DPA Study**

| ***In-Plane (IP) DPA Study*** | | | |
|---|---|---|---|
| **Failure Stress, *FS*** | | | |
| **Mean $SN_L$ at Levels 1 and 2** | **Particle Volume Fraction ($V_f$)** | **Dielectrophoretic Assembly (DPA)** | **Particle Size (Crystal Structure)** |
| $\overline{SN}_1$ | 34.56 | 32.15 | 34.84 |
| $\overline{SN}_2$ | 31.40 | 33.81 | 31.13 |
| Δ | 3.16 | 1.66 | 3.71 |
| Rank | 2 | 3 | 1 |

**Table 18: Rank Analysis for *FS* from the Through-Plane Study**

| ***Through-Plane (TP) DPA Study*** | | | |
|---|---|---|---|
| **Failure Stress, *FS*** | | | |
| **Mean $SN_L$ at Levels 1 and 2** | **Particle Volume Fraction ($V_f$)** | **Dielectrophoretic Assembly (DPA)** | **Particle Size(Crystal Structure)** |
| $\overline{SN}_1$ | 31.95 | 32.15 | 28.92 |
| $\overline{SN}_2$ | 25.48 | 25.28 | 28.52 |
| Δ | 6.47 | 6.87 | 0.40 |
| Rank | 2 | 1 | 3 |

For the In-Plane study, the rank analysis shows the particle size/crystal structure has the largest impact on *FS*. This supports the conclusion that the strength is increased with smaller particle size and greater surface area. For the Through-Plane study, however, the parameter with the largest impact on *FS* was DPA. During tensile testing, force was applied in the direction

perpendicular to the particle alignment, thus resulting in transverse loading. This is known as the iso-stress state, and the total stress, σ, in the material is given by Equation 5.3.1.1[58].

$$\sigma_f = \sigma_c = \sigma_m = \sigma$$ **Equation 5.3.1.1**

The subscripts *f*, *c*, and *m* refer to the filler, composite, and matrix, respectively. Since the polymer matrix and particle filler are experiencing the same load, the strength of the composite is determined by the weaker matrix. Scanning electron microscopy (SEM) was used to investigate particle chaining in DPA specimens; however, the high particle content made it challenging to discern distinct particle alignment. See Figure 39.

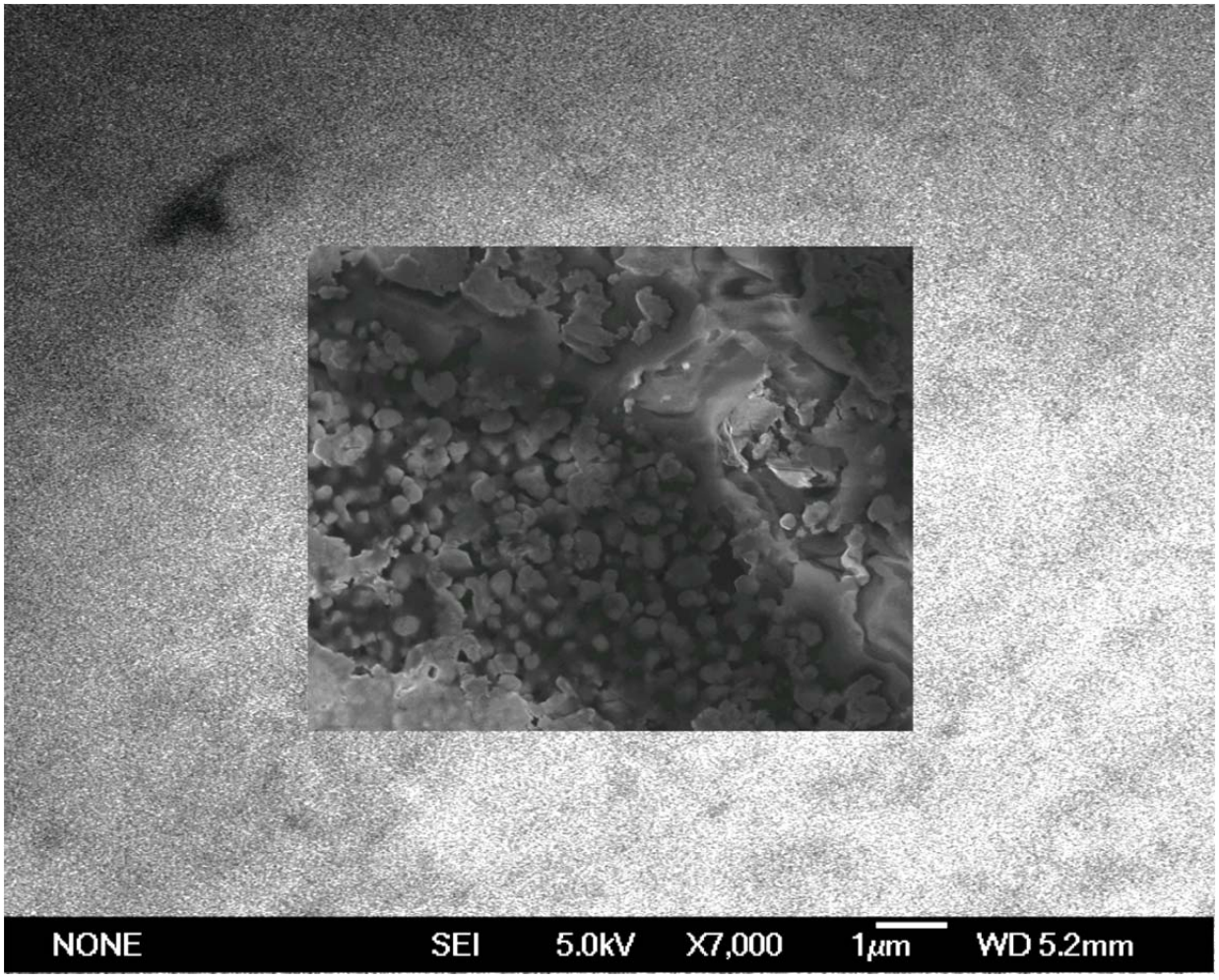


**Figure 39: SEM Image of 25% Volume Fraction Particles with DPA**

Figure 39 shows a pattern of alignment, in a 25% volume fraction composite with 200 nm (tetragonal) particles. Particle agglomeration was also observed. Due to the high particle loading used in this research, particle agglomeration was a problem that contributed to lower strength, despite the use of a coupling agent and a viscosity modifier.

## 5.4 Dielectric Property Results $\varepsilon_r$ and tan$\delta$

The mean and standard deviation for $\varepsilon_r$ @ 203 Hz and tan $\delta$ @ 1 MHz, are listed in Table 19. The mean $\varepsilon_r$ values were taken at a frequency of 203 Hz, as this was the frequency at which $\varepsilon_r$ was highest for all specimens characterized. The mean tan $\delta$ values were taken at a frequency of 1 MHz, as this was the maximum frequency used for characterizing these materials, and the highest values for tan $\delta$ are typically found at higher frequencies.

**Table 19: Mean and Standard Deviation of Dielectric Constant, $\varepsilon_r$, @ 203 Hz and tan d @ 1MHz**

| *Test Specimens* | *Mean $\varepsilon_r$* | *Standard Deviation* | *Mean tan $\delta$* | *Standard Deviation* |
|---|---|---|---|---|
| Pure Resin | 4.77 | 0.21 | 0.0273 | 0.0006 |
| 5% Modified Resin | 5.78 | 0.97 | 0.0231 | 0.0017 |
| Experiment 1 | 10.17 | 0.69 | 0.0228 | 0.0013 |
| Experiment 2 In-Plane DPA | 19.71 | 5.94 | 0.0227 | 0.0009 |
| Experiment 2 Through-Plane DPA | 30.27 | 10.39 | 0.0354 | 0.0252 |
| Experiment 3 | 42.66 | 2.14 | 0.0230 | 0.0018 |
| Experiment 4 In-Plane DPA | 19.76 | 0.74 | 0.0224 | 0.0014 |
| Experiment 4 Through-Plane DPA | 25.80 | 0.81 | 0.0257 | 0.0012 |
| MAX | 60.01 | 2.26 | 0.0217 | 0.0005 |

The maximum $\varepsilon_r$ was obtained from Experiment MAX, which was made with 50% volume fraction of 200 nm (tetragonal) particles, and DPA was applied. At 60.01, $\varepsilon_r$ for the max specimens was more than 12 times greater than pure resin, at 4.77. Given the same volume fraction of particles, the dielectric constant for specimens containing the 200 nm (tetragonal) particles, was higher than those containing the 100 nm (cubic) particles. At a particle loading of

25% by volume, Experiment 1 specimens, with 100 nm (cubic) particles have a lower dielectric constant that Experiments 2 (In-Plane and Through Plane) with 200 nm (tetragonal) particles. Similarly, at a particle loading of 50% by volume, Experiments 3 and MAX, with 200 nm (tetragonal) particles, have a higher dielectric constant than Experiments 4 (In-Plane and Through-Plane) with 100 nm (cubic) particles. This is believed to be due to the crystal structure, and corresponding polarization, of the particles.

There are three major types of polarization; electronic, ionic and orientation[58]. All three are depicted in Figure 40. Electronic polarization is defined as displacement of the center of the negatively charged electron cloud, relative to the positive nucleus of an atom, due to the presence of an electric field. Ionic polarization is defined as the displacement of cations in one direction, accompanied by the displacement of anions in the opposite direction, in the presence of an electric field. The third type of polarization applies only to materials with permanent dipole moments and results from the rotation of the permanent moments into the direction of the applied field.

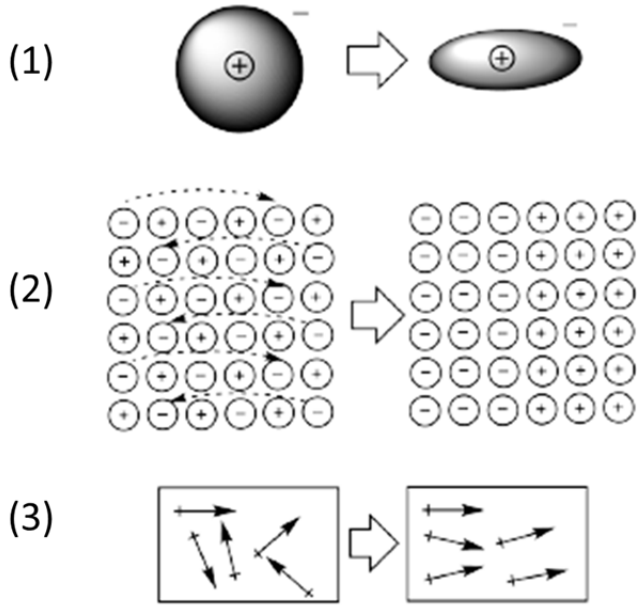


**Figure 40: Types of Polarization (1) Electronic (2) Ionic (3) Orientation**

As detailed in Section 2.1, tetragonal phase, $BaTiO_3$ has a permanent dipole, due to a shift in the central titanium atom of the molecule. These tetragonal particles have all three polarization components, ($P = P_e + P_i + P_o$); however, the cubic particles only have two of them ($P = P_e + P_i$). As shown in Equation 1.3.7, polarization, $P$, is related to electric field, $E$, through the dielectric constant, $\varepsilon_r$, of the material. Rearranging Equation 1.3.7 in terms of $\varepsilon_r$, yields Equation 5.4.1.

$$\varepsilon_r = 1 + \frac{P}{\varepsilon_0 E} \qquad \textbf{Equation 5.4.1}$$

Equation 5.4.1 shows that an increase in $P$ leads to an increase in $\varepsilon_r$. If the volume fractions are equal, composites made with tetragonal particles should have a higher $\varepsilon_r$ than those made with cubic particles.

Also of note is the fact that $\varepsilon_r$ for Experiment 2 In-Plane specimens, with a particle loading of 25% tetragonal particles, is nearly equal to the $\varepsilon_r$ for Experiment 4 In-Plane specimens, with a particle loading of 50% cubic particles, at all frequencies in the testing range. The remnant polarization of the tetragonal particles explains this as well. Even with half the amount of particles, the tetragonal $BaTiO_3$ was able to produce the same increase in $\varepsilon_r$.

The dielectric loss, tan $\delta$, for pure resin was 0.027 and the values for all of the composites ranged from 0.022 – 0.026, except for Experiment 2 Through-Plane specimens, which had a mean value of 0.035. It should be noted that arcing occurred between the bottom caul plate and top electrode of Experiment 2 Through-Plane, during DPA. The electric field was applied to both Experiments 2 and 4 Through-Plane, at the same time, as shown in Figure 23; however, arcing only occurred within the Experiment 2 mold. Each time the mold started to arc, the voltage was turned off and the top electrode was removed. There were visible signs of burning

on the top electrode, which covered the Experiment 2 mold, but no signs of burning on the side covering the Experiment 4 mold. This occurred four times during the 24-hour period of curing. The Experiment 2 Through-Plane specimens were also slightly discolored.

In addition to having a higher tan $\delta$, the standard deviation for the $\varepsilon_r$ was also very large for the Experiment 2 Through-Plane specimens. Arcing during DPA is believed to have contributed to the irregularities in the dielectric properties of the Experiment 2 Through-Plane specimens, although exactly how it affected the properties remains unclear. Plots of the results for $\varepsilon_r$, and $\tan\delta$, results are shown in Figures 41 and 42, respectively.

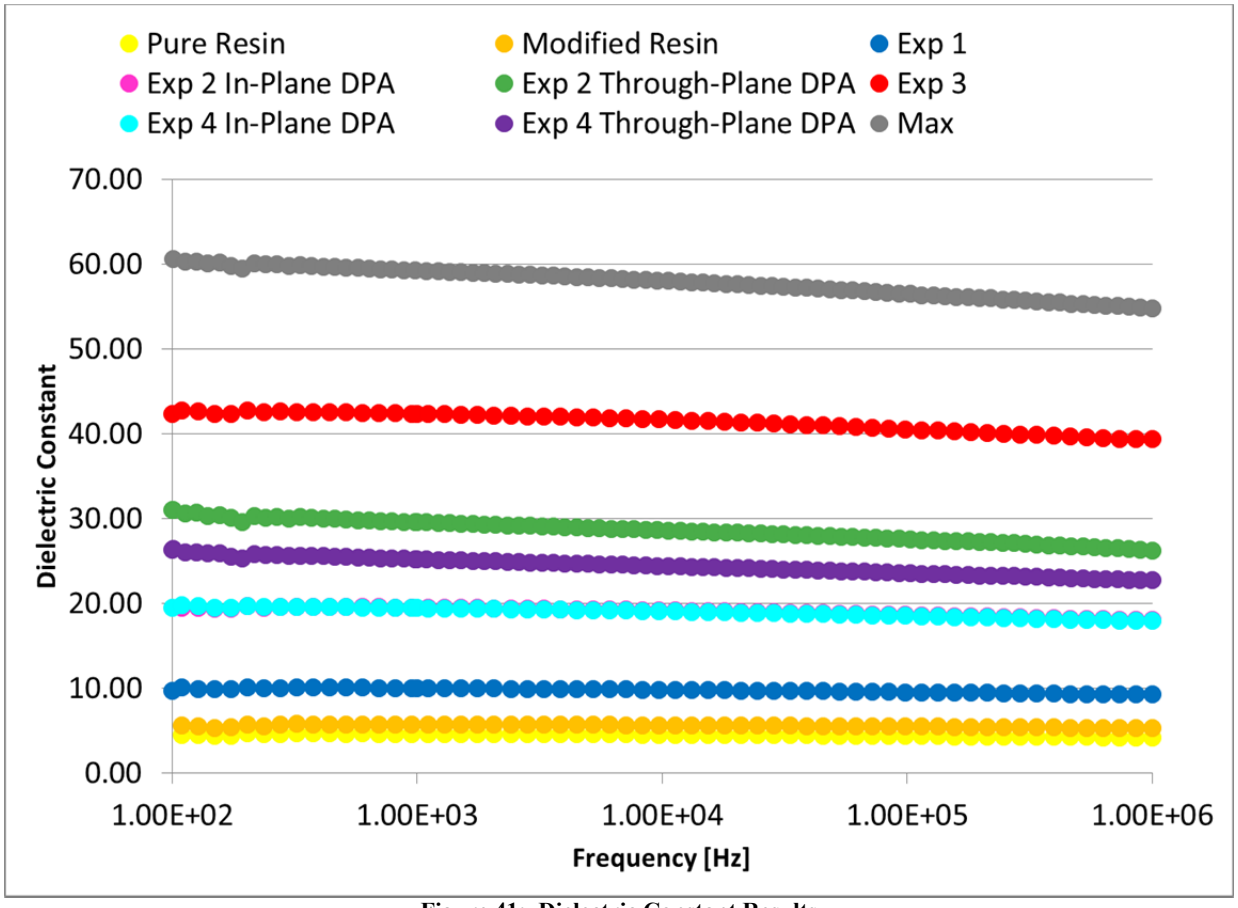


**Figure 41: Dielectric Constant Results**

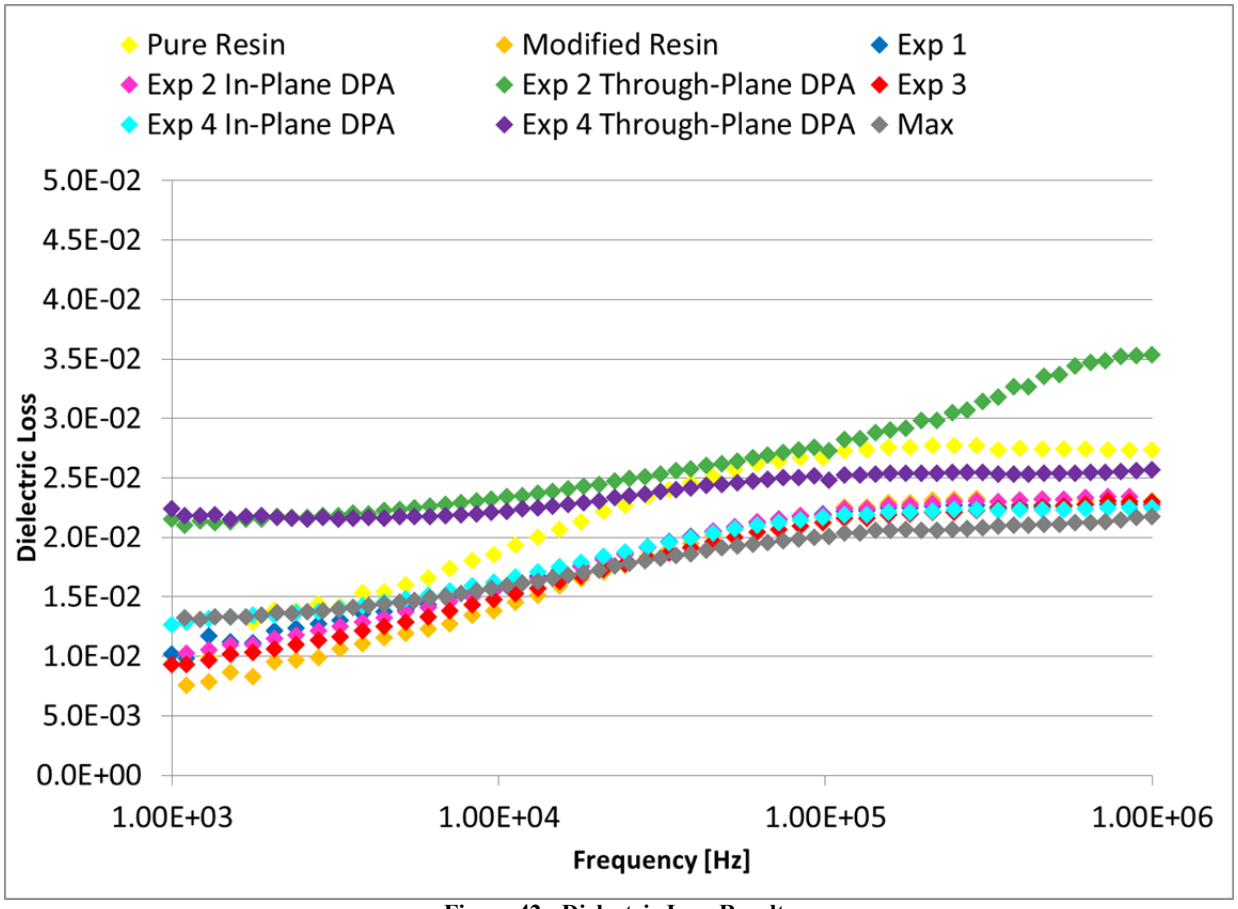


**Figure 42: Dielectric Loss Results**

### *5.4.1 Signal-to-Noise ($SN_L$) Ratio and Rank ($\Delta$) Analysis for $\varepsilon_r$*

For $\varepsilon_r$, $SN_L$ was used, as increasing $\varepsilon_r$ was an objective of this research. The results for the In-Plane and Through-Plane DPA studies can be found in Table 20 and Table 21, respectively. In each table, the maximum value for $SN_L$ is highlighted in yellow, with its corresponding controllable factors and experiment number. This represents the experiment with the optimum combination of parameters to maximize $\varepsilon_r$.

**Table 20: $SN_L$ Analysis for $\varepsilon_r$ from the In-Plane DPA Study**

| *In-Plane (IP) DPA Study* | | | | |
|---|---|---|---|---|
| **Dielectric Constant, $\varepsilon_r$** | | | | |
| **Experiment Number** | **Particle Volume Fraction ($V_f$)** | **Dielectrophoretic Assembly (DPA)** | **Particle Size(Crystal Structure)** | **$SN_L$ values for $\varepsilon_r$** |
| **1** | 25% | No | 100 (cubic) | 20.08 |
| **2-IP** | 25% | Yes | 200 (tetragonal) | 24.97 |
| **3** | 50% | No | 200 (tetragonal) | 30.08 |
| **4-IP** | 50% | Yes | 100 (cubic) | 25.89 |

**Table 21: $SN_L$ Analysis for $\varepsilon_r$ from the Through-Plane DPA Study**

| *Through-Plane (TP) DPA Study* | | | | |
|---|---|---|---|---|
| **Dielectric Constant, $\varepsilon_r$** | | | | |
| **Experiment Number** | **Particle Volume Fraction ($V_f$)** | **Dielectrophoretic Assembly (DPA)** | **Particle Size(Crystal Structure)** | **$SN_L$ values for $\varepsilon_r$** |
| **1** | 25% | No | 100 (cubic) | 20.08 |
| **2-TP** | 25% | Yes | 200 (tetragonal) | 26.69 |
| **3** | 50% | No | 200 (tetragonal) | 30.08 |
| **4-TP** | 50% | Yes | 100 (cubic) | 28.22 |

The $SN_L$ analyses from both the In-Plane and Through-Plane DPA studies, showed the optimum combination of parameters to maximize $\varepsilon_r$, were found with Experiment 3. These composites were made with 200 nm (tetragonal) particles, at a volume fraction of 50%, and without the application of DPA. The fact that specimens from Experiment 3 had the highest dielectric constant, in both the In-Plane and Through-Plane DPA studies, is believed to be due to high volume fraction (50%) of tetragonal particles, used to make the composite.

The rank analysis was completed for both the In-Plane and Through-Plane DPA studies, and the results are listed in Table 22 and Table 23, respectively. In each table, the parameter with the rank of 1 is highlighted in blue, along with its controllable factor. This represents the parameter with the largest impact on $\varepsilon_r$.

Table 22: Rank Analysis for $\varepsilon_r$ from the In-Plane DPA Study

| *In-Plane (IP) DPA Study* | | | |
|---|---|---|---|
| **Dielectric Constant, $\varepsilon_r$** | | | |
| **Mean $SN_L$ at Levels 1 and 2** | **Particle Volume Fraction ($V_f$)** | **Dielectrophoretic Assembly (DPA)** | **Particle Size (Crystal Structure)** |
| $\overline{SN}_1$ | 22.52 | 25.08 | 22.99 |
| $\overline{SN}_2$ | 27.99 | 25.43 | 27.52 |
| | | | |
| Δ | 5.46 | 0.35 | 4.53 |
| Rank | 1 | 3 | 2 |

Table 23: Rank Analysis for $\varepsilon_r$ from the Through-Plane Study

| *Through-Plane (TP) DPA Study* | | | |
|---|---|---|---|
| **Dielectric Constant, $\varepsilon_r$** | | | |
| **Mean $SN_L$ at Levels 1 and 2** | **Particle Volume Fraction ($V_f$)** | **Dielectrophoretic Assembly (DPA)** | **Particle Size(Crystal Structure)** |
| $\overline{SN}_1$ | 23.39 | 25.08 | 24.15 |
| $\overline{SN}_2$ | 29.15 | 27.45 | 28.38 |
| | | | |
| Δ | 5.76 | 2.37 | 4.23 |
| Rank | 1 | 3 | 2 |

For both the In-Plane and Through-Plane DPA studies, the rank analysis shows the particle volume fraction has the largest impact on $\varepsilon_r$.

### *5.4.2 Signal-to-Noise ($SN_s$) Ratio and Rank (Δ) Analysis for tan δ*

For tan $\delta$, $SN_S$ was used, as decreasing tan $\delta$ was an objective of this research. The results for the In-Plane and Through-Plane DPA studies can be found in Table 24 and Table 25, respectively. In each table, the maximum value for $SN_S$ is highlighted in yellow, with its corresponding controllable factors and experiment number. This represents the experiment with the optimum combination of parameters to maximize tan $\delta$.

Table 24: $SN_S$ Analysis for tan $\delta$ from the In-Plane DPA Study

| *In-Plane (IP) DPA Study* | | | | |
|---|---|---|---|---|
| **Dielectric Loss, tan $\delta$** | | | | |
| **Experiment Number** | **Particle Volume Fraction ($V_f$)** | **Dielectrophoretic Assembly (DPA)** | **Particle Size(Crystal Structure)** | **$SN_S$ values for tan $\delta$** |
| **1** | 25% | No | 100 (cubic) | 32.84 |
| **2-IP** | 25% | Yes | 200 (tetragonal) | 32.88 |
| **3** | 50% | No | 200 (tetragonal) | 32.74 |
| **4-IP** | 50% | Yes | 100 (cubic) | 32.96 |

Table 25: $SN_S$ Analysis for tan $\delta$ from the Through-Plane DPA Study

| *Through-Plane (TP) DPA Study* | | | | |
|---|---|---|---|---|
| **Dielectric Loss, tan $\delta$** | | | | |
| **Experiment Number** | **Particle Volume Fraction ($V_f$)** | **Dielectrophoretic Assembly (DPA)** | **Particle Size(Crystal Structure)** | **$SN_S$ values for tan $\delta$** |
| **1** | 25% | No | 100 (cubic) | 32.84 |
| **2-TP** | 25% | Yes | 200 (tetragonal) | 27.25 |
| **3** | 50% | No | 200 (tetragonal) | 32.74 |
| **4-TP** | 50% | Yes | 100 (cubic) | 31.81 |

The $SN_S$ analysis from the In-Plane DPA study showed the optimum combination of parameters to minimize tan $\delta$, were found with Experiment 4-IP. These composites were made with 100 nm (cubic) particles, at a volume fraction of 50%, and DPA was applied. For the Through-Plane DPA study, the $SN_S$ analysis showed the optimum combination of parameters to minimize tan $\delta$, were found with Experiment 1. These composited were made with 100 nm (cubic) particles, at 25% volume fraction, and without the application of DPA. In both studies, the tan d was minimized with the use of 100 nm (cubic) particles. This is also believed to be due to the lower polarization of the cubic particles, as compared to the tetragonal particles.

The rank analysis was completed for both the In-Plane and Through-Plane DPA studies, and the results are listed in Table 26 and Table 27, respectively. In each table, the parameter

with the rank of 1 is highlighted in blue, along with its controllable factor. This represents the parameter with the largest impact on tan $\delta$.

**Table 26: Rank Analysis for $\varepsilon_r$ from the In-Plane DPA Study**

| *In-Plane (IP) DPA Study* | | | |
|---|---|---|---|
| **Dielectric Loss, tan $\delta$** | | | |
| **Mean $SN_L$ at Levels 1 and 2** | **Particle Volume Fraction ($V_f$)** | **Dielectrophoretic Assembly (DPA)** | **Particle Size (Crystal Structure)** |
| $\overline{SN}_1$ | 32.86 | 32.79 | 32.90 |
| $\overline{SN}_2$ | 32.85 | 32.92 | 32.81 |
| | | | |
| $\Delta$ | 0.01 | 0.13 | 0.09 |
| Rank | 3 | 1 | 2 |

**Table 27: Rank Analysis for $\varepsilon_r$ from the Through-Plane Study**

| *Through-Plane (TP) DPA Study* | | | |
|---|---|---|---|
| **Dielectric Loss, tan $\delta$** | | | |
| **Mean $SN_L$ at Levels 1 and 2** | **Particle Volume Fraction ($V_f$)** | **Dielectrophoretic Assembly (DPA)** | **Particle Size(Crystal Structure)** |
| $\overline{SN}_1$ | 30.04 | 32.79 | 32.32 |
| $\overline{SN}_2$ | 32.27 | 29.53 | 29.99 |
| | | | |
| $\Delta$ | 2.23 | 3.27 | 2.33 |
| Rank | 3 | 1 | 2 |

For both the In-Plane and Through-Plane DPA studies, the rank analysis shows DPA has the largest impact on tan $\delta$.

### *5.4.3 Dielectric Constant Results Compared to Models*

There are a number of models that have been used to predict the dielectric constant of a two-phase dielectric composite material. The Series, Parallel and Cubic models are analogous to equivalent circuits for the composite in which the connectivity of the circuit elements are modeled after the connectivity of the phases in the composite[114]. A model developed by Maxwell was used to estimate randomly dispersed spheres in a matrix[10]. Lichtenecker developed

a logarithmic mixture formula that has been regarded as semi-empirical without firm theoretical justification[115]. These models assume that the dielectric properties are the result of the two phases only and that any effects of a third layer, e.g., interface, grain boundaries, etc., can be neglected. These models also assume that the properties of the two phases are uniform and constant throughout the material. A diagram of the Series, Parallel, Cubic and Maxwell models is shown in Figure 43.

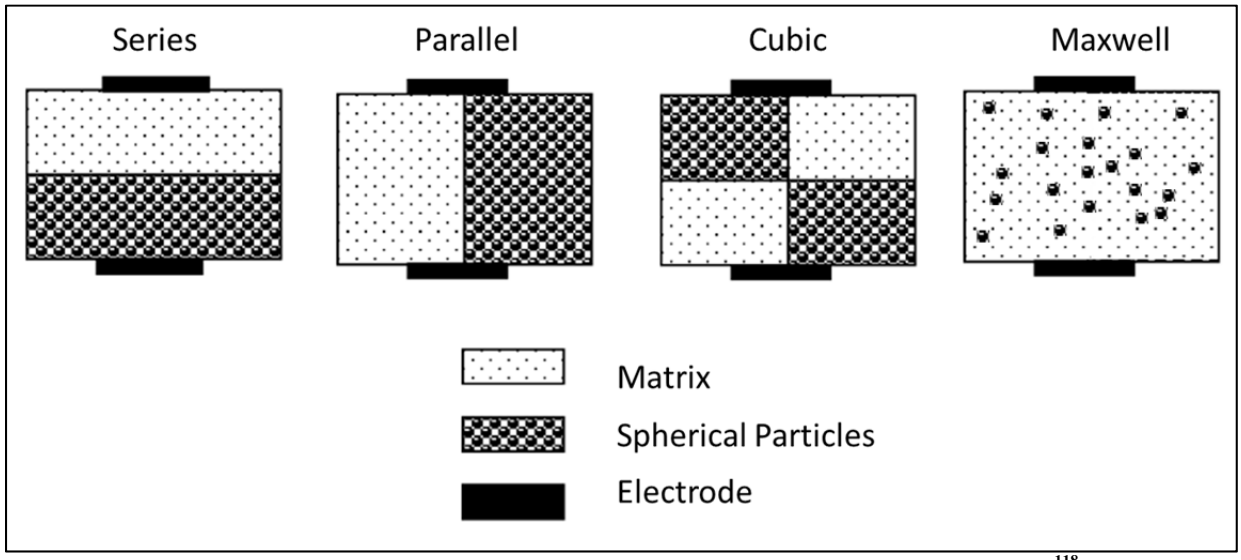


**Figure 43: Diagram of Series, Parallel, Cubic and Maxwell Dielectric Constant Models[118]**

These models were investigated for this work, and the mathematical expressions for the Series, Maxwell, Log, Parallel, and Cubic models are given in Equations 5.4.3.1 through 5.4.3.5, respectively[114-116]. The subscripts 1 and 2 in the following equations represent the matrix or phase 1 of the composite and the filler or phase 2 of the composite, respectively.

$$\varepsilon_{Series} = \left[\frac{V_1}{\varepsilon_1} + \frac{V_2}{\varepsilon_2}\right]^{-1} \qquad \textbf{Equation 5.4.3.1}$$

$$\varepsilon_{Maxwell} = \frac{V_1\varepsilon_1\Psi + V_2\varepsilon_2}{V_1\Psi + V_2} \quad \Psi = \frac{2}{3} + \frac{\varepsilon_2}{\varepsilon_1} \qquad \textbf{Equation 5.4.3.2}$$

$$\log \varepsilon_{\log} = V_1 \log \varepsilon_1 + V_2 \log \varepsilon_2$$ **Equation 5.4.3.3**

$$\varepsilon_{Parallel} = V_1 \varepsilon_1 + V_2 \varepsilon_2$$ **Equation 5.4.3.4**

$$\varepsilon_{Cubic} = \frac{\varepsilon_1 \varepsilon_2}{(\varepsilon_2 - \varepsilon_1) V^{\frac{-1}{3}} + \varepsilon_1 V_1^{\frac{-2}{3}}} + \varepsilon_2 (1 - V_1^{\frac{2}{3}})$$ **Equation 5.4.3.5**

A plot of the dielectric constant results compared to the Series, Maxwell and Log models is shown in Figure 44 and a plot of the results compared to the Parallel and Cubic Models is shown in Figure 45. The dielectric constant of the matrix used in the model calculations is 5.78, which is the value measured for the resin with 5 wt% HELOXY 61 modifier. The dielectric constant of the particles used in the model calculations is 2000, and it was taken from the literature[117].

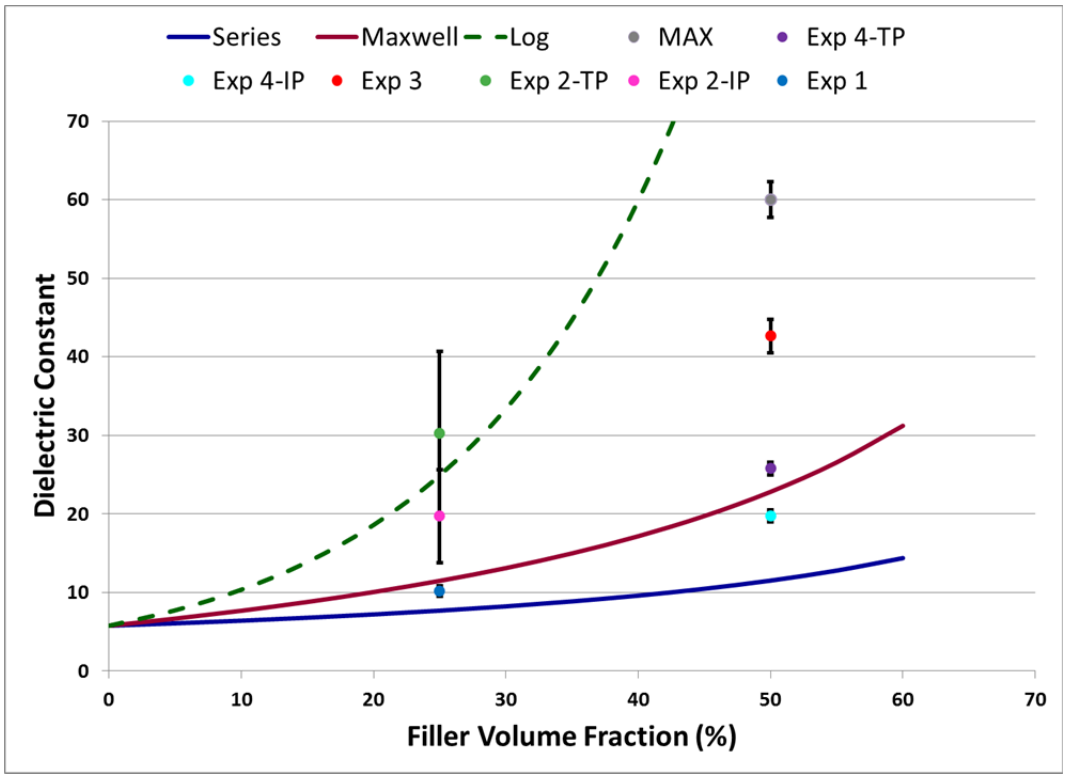


**Figure 44: Series, Log and Maxwell Models Compared to Dielectric Constant Results**

Experiments 2 In-Plane and Through-Plane, with their large standard deviations, were in agreement with the Log model, and Experiment 1 was in agreement with the Maxwell Model. None of the 50% volume fraction composites were in agreement with the models. It is unclear if these models account for such a high particle loading. While not in agreement, all of the 50% volume fraction models fall between the Series and Log models. None of the experimental results were in agreement with the Parallel or Cubic models.

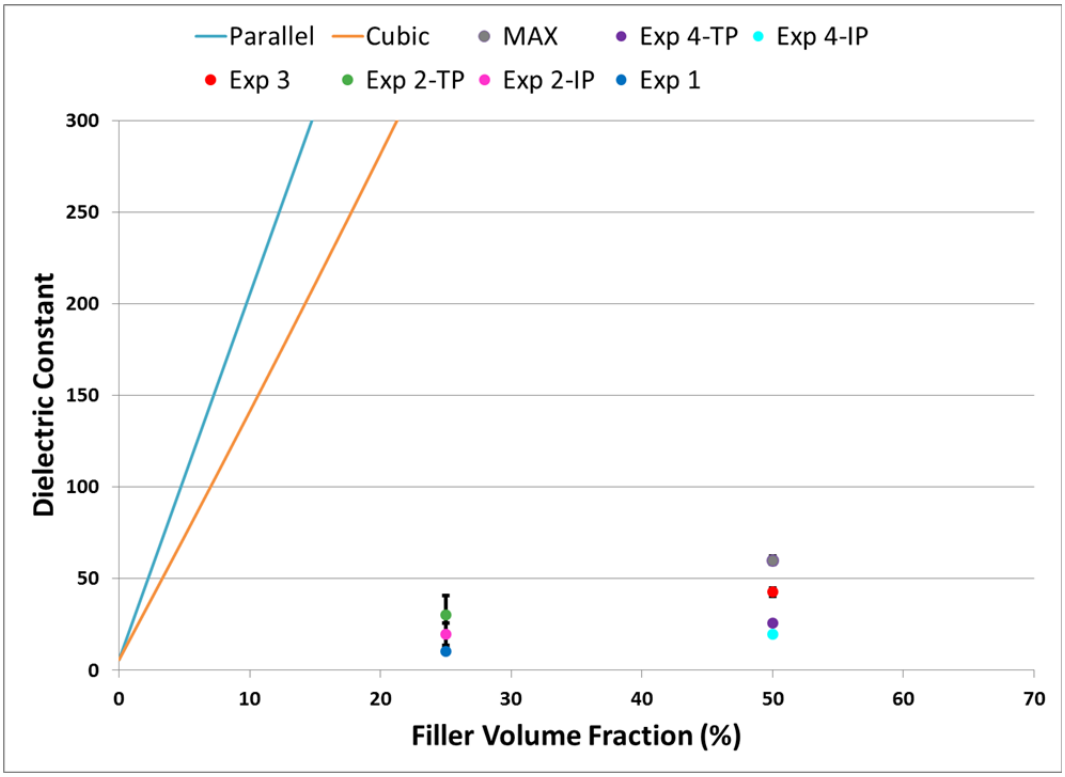


**Figure 45: Parallel and Cubic Models Compared to Dielectric Constant Results**

## 5.5 *Numerical Simulation*

For a dielectric sphere in a uniform electric field, the field inside the sphere is given by Equation 5.5.1[1].

$$\vec{E} = -\vec{\nabla}V \qquad \textbf{Equation 5.5.1}$$

The volume charge density is given by Equation 5.5.2[1].

$$\rho = -\vec{\nabla} \bullet \vec{P} \qquad \textbf{Equation 5.5.2}$$

The Polarization was defined by Equation 1.3.7, and substituting it into Equation 5.5.2, the charge density is given by Equation 5.5.3.

$$\rho_v = \vec{\nabla} \bullet \left( \varepsilon_0 \varepsilon_r \vec{E} \right) \qquad \textbf{Equation 5.5.3}$$

COMSOL Multiphysics software was used to solve Equation 5.5.1 and 5.5.3; to calculate the magnitude of the electric field inside the composite; and to calculate the charge on the surface of the material. The geometry used for the COMSOL simulation includes a rectangular prism of epoxy, with aligned, spherical, $BaTiO_3$ particles inside. A parametric sweep was used, and for each iteration, the number of particles was reduced by one, starting with ten particles, which simulates a particle loading of 50% volume fraction, and ending with one particle, which simulated a condition that was very close to pure resin. The 25% volume fraction case was simulated with five particles in the prism. A drawing of the model, with ten particles, is shown in Figure 46.

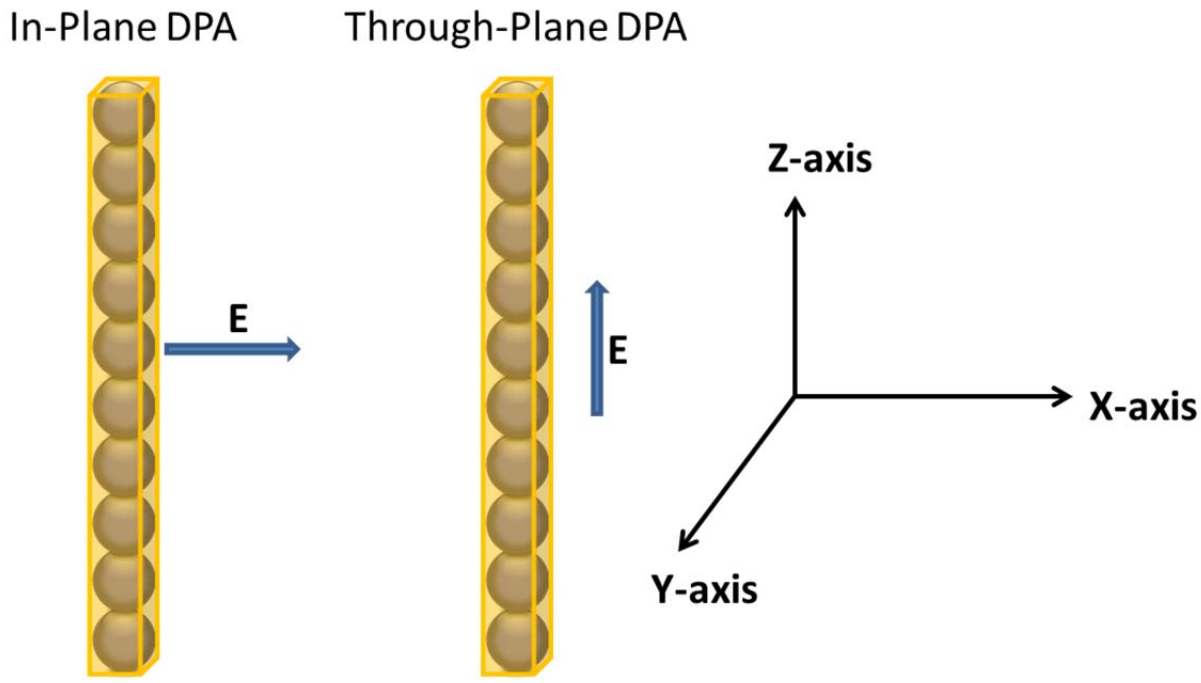


**Figure 46: Geometry for COMSOL Models of In-Plane and Through-Plane DPA at 50% Volume Fraction Particles**

The prism had four surfaces, hereafter referred to as faces, of equal dimensions. It also had a top and bottom surface, which had equal dimensions but were not the same dimensions as the faces. The boundary conditions used on the bottom surface of each prism included one fixed corner and a roller boundary everywhere else. There was also a symmetry condition on all four faces, simulating an infinite array of this geometry throughout the material. For the In-Plane DPA models, ground was on the right face of the prism and the electric field was applied in a direction parallel to the x-axis. For the Through-Plane DPA models, ground was on the top surface and the field was applied in a direction parallel to the z-axis. See Figure 46.

The charge data was calculated by integrating the energy density over the surface of the electrodes. For the In-Plane DPA study, the electrodes were on the faces of the prism in the y-z plane, perpendicular to the x-axis. For the Through-Plane DPA study, the electrodes were on the top and bottom surfaces of the prism, in the x-y plane, perpendicular to the z-axis. Using the charge values determined by COMSOL, Equations 1.2.2, 1.2.5, and 1.2.6 were used to calculate the effective dielectric constant of the composites. The dielectric constant values calculated from the COMSOL data were compared to the experimental results, and this comparison data is listed in Table 28.

**Table 28: Dielectric Constant Values Determined by Numerical Simulation Compared to Experimental Results**

| ***COMSOL Calculated Dielectric Constant, $\varepsilon_r$, with Experimental Results*** | | | |
|---|---|---|---|
| Particle Volume Fraction | $\varepsilon_r$ Calculated with COMSOL | Measured $\varepsilon_r$ | Experiment |
| 50% | 53.32 | 60.01 | MAX |
| 50% | 30.68 | 19.76 | 4-IP |
| 25% | 8.91 | 10.17 | 1 |
| 25% | 18.62 | 19.71 | 2-IP |

The results for $\varepsilon_r$ calculated with COMSOL are in good agreement with the experimental results, except for the Experiment 4 In-Plane DPA case. The difference is believed to be due to the fact that not enough epoxy was included in the geometry for this model, along the symmetry planes.

As a result, COMSOL assumes the particles are aligned and in contact in the x-direction, when they are actually aligned and in contact only in the z-direction. The electrostatic field results are shown in Figure 47 – 52.

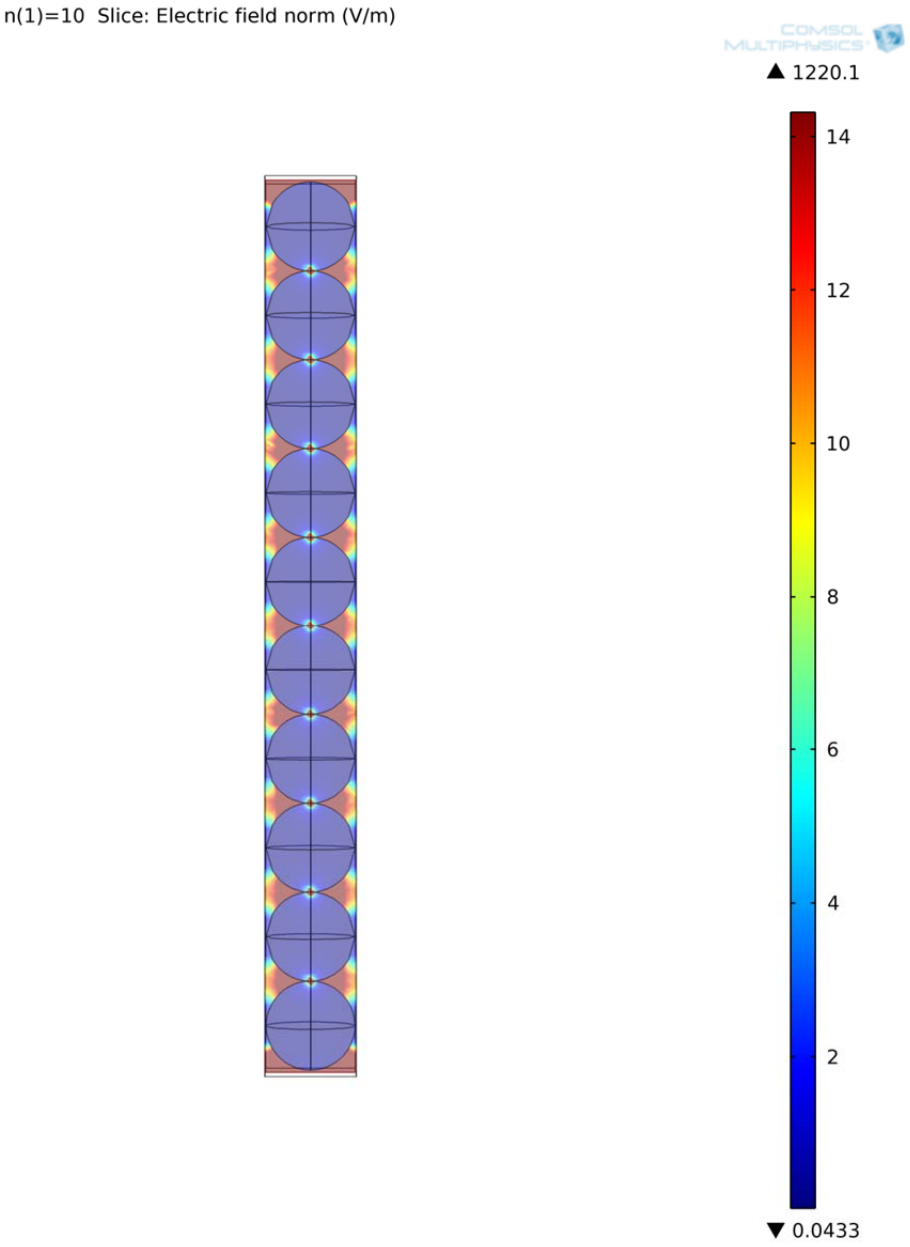


**Figure 47: Calculated Magnitude of the Electric Field in the Exp 4-TP Composite**

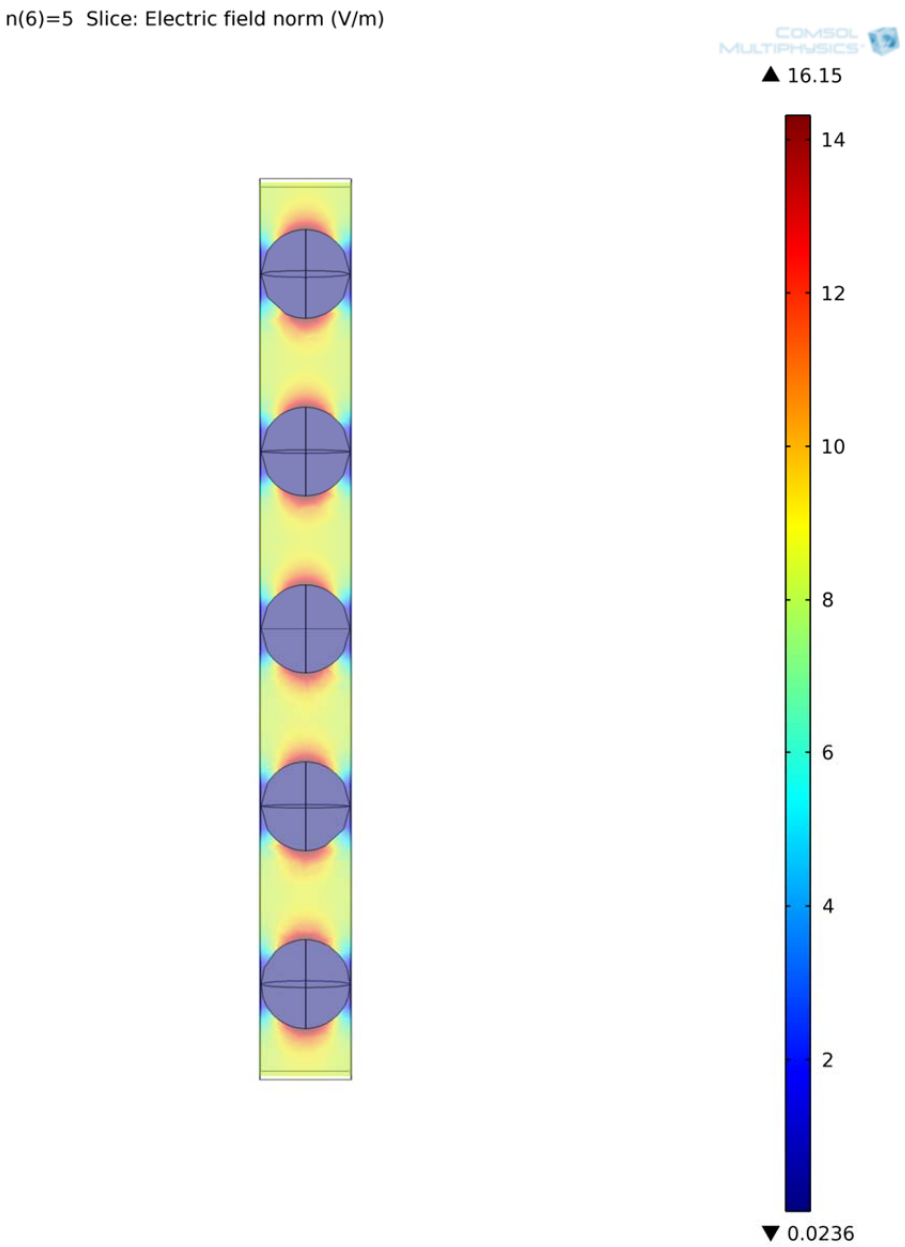


**Figure 48: Calculated Magnitude of the Electric Field in the Exp 1 Composite**

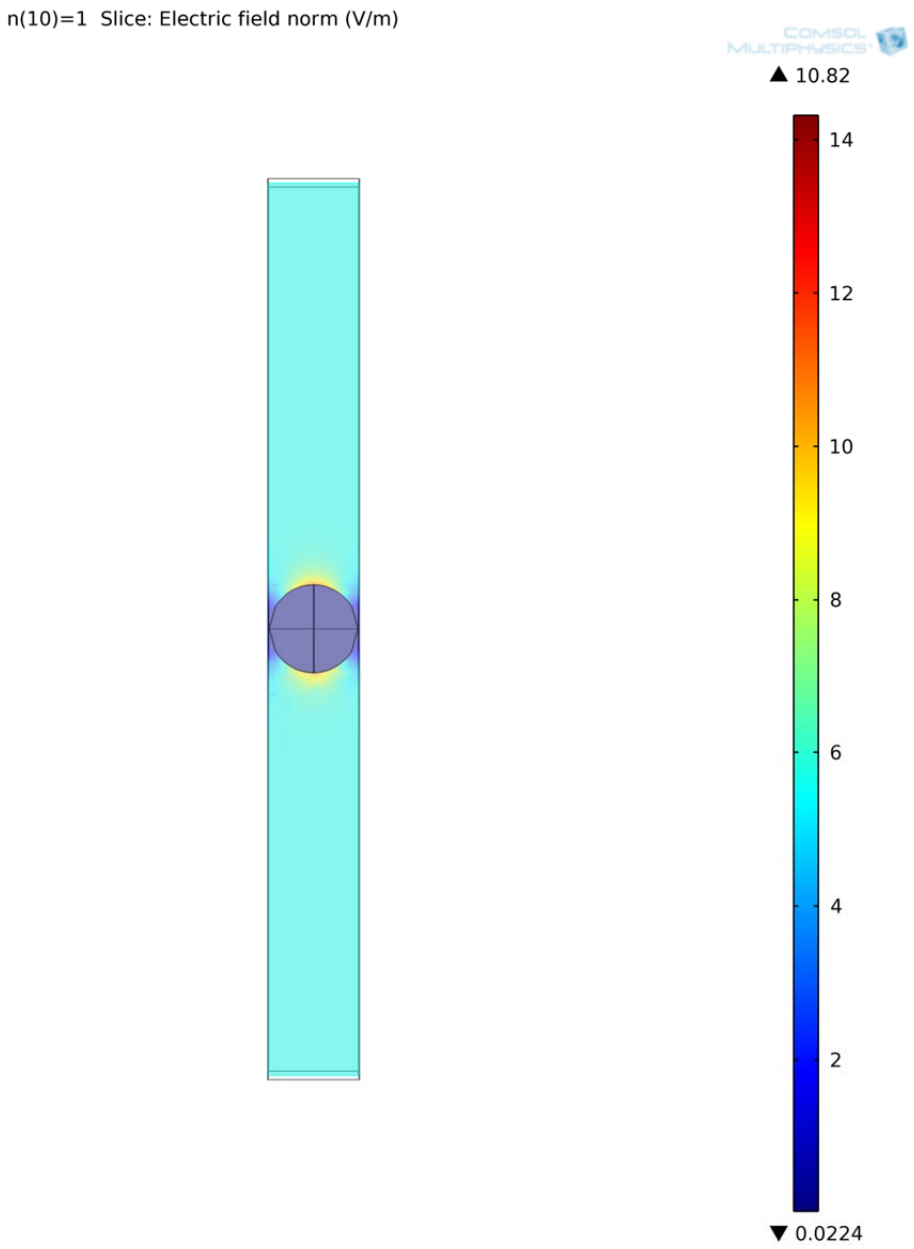


**Figure 49: Calculated Magnitude of the Electric Field for 1 Particle in Epoxy, 100 nm (Cubic)**

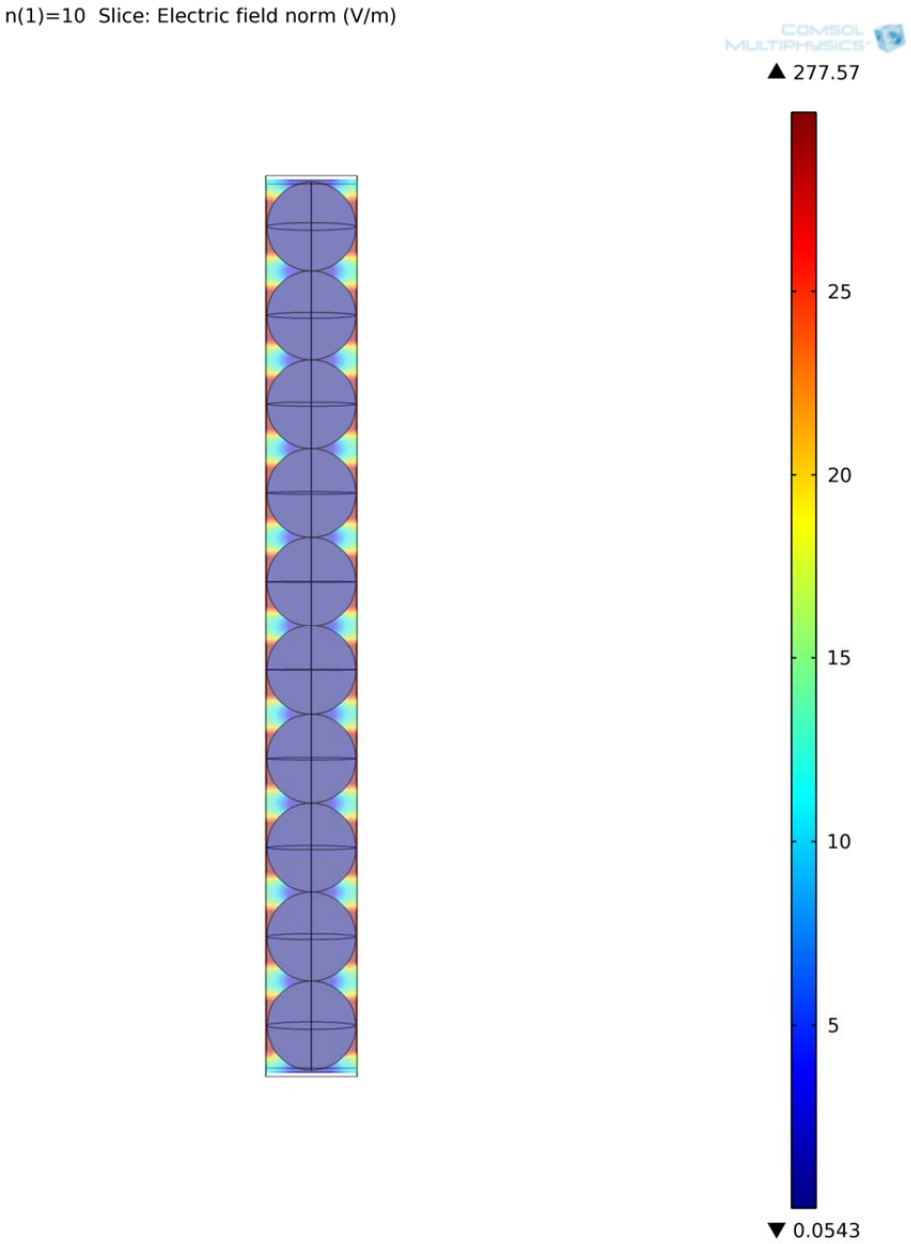


**Figure 50: Calculated Magnitude of the Electric Field for Exp 4-IP Composite**

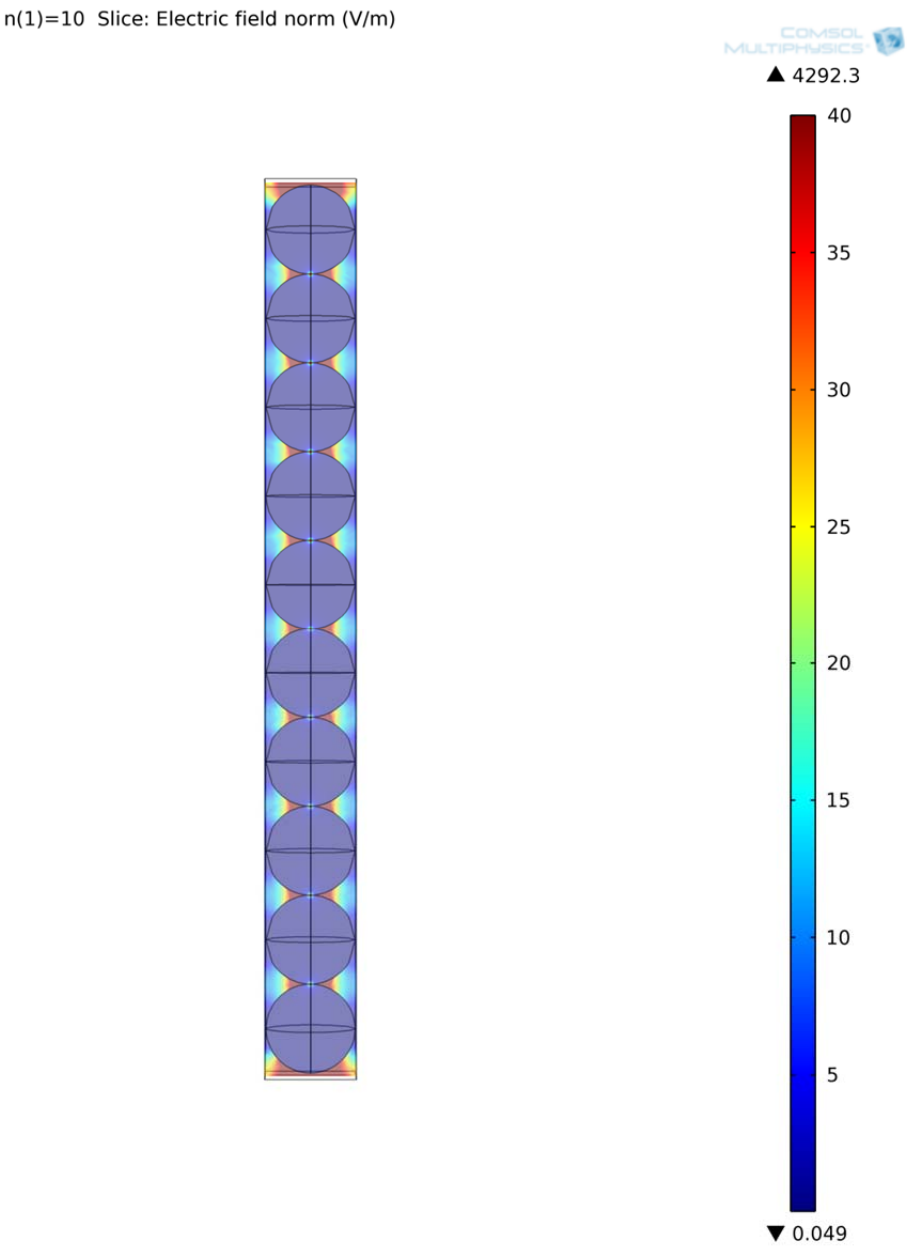


**Figure 51: Calculated Magnitude of Electric Field for Exp MAX Composite**

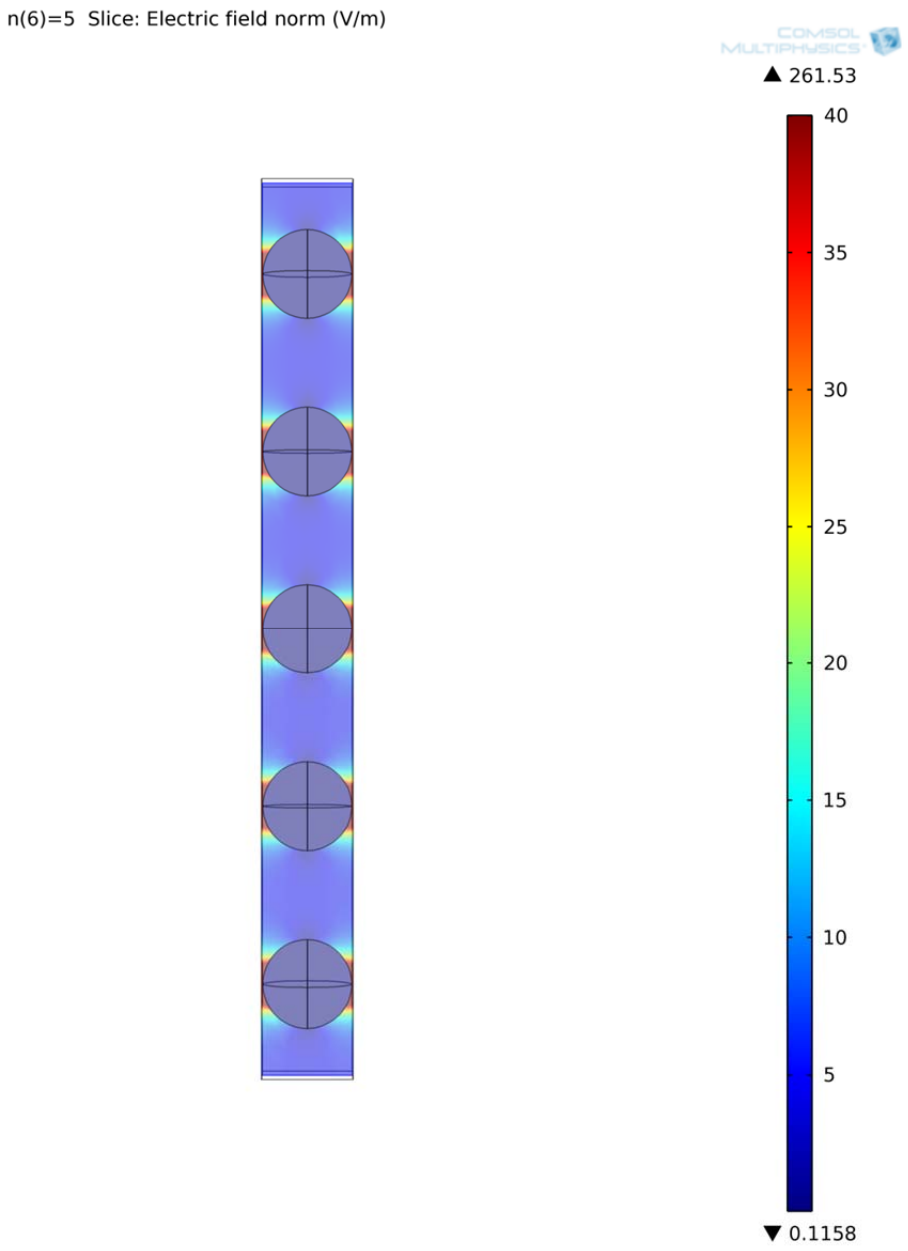


**Figure 52: Calculated Magnitude of Electric Field for Exp 2-IP Composite**

# *Chapter 6: Conclusions and Future Work*

Multifunctional composite materials were developed to enhance the dielectric properties of an epoxy polymer by reinforcing it with ceramic barium titanate ($BaTiO_3$) particles. The parameters varied were the volume fraction ($V_f$) of the particles; the particle size (crystal structure); and the use of dielectrophoretic assembly (DPA) by applying an electric field during the composite curing process. In parametric Study 1, DPA was applied in the plane of the mold used to manufacture composite specimens, referred to as In-Plane DPA. For the In-Plane DPA study, the optimum combination of parameters required to achieve the desired material properties are summarized in Table 29. To maximize failure stress, the optimum combination of parameters were found in Experiment 1, with 25% volume fraction, 100 nm (cubic) particles, and no application of DPA. To maximize Young's modulus and dielectric constant, the optimum combination of parameters were found in Experiment 3, 50% volume fraction, 200 nm (tetragonal) particles, and no application of DPA. To minimize dielectric loss, the optimum combination of parameters were found in Experiment 4, with 50% volume fraction, 100 nm (cubic), and with DPA applied. No experiment had the optimum combination of parameters for all of the desired material characteristics.

**Table 29: Summary of Signal-Noise-Ration Results for the In-Plane DPA Parametric Study**

| ***Signal to Noise Ratio Analysis Summary for In-Plane DPA*** | | | | |
|---|---|---|---|---|
| **Experiment Number** | **$SN_L$ values for FS** | **$SN_L$ values for E** | **$SN_L$ values for $\varepsilon_r$** | ***$SN_S$* values for *$tan\delta$*** |
| **1** | 35.59 | 15.14 | 20.08 | 32.84 |
| **2-IP** | 33.54 | 19.10 | 24.97 | 32.88 |
| **3** | 28.72 | 23.14 | 30.08 | 32.74 |
| **4-IP** | 34.09 | 22.60 | 25.89 | 32.96 |

A rank analysis was also completed to determine which parameter had the largest impact on the desired material property. A summary of these parameters is given in Table 30. Particle

size (crystal structure) was found to have the largest impact on maximizing failure stress. Particle volume fraction was found to be the most important parameter for maximizing Young's modulus and dielectric constant. For minimizing dielectric loss, DPA was found to have the largest impact.

**Table 30: Summary of Most Influential Parameters on Material Properties for In-Plane Study**

| ***Rank Analysis Summary for In-Plane DPA Study*** | |
|---|---|
| **Manufacturing Parameter** | **Desired Characteristic Outcome** |
| Particle Size(Crystal Structure) | Maximize FS |
| Particle Volume Fraction ($V_f$) | Maximize Young's Modulus |
| Particle Volume Fraction ($V_f$) | Maximize Dieletric Constant |
| Dielectrophoretic Assembly (DPA) | Minimize Dielectric Loss |

In the other parametric study, DPA was applied through the plane of the mold, referred to as Through-Plane DPA. For the Through-Plane DPA study, the optimum combination of parameters required to achieve the desired material properties are summarized in Table 31.

**Table 31: Summary of Signal-Noise-Ration Results for the Through-Plane DPA Parametric Study**

| ***Signal to Noise Ratio Analysis Summary with Through-Plane DPA*** | | | | |
|---|---|---|---|---|
| **Experiment Number** | **$SN_L$ values for FS** | **$SN_L$ values for E** | **$SN_L$ values for $\varepsilon_r$** | **$SN_S$ values for ($\tan\delta$)** |
| **1** | 35.59 | 15.14 | 20.08 | 32.84 |
| **2-TP** | 28.31 | 17.76 | 26.69 | 27.25 |
| **3** | 28.72 | 23.14 | 30.08 | 32.74 |
| **4-TP** | 22.24 | 21.70 | 28.22 | 31.81 |

To maximize failure stress, and to minimize dielectric loss, the optimum combination of parameters were found in Experiment 1, with 25% volume fraction, 100 nm (cubic) particles, and no application of DPA. To maximize Young's modulus and dielectric constant, the optimum combination of parameters were found in Experiment 3, 50% volume fraction, 200 nm (tetragonal) particles, and no application of DPA. As in the case for the In-Plane study, no

experiment had the optimum combination of parameters for all of the desired material characteristics.

A rank analysis was also completed to determine which parameter had the largest impact on the desired material property. A summary of these parameters is given in Table 32.

**Table 32: Summary of Most Influential Parameters on Material Properties for Through-Plane Study**

| ***Rank Analysis Summary for Through-Plane DPA Study*** | |
|---|---|
| **Manufacturing Parameter** | **Desired Characteristic Outcome** |
| Dielectrophoretic Assembly (DPA) | Maximize FS |
| Particle Volume Fraction ($V_f$) | Maximize Young's Modulus |
| Particle Volume Fraction ($V_f$) | Maximize Dielectric Constant |
| Dielectrophoretic Assembly (DPA) | Minimize Dielectric Loss |

Dielectrophoretic Assembly was found to have the largest impact on maximizing failure stress and minimizing dielectric loss. Particle volume fraction was found to be the most important parameter for maximizing Young's modulus and dielectric constant.

For both studies, the optimum combination of parameters and the most influential parameters on a property were determined through statistical methods, and supported by the physics which govern the material properties. An electrostatic numerical simulation was also completed to calculate the magnitude of the electric field inside the composite, and the charge on the surface of the material. The numerical simulation results were in good agreement with the experimental results.

## *6.1 Future Work*

A ceramic material is polycrystalline meaning it is composed of a large number of randomly oriented crystallites. Due to this polycrystalline structure, a ceramic is expected to be isotropic with respect to properties. Poling is a process in which a strong, direct current (DC), electric field is temporarily applied to an isotropic, ferroelectric ceramic to permanently polarize

it. Under the right conditions of temperature and time, the polar axes align as closely to the field direction as possible[5]. The degree of alignment is limited by what the crystal structure will allow as well as the local environment. Figure 53 shows an illustration of the poling results.

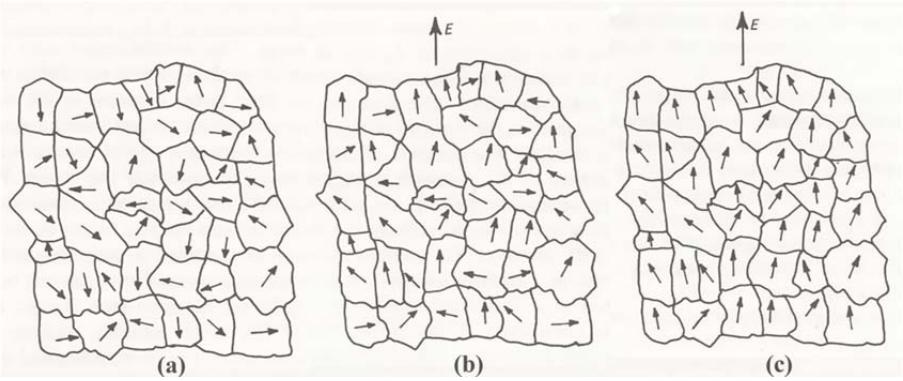


**Figure 53: (a) Ceramic Before Poling (b) Ceramic Poled 180° (c) Ceramic Poled 180° and 90°[5]**

For this work, poling could orient the dipoles in the nanoparticles, in the direction of the electric field. All of the composite specimens should be poled, in an effort to increase the dielectric constant above the values achieved in this study.

Experiment 2 Through-Plane should also be repeated, using the same DPA parameters used during Experiment MAX. This should eliminate the problems with arcing that occurred, allowing DPA to run continuously, over the 24-hour period required to cure the composites. This may also lead to improved dielectric properties as enough time would be allowed for chain formation between the particles. A greater the degree of particle connectivity should lead to better dielectric properties.

# *References*


1. Giancoli, D. C. (2000). *Physics for Scientists & Engineers with Modern Physics* (Third ed.). Upper Saddle River , NJ, USA: Prentice Hall.

2. Birks, J. B. (1960). *Modern Dielectric Material.* London: Heywood & Company Ltd.

3. Buchanan, R. C. (1991). *Ceramic Materials for Electronics Processing, Properties and Applications* (2nd ed.). New York, NY, USA: Marcel Dekker Inc.

4. (n.d.). (D. o. University, Producer, & Addison Wesley Longman, Inc.) Retrieved June 4, 2014, from Department of Physics & Astronomy San Jose State University: http://www.physics.sjsu.edu/becker/physics51/images/25_14Polarization.JPG

5. Moulson, A. J. (1990). *Electroceramics: Materials, Properties, Applications.* London, England: Chapman & Hall.

6. (n.d.). Retrieved June 2014, from Thomasnet.com: http://www.thomasnet.com/articles/image/automation-electronics/supercapacitor-resize.jpg

7. (n.d.). Retrieved August 3, 2014, from Desktop Class - Online Classroom: http://www.desktopclass.com/wp-content/uploads/2011/06/Picture-1-12-39-20.png

8. Byro, A. H. (2014). *Property Enhancement of Dielectric Nanoparticles via Surface Functionalization (Doctoral Dissertation) The City University of New York, New York, NY.,*. Ann Arbor, MI, USA: ProQuest LLC.

9. (n.d.). Retrieved August 5, 2024, from Passive Component Magazine: http://www.passivecomponentmagazine.com/

10. Roberts, M. M. (1997). *Evaluating the Dielectrophoretic Assembly of Composite Materials (Master's Thesis).* Los Angeles, CA, USA: University of California Los Angeles.

11. Carrodeguas, R. G., et al. (2003). Injectable Acrylic Bone Cements for Vertebroplasty with Improved Properties. *Journal of Biomedical Materials Research Part B: Applied Biomaterials*(68B), 94-104.

12. Chiang, C. K., et al. (2001). Dielectric Properties and Morphology of Ferroelectric Ceramic-Polymer Composite Films. *Materials Research Society Symposium Proceedings*, *682E*, pp. N.6.9.1 – 6. San Francisco.

13. Liang, S., et al. (1998). Barium Titanate/Epoxy Composite Dielectric Materials for Integrated Thin Film Capacitors. *IEEE Electronic Components and Technology Conference*, (pp. 171-5). Seattle.

14. Cho S., et al. (2004). Study on Epoxy/BaTiO3 Composite Embedded Capacitor Films (ECFs) for Organic Substrate Applications. *Materials Science and Engineering B*(110), 233-9.

15. Korleski, J. E., et al. (1997). New Composite Organic Dielectric for High Performance Flip Chip Single Chip Packages. *IEEE Electronic Components and Technology Conference*, (pp. 1015-21). San Jose.

16. Balasubramanian, S. (2011). *Polymer Composite Dielectric Materials for Pulse Power Applications (Doctoral Dissertation).* Ann Arbor, MI, USA: ProQuest.

17. Kim, P. (2008). *Surface Modification of Nanoparticles for Polymer/Ceramic Nanocomposites and Their Applications (Doctoral Dissertation) Georgia Institute of Technology, Atlanta, GA.,.* Ann Arbor, MI, USA: ProQuest.

18. Newnham, R. E., et al. (1980, December). Composite Piezoelectric Transducers. *Materials in Engineering, 2*, 93-106.

19. Hsiang, H., et al. (2001). Effects of particle size of BaTiO3 powder on the dielectric properties of BaTiO3 polyvinylidene fluoride composites. *Journal of Materials Science*(36), 3809-15.

20. Pohl, H. A. (1978). *Dielectrophoresis.* New York: Cambridge University Press.

21. Randall, C. A., et al. (1996). Electric Field Processing of Ferroelectric Particulate Ceramics and Composites. *IEEE International Symposium on Applications of Ferroelectrics*, *1*, pp. 189-92. East Brunswick.

22. Khastgir, D., Adachi, K. (1999). Piezoelectric and Dielectric Properties of Siloxane Elastomers Filled with Barium Titanate. *Journal of Polymer Science: Part B: Polymer Physics*(37), 3065-70.

23. Bowen, C. P., et al. (1998). Dielectric Properties of Dielectrophoretically Assembled Particulate-polymer Composites. *Journal of Materials Research, 13*(1), 205-10.

24. Collins, D. E., Slamovich, E. B. (1999). Preparation of a Homogeneously Dispersed BaTiO3/Polymer Nanocomposite Thin Film. *Chemistry of Materials*(11), 2319-21.

25. Lee, T., et al. (2001). Barium Titanate Nanoparticles in Block Copolymer. *Langmuir*(17), 7656-63.

26. Hirano, S., et al. (2003). In Situ Processing of Nano Crystalline Oxide Particles/Polymer Hybrid. *Journal of Sol-Gel Science and Technology*(26), 35-41.

27. Somani, P., et al. (1999). Charge Transport Mechanism And The Effect of Poling On The Current-Voltage Characteristics Of Conducting Polyaniline-BaTiO3 Composites. *Synthetic Metals*(106), 53-8.

28. Patil, R. C., et al. (2001). Piezoresistivity of Conducting Polyaniline/BaTiO3 Composites. *Journal of Materials Research, 16*(7), 1982-88.

29. Blum, Y. D., et al. (2001). Nanocomposites by Covalent Bonding between Inorganic Nanoparticles and Polymers. *Materials Research Society Symposium*, *676*, pp. Y1.8.1-8. San Francisco.

30. Wang, J., et al. (2003). Preparation and Electrical Properties of Humidity Sensing Films of BaTiO3/Polystrene Sulfonic Sodium. *Materials Chemistry and Physics*(78), 746-50.

31. Rong, M. Z., et al. (2003). Graft polymerization onto inorganic nanoparticles and its effect on tribological performance improvement of polymer composites. *Tribology International*(36), 697-707.

32. Chen, L. F., et al. (2004). Preparation and Properties of Polymer Matrix Piezoelectric Composites Containing Aligned BaTiO3 Whiskers. *Journal of Materials Science*(39), 2997-3001.

33. Kuo, D. H., et al. (2004). Dielectric Properties of Three Ceramic/Epoxy Composites. *Materials Chemistry and Physics*(85), 201-6.

34. Rao, Y., Wong, C. P. (2004). Material Characterization of a High-Dielectric-Constant Polymer-Ceramic Composite for Embedded Capacitor for RF Applications. *Journal of Applied Polymer Science*(92), 2228-31.

35. Tchmyreva, V. V., et al. (2004). Electrophysical Properties of Polymer Based Composites with Barium Titanate (BaTiO3). *Ferroelectrics*(307), 233-42.

36. Grewe M. G., et al. (1990). Acoustic Properties of Particle/Polymer composites for Ultrasonic Transducer Backing Applications. *IEEE Transactions on Ultrasonics, Ferroelectrics and Frequency Control, 37*(6), 506-14.

37. Orlowska, S. et al. (2002). Barium titanate particle model inquiry through effective permittivity measurements and boundary integral equation method based simulations of the BaTiO3-epoxy resin composite material. *Journal of Physics D: Applied Physics*(35), 2656-60.

38. Tripathi, A. K., et al. (1996). Optically Nonlinear And Transparent Polyimide:Barium Titanate Films-Preparation And Characterization. *IEEE International Symposium on Electrets*, (pp. 438-43). Shanghai.

39. Roberts, S. (1947). Dielectric and Piezoelectric Properties of Barium Titanate. *Physical Review Letters*(71), 890-95.

40. Barrett, J. (1952). Dielectric Constant in Perovskite Type Crystals. *Physical Review Letters*(86), 118-20.

41. Frey, M. H., Payne, D. (1993). Nanocrystalline Barium Titanate: Evidence for the Absence of Ferroelectricity in Sol-Gel Derived Thin-Layer Capacitors. *Applied Physics Letters*(63), 2753-55.

42. Wang, S.-F.; Dayton, G. O. (1999). Dielectric Properties of Fine-Grained Barium Titanate Based X7R Materials. *Journal of the American Ceramic Society, 82*(10), 2677-82.

43. Polotai, A., et al. (2005). A Novel Approach to Sintering Nanocrystalline Barium Titanate Ceramics. *Journal of the American Ceramic Society*(88), 3008-12.

44. López, M., et al. (1999). Characterization of Barium Titanate Powders: Barium Carbonate Identification. *Journal of the American Ceramic Society*(82), 1777-86.

45. Deng, X. et al. (2006). Ferroelectric properties of nanocrystalline barium titanate ceramics. *Applied Physics Letters*(88), 252905.

46. Li, J., et al. (2006). Dielectric Relaxation in Gigahertz Region and Phase Transition of BaTiO3-Based Ceramics. *Journal of Applied Physics 024106*(100).

47. Hennings, D., et al. (2001). Defect Chemistry and Microstructure of Hydrothermal Barium Titanate. *Journal of the American Ceramic Society, 84*(1), 179-82.

48. Kim, E., et al. (2013). Second-Harmonic Generation of Single BaTiO3 Nanoparticles down to 22 nm Diameter. *ACS Nano, 7*(6), 5343-49.

49. Teranishi, T., et al. (2010). Ferroelectrics and Frequency Control. *Analysis of polarization behavior in relaxation of BaTiO3-based ferroelectrics using wideband dielectric spectroscopy, IEEE Transactions on Ultrasonics, 57*(10), 2118-26.

50. Smith, M. B., et al. (2008). Crystal Structure and the Paraelectric-to-Ferroelectric Phase Transition of Nanoscale BaTiO3. *Journal of the American Chemical Society, 130*(22), 6955-63.

51. Polotai, A. V., et al. (2004). The XRD and IR Study of the Barium Titanate Nano-Powder Obtained Via Oxalate Route. *Ferroelectrics, 298:1*, 243-51.

52. Adair, J. H., et al. (2006). The Role of Material Chemistry in Processing BaTiO3 in Aqueous Suspensions. *Journal of the American Ceramic Society, 89*(6), 1853-60.

53. Yashima, M, et al. (2005). Size effect on the crystal structure of barium titanate nanoparticles. *Journal of Applied Physics*(98), 014313.

54. Zeng, X., et al. (2011). Microstructure, thermal and dielectric properties of homogeneous bismaleimide-triazine/barium titanate nanocomposite films. *Materials Chemistry and Physics, 131*(1-2), 387-92.

55. Rabuffetti, F. A, Brutchey, R. L. (2012). Structural Evolution of BaTiO3 Nanocrystals Synthesized at Room Temperature. *Journal of the American Chemical Society, 134*(22), 9475-87.

56. Busca, G., et al. (1994). Solid-State and Surface Spectroscopic Characterization of BaTiO3 Fine Powders. *Chemistry of Materials*(6), 955-61.

57. Callister, W. D., Jr. (2000). *Materials Science and Engineering An Introduction* (5th ed.). New York, NY, USA: John Wiley & Sons, Inc.

58. Lee, T., Aksay, A. (2001). Hierarchical Structure – Ferroelectricity Relationships of Barium Titanate Particles. *Crystal Growth & Design, 1*(5), 401-19.

59. Wada, S., et al. (2003). Preparation of nm-Sized Barium Titanate Fine Particles and Their Powder Dielectric Properties. *Japanese Journal of Applied Physics Part 1, 42*(9B), 6188-95.

60. Xu, H., Gao, L. (2004). Hydrothermal Synthesis of High-purity BaTiO3 Powders: Control of Powder Phase and Size, Sintering Density, and Dielectric Properties. *Materials Letters*(58), 1582-6.

61. Ulrich, R., et al. (2000). Comparison of Paraelectric and Ferroelectric Materials for Applications as Dielectrics in Thin Film Integrated Capacitors. *International Journal of Microcircuits and Electronic Packaging, 23*(2), 172-80.

62. (n.d.). Retrieved September 28, 2012, from Nanostructured and Amorphous Materials: http://nanoamor.com/inc/sdetail/16421

63. (n.d.). Retrieved September 28, 2012, from Nanostructured and Amorphous Materials: http://nanoamor.com/inc/sdetail/20905

64. *High-Performance Composites.* (2005, May). Retrieved January 14, 2011, from CompositesWorld: http://www.compositesworld.com/articles/composite-fan-blade-containment-case

65. *Patentimages.storage.googleapis.com*. (n.d.). Retrieved March 4, 2013, from http://patentimages.storage.googleapis.com/US6180696B1/US06180696-20010130-C00005.png

66. (March 2005). *EPON™ Resin 862 Technical Data Sheet.* Hexion Specialty Chemicals.

67. (August 2007). *EPIKURE ™ Curing Agent 3230 Technical Data Sheet.* Hexion Specialty Chemicals.

68. Guo, Z., et al. (2008). Strengthening and Thermal Stabilization of Polyurethane Nanocomposites with Silicon Carbide Nanoparticles by a Surface-initiated-polymerization Approach. *Composites Science and Technology, 68*(1), 164-70.

69. Guo, Z. et al. (2006). Surface Functionalized Alumina Nanoparticle Filled Polymeric Nanocomposites with Enhanced Mechanical Properties. *Journal of Materials Chemistry, 16*(27), 2800-8.

70. (March 2012). *3-(Trimethoxysilyl)propyl methacrylate Material Safety Data Sheet.* Sigma-Aldrich.

71. *Epoxy Diluents and Modifiers*. (n.d.). Retrieved January 10, 2014, from Air Products: http://www.airproducts.com/products/Chemicals/Epoxy-Diluents-Modifiers.aspx

72. (August 2011). *HELOXY™ 61 Epoxy Functional Modifier Technical Data Sheet.* Hexion Specialty Chemicals.

73. Campbell, F. C. (2010). Introduction to Composite Materials. *American Society for Metals International*, p. 30.

74. Montgomery, D. C. (1991). *Introduction to Statistical Quality Control* (2nd ed.). New York, NY, USA: John Wiley & Sons.

75. Unal, R., Dean, E. B. (1991). Taguchi Approach to Design Optimization for Quality and Cost: An Overview. *Conference of the International Society of Parametric Analysts*, (pp. 1-10). New Orleans.

76. Rao, R. S., et al. (2008). The Taguchi methodology as a statistical tool for biotechnological applications: A critical appraisal. *Biotechnology Journal, 3*(4), 510-23.

77. Jayaswal, B. K., Patton, P. C. (2007). *Design for Trustworthy Software: Tools, Techniques, and Methodology of Developing Robust Software.* Upper Saddle River, NJ, USA: Pearson Education, Inc.

78. *Oxford Dictionaries*. (n.d.). Retrieved March 23, 2014, from http://www.oxforddictionaries.com/us/definition/american_english/Latin-square?q=Latin+Square

79. Xu, J. (2006). *Dielectric Nanocomposites for High Performance Embedded Capacitors in Organic Printed Circuit Boards(Doctoral Dissertation).* Atlanta, Georgia, USA: Georgia Institute of Technology.

80. Lui, K., et al. (2012). Characterization ofBonding Between Poly(dimethylsiloxane) and Cyclic Olefin Copolymer using Corona Discharge Induced Grafting Polymerization. *Journal of Colloid and Interface Science*(365), 289-95.

81. Boyd, S., Kirkwood, J. (2011, March). *Quantitative analysis using ATR-FTIR Spectroscopy Application Note.* Retrieved March 5, 2012, from Agilent Technologies: http://www.agilent.com/chem

82. ASTM Standard D 1708-06a. (2006). *Standard Test Method for Tensile Properties of Plastics by Use of Microtensile Specimens*, 1-5.

83. Craig, R. R., Jr. (2000). *Mechanics of Materials* (2nd ed.). New York: John Wiley & Sons.

84. Walley, S.M., Field, J. E. (2005). Elastic Wave Propagation in Materials. *Encyclopedia of Materials: Science and Technology*, 1-7. Retrieved 12 12, 2012, from http://www.smf.phy.cam.ac.uk/Publications/Strength%20papers/607StrWalleyEncycMateronline.pdf

85. Mal, A.K. (n.d.). Elastodynamics Class Notes. *Mechanical and Aerospace Engineering Department MAE 257A, ESS M224A*. Los Angeles, CA, USA: University of California Los Angeles.

86. Kline, R. A. (1992). *Nondestructive Characterization of Composite Media.* London, England: CRC Press.

87. Wooh, S-C., Daniel, I. M. (1991). Mechanical characterization of a unidirectional composite by ultrasonic methods. *Journal of Acoustical Society of America, 90*(6), 3248-53.

88. Hsu, D. K., et al. (1992). Ultrasonic Determination of Anisotropic Elastic Constants and Flaw Sizes in Thick Composite Laminates. In K. M. Finlayson, K. R. Osborn, & W. Shalaby (Ed.), *6th Japan-U.S. Conference on Composite Materials* (pp. 666-69). Orlando: CRC Press.

89. Balasubramaniam K., Whitney, S. C. (1996). Ultrasonic through-transmission. *Independent Nondestructive Testing and Evaluation (NDT & E) International, 29*(4), 225-36.

90. Adamowski, J. C., et al. (2007). Ultrasonic through-transmission characterization of fiber reinforced composites using a large aperture receiver. *Proceedings of the International Congress on Ultrasonics*, (pp. 1-4). Vienna.

91. Mourik, N., et al. (1997). Ultrasonic Characterization of the Elastic Anisotropy in Aluminum-SiC and -Al2O3 Meta l Matrix Composites. (O. Thompson, & D. E. Chimenti, Eds.) *Review of Progress in Quantitative Nondestructive Evaluation, 16*, 1143-1150.

92. Parthasarathi S., et al. (1995). Ultrasonic characterization of elastic anisotropy in plasma-sprayed alumina coatings. *Journal of Thermal Spray Technology, 4*(4), 367-73.

93. Yeheskel, O. (2006). Quantitative NDE OF The Young's Modulus of FCC Porous Metals. *Proceedings of the 12th Asia-Pacific Conference on NDT*, (pp. 1-7). Auckland.

94. Rokhlin, S.I., Wang, L. (2002). Ultrasonic waves in layered anisotropic media: characterization of multidirectional composites. *International Journal of Solids and Structures*(39), 4133-49.

95. Mittal, R., et al. (2007). Mechanical Constants Characterization of Thin Layers by Low Frequency Ultrasonics. *Numerical and Computational Methods in Engineering (CMNE/CILAMCE) Conference Proceedings, Oporto, Portugal 2007*, (pp. 1-14). Oporto.

96. Solodov, I., et al. (2008). Ultrasonic Characterization of Elastic Anisotropy in Composites: Case Study of CFRP. *Materials Testing, 50*(10), 602-8.

97. Baid, H. K. (2012). *Detection of Damage in a Composite Structure Using Guided Waves (Doctoral dissertation) University of California Los Angeles, Los Angeles, CA.,*. Ann Arbor, MI: ProQuest LLC.

98. Agilent 16451B Dielectric Test Fixture Operation and Service Manual. (2000). Japan: Agilent Technologies.

99. Kuczek, T. (2005, February 10). Taguchi Analysis. *STAT 513/IE 530: Statistical Quality Control course manual*, 1-27. West Lafayette, Indiana, USA: Purdue University. Retrieved March 12, 2014, from http://www.stat.purdue.edu/~kuczek/stat513/taguchi.pdf

100. Ghosh, S., et al. (2012). Wear Behaviour of Al-SiCp Metal Matrix Composites and Optimization Using Taguchi Method and Grey Relational Analysis. *Journal of Minerals and Materials Characterization and Engineering*(11), 1085-94. Retrieved 12 20, 2012, from http://www.scirp.org/journal/PaperDownload.aspx?

101. Samandari, S. S., Khatibi, A. A. (2007). Evaluation of Elastic Modulus of Polymer Matrix Nanocomposites. *Polymer Composites*, 406-11.

102. Fu, S-Y., et al. (2008). Effects of particle size, particle/matrix interface adhesion and particle loading on mechanical properties of particulate-polymer composites. *Composites Part B: Engineering*, 933-61.

103. Clark, I. J., et al. (1999). Hydrothermal Synthesis and Characterization of BaTiO3 Fine Powders: Precursors, Polymorphism, and Properties. *Journal of Materials Chemistry*(9), 83-91.

104. Fu, S. Y., Lauke B. (1998). Characterization of tensile behaviour of hybrid short glass fibre calcite particle ABS composite. *Composite Part A*(29A), 575-83.

105. Radford, K. C. (1971). The mechanical properties of an epoxy resin with a second phase dispersion. *Journal of Materials Science*(6), 1286-91.

106. Zhu, Z. K., et al. (1999). Preparation and properties of organosoluble polyimide/silica hybrid materials by sol–gel process. *Journal of Applied Polymer Science*(73), 2977-84.

107. Wang M, et al., . (1998). Young's and shear moduli of ceramic particle filled polyethylene. *Journal of Materials Science: Materials in Medicine*(9), 621-4.

108. Smithers RAPRA. (n.d.). *Epoxy Resins*. Retrieved July 2, 2014, from http://info.smithersrapra.com/downloads/chapters/Thermoset%20Resins.pdf

109. Nakamura, Y., et al. (1999). Effects of particle shape, size and interfacial adhesion on the fracture strength of silica-filled epoxy resin. *Polymers & Polymer Composites*(7), 177-86.

110. Buggy, M., et al. (2005). Polymer–filler interactions in kaolin/nylon 6,6 composites containing a silane coupling agent. *Polymer–filler interactions in kaolin/nylon 6,6 composites containing a silane coupling agent*(36), 437-42.

111. Pukanszky, B,, Voros , G. (1993). Mechanism of interfacial interactions in particulate filled composites. *Composite Interfaces*(1), 411.

112. Reynaud, E., et al. (2001). Nanofillers in polymeric matrix: a study on silica reinforced PA6. *Polymer*(42), 8759-68.

113. Nakamura, Y., et al. (1992). Effects of particle size on mechanical and impact properties of epoxy resin filled with spherical silica. *Journal of Applied Polymer Science*(45), 1281-9.

114. Yoon, D-H., et al. (2003). Dielectric constant and mixing model of BaTiO3 composite thick films. *Materials Research Bulletin*(38), 765-72.

115. Simpkin, R. (2010). Derivation of Lichtenecker's Logarithmic Mixture Formula From Maxwell's Equations. *IEEE Transactions on Microwave Theory and Techniques, 58*(3), 545-50.

116. Barber, P., et al. (2009). Polymer Composite and Nanocomposite Dielectric Materials for Pulse Power Energy Storage. *Materials*(2), 1697-33.

117. Arit, G., et al. (1985). Dielectric properties of fine-grained barium titanate ceramics. *Journal of Applied Physics, 58*(4), 1619-25.